

Atomic level insight into irradiation effects in nuclear fuel materials

Présentée le 19 mars 2024

Faculté des sciences de base
Laboratoire de physique des réacteurs et de comportement des systèmes
Programme doctoral en science et génie des matériaux

pour l'obtention du grade de Docteur ès Sciences

par

Shaileyee BHATTACHARYA

Acceptée sur proposition du jury

Dr A. Hessler-Wyser, présidente du jury
Dr M. A. Pouchon, Dr G. Kuri, directeurs de thèse
Prof. C. Ekberg, rapporteur
Prof. S. Finkeldei, rapporteuse
Dr P. Sprung, rapporteur

If you want to shine like a sun,
first burn like a sun.
– A.P.J. Abdul Kalam

To my family . . .

Acknowledgements

Embarking on this Ph.D. journey has been a long, yet immensely gratifying journey. Without the support and contributions of several people, directly or indirectly involved, my dissertation would not have seen the light of day.

Foremost, my sincere gratitude to *Dr. Goutam Kuri*, my thesis supervisor, whose unwavering support over the last four years, both personally and professionally, have boosted my confidence and enhanced my skills. Thank you for the encouragement and guidance you provided throughout, especially during the challenging aspects of this project. Your tireless work ethics and commitment to perform any work to the best possible way has deeply influenced me.

I express my gratitude to *Dr. Manuel Pouchon*, the director of my thesis, for the many insightful conversations and scientific discussions that have significantly enriched my research work. Also, I am very inspired by his determination to commute to work daily by bike, regardless of the time or weather.

I extend my sincere appreciation to *Dr. Johannes Bertsch*, it has been a genuine privilege to work in the Nuclear Fuels group. Your leadership style and hardworking nature is an inspiration. Thank you for the motivation and the very insightful feedback you always provided.

A significant part of my Ph.D. thesis centered around the PSI HotLab, be it for sample preparation or the material characterization by different analytical techniques. This thesis would not have come to fruition without the support of the HotLab colleagues– *Matthias Martin, Röbi Zubler, Robin Grabherr, Roland Brütsch, Andrej Bullemer* and *Anders Jonas Wissting*. Thank you for the time that you have always found for me, and your patience in accommodating my (sometimes, very tight) work timelines.

Synchrotron light experiments is a pivotal part of my thesis. I owe the success of the PSI–SLS beam campaigns to the beamline scientists– *Dr. Camelia Borca* (PHOENIX beamline), *Dr. Thomas Huthwelker* (PHOENIX beamline), *Dr. Malgorzata Makowska* (microXAS beamline) and *Dr. Ana Diaz* (cSAXS beamline). Thank you for your exceptional help, collaboration, and for going above and beyond by working seamlessly, even outside of regular office hours.

My acknowledgements also go to *Dr. Elisabeth Müller* at the Electron Microscopy Facility (EMF) at PSI. Thank you for your guidance and support throughout, be it during the FIB-SEM training or TEM experiments.

My gratitude extends to the closest colleagues at PSI– *Liliana, Aaron, Francesco, Okan, Cloé* and *Jonny*, to name a few– for our many shared moments of laughter and fun and

hard work. Beyond being just work colleagues, you have become friends. I would also like to express thanks to the numerous other colleagues at PSI with whom I have had the privilege to interact during the last four years, both on a professional and personal level. I could not have asked for better colleagues!

Special acknowledgement is reserved for *swissnuclear*, for providing financial support to this project, as well as for the valuable feedback during the various update meetings. I extend my thanks to the Swiss nuclear powerplants– *Kernkraftwerk Gösgen* and *Kernkraftwerk Leibstadt* – for providing the fuel samples investigated in this thesis.

Finally, my deepest appreciation goes to my parents, and all of my family. I am who I am because of you! Thank you for always believing in me and for being my constant pillars of strength.

The collective support of everyone mentioned, and those inadvertently omitted, has been instrumental in the realization of this thesis. Thank you all!

– Shaileyee

Abstract

Microstructural evolution during in-pile irradiation, radiation damage effects and fission products behavior in UO_2 nuclear fuel are key issues in understanding and for the modeling of the performance as well as safety characteristics of nuclear fuels in the reactor. In general, the overall performance of standard UO_2 at high burnup is often limited by the physical phenomena of pellet-to-cladding mechanical interaction, gaseous swelling of a fuel pellet, and the release of stable fission gases. Therefore, alternative fuel materials with improved properties have been uncovered, such as chromia-doped UO_2 , capable to mitigate the above listed effects. This thesis work reports an experimental investigation on irradiation induced microstructure evolution in high burnup standard UO_2 and chromia-doped UO_2 spent fuels considering the role of dopant Cr and chemical effect of fission product elements, and a comparison of the results of doped fuel with those observed for the standard (undoped) UO_2 material. To clarify the prevailing microstructural aspects associated with the development of the so-called high burnup structure, additional experiments have been performed for an evaluation of atomic-scale uranium and plutonium environment in intermediated burnup UO_2 . In order to investigate the chemical state(s) of the dopant Cr in UO_2 crystals, micro-beam XANES experiments were conducted in fresh and irradiated doped fuels. Spent nuclear fuel is intensely radioactive and extremely difficult to investigate experimentally. Therefore, methods have been developed to prepare small sub-samples from targeted regions of the spent fuel pellets. Synchrotron based modern analytical techniques of scanning micro-beam X-ray fluorescence spectrometry, X-ray diffraction, and microprobe X-ray absorption spectroscopy have been used for structural analyses covering a wide range of local burnup from 50 to 100 MWd/kgU in the investigated materials. The obtained results are supplemented by electron probe micro analysis and transmission electron microscopy studies. The line profiles of characteristic X-ray diffraction peaks are analyzed in detail for a quantitative evaluation of UO_2 lattice parameter with fuel burnup, microscale spatial distribution of residual strain within irradiated UO_2 crystallites, and the remnant dislocation contents in spent fuels. The results provide a comprehensive and comparative overview of the irradiation induced microstructure evolution and structural changes in high burnup standard and doped UO_2 fuels. A detail analysis of the of extended-range X-ray absorption spectra of irradiated samples provide novel insights into the local atomic arrangement of uranium and plutonium ions including their oxidation state assignment, and furnish a clear atomic scale picture of the uranium dioxide crystal structure modifications resulting from irradiation effects. The obtained experimental results of this study on the chemical

and local structural specificity of uranium and plutonium in irradiated UO_2 matrix shall be useful for fuel modelling studies that could account for the UO_2 fuel lattice defects evolution as well as fission products and/or actinide products behavior under irradiation conditions.

Keywords

Uranium dioxide, chromia-doped fuel, spent nuclear fuel, burnup, electron probe microanalysis, scanning electron microscopy, transmission electron microscopy, synchrotron X-rays, X-ray diffraction, X-ray absorption spectroscopy, lattice parameter, fission product, lattice strain, dislocation density.

Zusammenfassung

Die mikrostrukturelle Entwicklung von UO_2 -Kernbrennstoff während der Bestrahlung im Reaktor, Strahlenschäden und das Verhalten der Spaltprodukte sind Schlüsselthemen für das Verständnis und die Modellierung der Leistungs- und Sicherheitseigenschaften von Kernbrennstoffen. Allgemein wird die Performance von Standard- UO_2 bei hohem Abbrand durch die Wechselwirkung zwischen Pellets und Hüllrohr, Brennstoffschwellen und Freisetzung von Spaltgas limitiert. Alternative Brennstoffe mit verbesserten Eigenschaften, wie z. B. mit Chrom dotiertes UO_2 , reduzieren die genannten Effekte. Die vorliegende Dissertation befasst sich mit experimentellen Untersuchungen der strahlungsinduzierten Mikrostrukturveränderungen in abgebrannten Standard- UO_2 - und mit Chromoxid-dotierten UO_2 -Brennstoffen mit hohem Abbrand, unter Berücksichtigung der Rolle der Dotierung mit Chrom und der chemischen Wirkung von Spaltprodukten. Die entsprechenden Resultate für dotierten Brennstoff werden denjenigen für undotierten Brennstoff, Standard- UO_2 gegenübergestellt. Um die vorliegenden Mikrostruktur mit der Hochabbrandstruktur zu vergleichen und auch deren Entstehung zu klären, wurden zusätzliche Experimente zur Einbettung von Uran und Plutonium auf atomarer Ebene in UO_2 mit mittlerem Abbrand durchgeführt. Um die chemische Bindung des Dotierungselements Chrom im UO_2 Kristall zu untersuchen, wurden Messungen zur Röntgenabsorption nahe an der Absorptionskante (XANES) an unbestrahltem und bestrahltem Brennstoff durchgeführt. Abgebrannter Kernbrennstoff ist stark radioaktiv und lässt sich experimentell nur schwer untersuchen. Daher wurden Methoden entwickelt, um kleine Teilproben aus bestimmten Bereichen der abgebrannten Brennstoffpellets zu präparieren. Zur Untersuchung der Proben wurden Synchrotron-Analysen nach neustem Stand der Technik genutzt, Röntgenfluoreszenzspektrometrie (XRF), Röntgenbeugung (XRD) und Röntgenabsorptionsspektroskopie (XAS), unter Nutzung eines mikrometer-feinen Strahls zur Abrasterung der Probe. Die Proben decken einen weiten Bereich verschiedener Abbrände ab, die lokal zwischen 50 und 100 MWd/kgU liegen. Die gewonnenen Resultate werden durch Elektronensonden-Mikroanalyse und Transmissionselektronenmikroskopie-Untersuchungen ergänzt. Die Profile charakteristischer Röntgenbeugungspeaks werden in Abhängigkeit vom Brennstoffabbrand im Detail analysiert zwecks Bestimmung des UO_2 -Gitterparameters, der mikroskopischen räumlichen Verteilung der eingebrachten Dehnung innerhalb bestrahlter UO_2 -Kristallite und der Versetzungsdichte. Die detaillierte Strukturanalyse erweiterter Röntgenabsorptionsspektren liefert Resultate zur lokalen Anordnung von Uran- und Plutonium-Ionen, einschließlich ihres Oxidationszustands, und liefert damit

ein Bild der resultierenden Kristallstrukturmodifikationen des Urandioxids auf atomarer Ebene. Die experimentellen Ergebnisse zur Spezifität und lokalen strukturellen Einbettung von Uran und Plutonium in der bestrahlten UO_2 -Matrix können für die Brennstoffmodellierung genutzt werden. Die Modellierung wiederum kann für die Erklärung der Entwicklung von Gitterdefekten im UO_2 -Brennstoff sowie das Verhalten von Spaltprodukten und/oder Aktiniden unter Bestrahlungsbedingungen herangezogen werden.

Stichwörter

Urandioxid, mit Chromoxid dotierter Brennstoff, abgebrannter Kernbrennstoff, Abbrand, Elektronensonden-Mikroanalyse, Rasterelektronenmikroskopie, Transmissionselektronenmikroskopie, Synchrotron-Röntgenstrahlung, Röntgenbeugung, Röntgenabsorptionsspektroskopie, Gitterparameter, Spaltprodukte, Gitterdehnung, Versetzungsdichte.

Résumé

L'évolution de la microstructure lors de l'irradiation dans un réacteur, les effets d'endommagement d'irradiation et le comportement des produits de fission dans le combustible nucléaire UO_2 sont des questions clés pour la compréhension et la modélisation de la performance ainsi que des caractéristiques de sûreté. En général, les performances de l' UO_2 standard à taux de combustion élevé sont souvent limitées par les phénomènes d'interaction pastille-gaine, le gonflement du combustible et le dégagement des gaz de fission. Par conséquent, des matériaux combustibles alternatifs aux propriétés améliorées ont été découverts, tels que l' UO_2 dopé au chrome, capable de résister aux effets énumérés ci-dessus. Ce travail de thèse rend compte d'une étude expérimentale sur l'évolution de la microstructure induite par l'irradiation dans des combustibles usés UO_2 standard à haut taux de combustion et dopé au chrome, en considérant le rôle du dopant Cr et l'effet chimique des éléments des produits de fission. Les résultats du combustible dopé sont comparés avec ceux du combustible standard UO_2 (non dopé). Pour clarifier les aspects microstructuraux associés au développement de la structure à haut taux de combustion, des expériences supplémentaires ont été réalisées pour une évaluation de l'environnement de l'uranium et du plutonium à l'échelle atomique dans un UO_2 à taux de combustion intermédiaire. Pour analyser l'état chimique de l'élément de dopage chrome dans le cristal d' UO_2 , des mesures d'absorption des rayons X près du seuil d'absorption (XANES) ont été faites, utilisant du combustible irradié et non-irradié. Le combustible nucléaire utilisé est extrêmement radioactif et difficile à étudier expérimentalement. Par conséquent, des méthodes ont été développées pour préparer de petits sous-échantillons provenant de régions ciblées des pastilles de combustible usé. Des techniques analytiques modernes basées sur le synchrotron, telles que la spectrométrie de fluorescence X à microfaisceau, la diffraction des rayons X et la spectroscopie d'absorption des rayons X, ont été utilisées pour sonder les échantillons couvrant une large gamme de taux de combustion local de 50 à 100 MWj/kgU dans les matériaux étudiés. Les résultats obtenus sont complétés par des études de microsonde électronique et de microscopie électronique en transmission. Les profils des pics caractéristiques de diffraction des rayons X sont analysés en détail en fonction du taux de combustion pour une évaluation quantitative du paramètre de maille d' UO_2 , de la distribution spatiale microscopique de la déformation résiduelle dans les cristallites d' UO_2 irradiés et du contenu des dislocations résiduelles dans les combustibles usés. Les résultats fournissent un aperçu complet et comparatif de l'évolution de la microstructure induite par l'irradiation et des changements structuraux dans les combustibles UO_2 dopés et à taux de combustion élevé. Une analyse détaillée

des spectres d'absorption des rayons X (EXAFS) d'échantillons irradiés fournit de nouvelles informations sur l'arrangement atomique local des ions uranium et plutonium, y compris leur état d'oxydation, et fournit une image claire à l'échelle atomique des modifications de la structure cristalline du dioxyde d'uranium qui résultent des effets de l'irradiation. Les résultats expérimentaux obtenus dans cette étude sur la spécificité chimique et structurale locale de l'uranium et du plutonium dans la matrice UO_2 irradiée seront utiles pour les études de modélisation du combustible qui pourraient rendre compte de l'évolution des défauts du réseau du combustible UO_2 ainsi que du comportement des produits de fission et/ou des produits actinides dans des conditions d'irradiation.

Mots clé

Dioxyde d'uranium, combustible dopé au chrome, taux de combustion, microsonde électronique, microscopie électronique à balayage, microscopie électronique en transmission, radiation synchrotron, diffraction des rayons X, spectroscopie d'absorption des rayons X, paramètre de maille, produits de fission, extension du réseau, densité de dislocations.

Contents

Acknowledgements	i
Abstract	iii
Zusammenfassung	v
Résumé	vii
List of abbreviations	xiii
List of samples investigated	xiv
List of figures	xv
List of tables	xix
Structure of the thesis	xxi
1 Introduction	1
1.1 General introduction on nuclear reactors and their fuel	1
1.2 Literature review	4
2 Materials and Methodology	9
2.1 Fuel materials used	9
2.2 Sample preparation methods	10
2.2.1 EPMA investigations	11
2.2.2 Replica print	11
2.2.3 FIB milling	12
2.3 Beamline setup and experimental conditions	13
2.3.1 microXAS (X05LA) station	14
2.3.2 PHOENIX (X07MA/B) station	16
2.4 Experimental data reduction	17
2.4.1 XRD data	17
2.4.2 XAS data	21
2.5 Theoretical approach to the experimental techniques	21
2.5.1 X-ray fluorescence (XRF)	21
2.5.2 X-ray diffraction (XRD)	23
2.5.3 X-ray absorption fine structure (XAFS)	25

3	Local Burnup Determination by ^{148}Nd Method	33
3.1	Burnup profile in the pellets	33
4	Lattice Parameter Evolution in UO_2	39
4.1	Micro-beam XRF and XRD analyses	39
4.2	Evaluation of UO_2 lattice parameter	41
4.3	Effect of dissolved fission products on UO_2 lattice	45
4.4	Summary	49
5	Residual Lattice Strain in UO_2	51
5.1	Scanning XRD data processing	51
5.2	Microscale lattice strain distribution	52
5.3	Summary	56
6	Dislocation Content in UO_2 Fuel	57
6.1	Quantification of dislocation density	58
6.1.1	Cahn-Nye formalism	58
6.1.2	GND density evolution with burnup	58
6.2	Summary	64
7	Chemical State of Dopant Cr in UO_2	65
7.1	Specimen preparation	65
7.2	EPMA studies	66
7.3	Synchrotron investigations	69
7.3.1	Micro-beam XRF analysis	69
7.3.2	Cr K-edge XANES	70
7.4	Summary	75
8	Chemical Speciation of U and Pu in Standard UO_2	77
8.1	Micro-beam XRF analysis	77
8.2	Micro-beam XAS investigations of spent fuel	78
8.2.1	Uranium speciation	78
8.2.2	Plutonium speciation	82
8.3	Summary	84
9	Analysis of Fission Gas using TEM	85
9.1	Distribution of fission gas bubbles	85
9.2	Lattice imaging and SAEDP analysis	91
9.3	Summary	92
10	Summary and Conclusions	95
10.1	Conclusions	96
10.2	Outlook	98

Appendix A	101
Bibliography	107
Curriculum vitae	123

List of abbreviations

BSE	Back-scattered electrons
BU	Burnup
BWR	Boiling water reactor
CCD	Charge coupled device
DF	Doped fuel
EDS	Energy dispersive spectrometer
EPMA	Electron probe micro analysis
EXAFS	Extended X-ray absorption fine structure
FIB	Focused ion beam
FIMA	Fission per initial metal atom
FP	Fission product
FT	Fourier transform
FWHM	Full width at half-maximum
GND	Geometrically necessary dislocation
HBS	High burnup structure
KKG	Kernkraftwerk Gösgen (Gösgen nuclear powerplant)
KKL	Kernkraftwerk Leibstadt (Leibstadt nuclear powerplant)
LWR	Light water reactor
PCI	Pellet cladding interaction
PIE	Post irradiation examination
PWR	Pressurized water reactor
RDF	Radial distribution function
SAEDP	Selected area electron diffraction pattern
SE	Secondary electrons
SEM	Scanning electron microscopy
SLS	Swiss Light Source
SPP	Secondary phase particle
SSD	Solid state detector
TEM	Transmission electron microscopy
WDS	Wavelength dispersive spectrometer
XAFS	X-ray absorption fine structure
XANES	X-ray absorption near edge structure
XAS	X-ray absorption spectroscopy
XRD	X-ray diffraction
XRF	X-ray fluorescence



List of samples investigated

FSF	Fresh Standard UO_2 Fuel
FDF	Fresh Doped UO_2 Fuel
BSF (-C/R)	Standard UO_2 Fuel irradiated at BWR (-Center/ Rim)
BDF (-C/R)	Doped UO_2 Fuel irradiated at BWR (-Center/ Rim)
PSF (-C/R)	Standard UO_2 Fuel irradiated at PWR (-Center/ Rim)

List of figures

1.1	Schematic diagram of PWR fuel rod assembly showing (a) the fuel pellet, and (b) the fuel rod.....	1
2.1	Sample preparation via replica method.....	11
2.2	Types of interactions of electron with matter.....	12
2.3	Sample preparation via FIB-SEM for synchrotron analyzes.....	13
2.4	The end-station of the microXAS (X05LA) beamline, used for the measurements of the radioactive fuel specimens.....	15
2.5	The end-station of the PHOENIX (X07MA/B) beamline.....	16
2.6	An example of a two-dimensional μ XRD pattern acquired from corundum α - Al_2O_3 powder sample measured at 17.2 keV energy.....	17
2.7	Example of 1D diffraction spectrum of reference Al_2O_3 powder sample.....	18
2.8	Plot of standard deviation on d -spacing versus d -spacing, obtained by analyzing the XRD data of reference Al_2O_3 sample.....	19
2.9	The cubic fluorite unit cell of uranium dioxide.....	19
2.10	Types of interactions of X-rays (photons) with matter.....	22
2.11	Schematic representation of K and L series electronic transition.....	23
2.12	Laue photographs of zinc blende (presented by Laue, Friedrich and Knipping on June 8, 1912, at Königlich Bayerische Akademie der Wissenschaften)	24
2.13	Schematic representation of the Bragg diffraction. X-ray with wavelength λ is incident on a crystal of symmetrical arrangement of atoms having interplanar spacing as d at an angle θ . The optical path difference travelled by the two waves is equal to $2d\sin\theta$	25
2.14	Typical $\text{L}_{3\text{-edge}}$ XAFS spectrum of uranium.....	27
2.15	(a) Graphical representation of X-ray absorption by an isolated atom. (b) Graphical representation of X-ray absorption in a multi-atom system, wherein the outgoing photoelectron wave experience interference (both constructive and destructive) effect with itself due to the presence of backscattering atoms.....	29

3.1	Radial distribution of the normalized U, Pu and O content in the spent fuel pellet PSF measured by EPMA.....	34
3.2	Radial distribution of the normalized U, Pu and O content in the spent fuel pellet BSF measured by EPMA.....	34
3.3	EPMA intensity maps of neodymium signal collected from the outer edge region of the (a) BSF and (b) BDF pellets.....	35
3.4	Quantitative EPMA of Nd and burnup distribution profile of PSF, measured (with 20 keV, 320 nA and ~300 nm electron beam spot size) along the diameter of the spent fuel pellet.....	36
3.5	Quantitative EPMA of Nd and burnup distribution profile of BSF, measured (with 20 keV, 320 nA and ~300 nm electron beam spot size) along the diameter of the spent fuel pellet.....	37
3.6	Quantitative EPMA of Nd and burnup distribution profile of BDF, measured (with 20 keV, 320 nA and ~300 nm electron beam spot size) along the diameter of the spent fuel pellet.....	38
4.1	Elemental uranium distribution recorded by μ XRF mapping from the BDF-R specimen.....	40
4.2	Comparison of the experimental XRD patterns for fresh and irradiated chromia-doped UO_2 fuels. The irradiated fuel has a local burnup of about 70 MWd/kgU.....	42
4.3	XRD reflections (331) of unirradiated and irradiated DF specimens having burnup in the range of 64 to 90 MWd/kgU.....	43
4.4	UO_2 lattice parameter evolution as a function of fuel burnup for standard UO_2 and chromia-doped UO_2 spent fuels. The data are shown by symbols and the long-dashed lines are drawn to guide the eye. The arrows indicate the lattice parameters for unirradiated standard and doped fuel, respectively.....	44
4.5	Changes in UO_2 unit cell lattice parameter due to various soluble additives with various valences analyzed for chromia-doped UO_2 spent fuel.....	48
5.1	(a) The μ XRF element mapping (2 μm step size, 2 s exposure) with the U La fluorescent line of the area under investigation for identifying spent fuel UO_2 particles (local burnup ~68 MWd/kgU) on the Kapton tape, shown for BSF-C sample. (b) The corresponding lattice strain distribution map of irradiated UO_2 crystallites for the entire mapped area, obtained by analyzing the scanning μ XRD data set in a batch-wise processing mode.....	54
5.2	(a) The μ XRF element mapping (2 μm step size, 2 s exposure) with the U La fluorescent line of the area under investigation for identifying spent fuel UO_2 particles (local burnup ~68 MWd/kgU) on the Kapton tape, shown for BDF-C sample. (b) The corresponding lattice strain distribution map of irradiated UO_2 crystallites for the entire mapped area, obtained by analyzing the scanning μ XRD data set in a batch-wise processing mode.....	55

6.1	(a) Singular circular Laue spot observed in fresh non-irradiated fuels. In irradiated fuels, modifications are observed in the Laue spot in the form of (b) uniform streaking, (c) non-uniform streaking, and (d) splitting. The peak heights correspond with the intensity.....	59
6.2	Two-dimensional Laue images showing the typical shapes of the (220) Laue diffraction spots observed from chromia-doped fresh fuel and irradiated specimens at various burnups.....	61
6.3	GND density versus burnup for standard UO ₂ and chromia-doped UO ₂ nuclear fuels.....	62
7.1	(a) Photographic image of the FDF specimen. (b)–(f) Set of selected SEM images collected during FIB-based lamella preparation. (f) The magnified view of the sample BDF-C. The specimens shown in (a) and (e) have been analyzed by XRF and Cr K-edge XANES.....	66
7.2	EPMA maps showing distributions of (a) chromium and (b) oxygen in the FDF specimen. EPMA line scan analyses of Cr and O across a selected Cr ₂ O ₃ precipitate are shown. Analyses were made under measurement conditions of 10 keV and 90 nA with an electron beam spot size ~0.1 μm.....	67
7.3	(a) An EPMA image of the dopant Cr collected from the center region of the BDF pellet. In (b)–(d) , distribution maps of EPMA results for Cr, Mo, and Ru, obtained from the same sample area of the fuel and collected simultaneously, are shown.....	68
7.4	Synchrotron radiation induced XRF spectrum measured from the FDF specimen. The element Cr was detected in all regions of the specimen. The XRF peak of Cr is marked in the spectrum. The spectrum is measured with 6200 eV incident photons and collected for 15 s from a single spot location of the specimen.....	69
7.5	Normalized and background removed Cr K-edge XANES spectrum of (a) Cr metallic foil, (b) Cr ₂ O ₃ powder, and (c) CrO ₃ powder. In the insets, the first derivatives of the XANES data are shown which reveal the absorption edge energies.....	71
7.6	(a) Micro-beam XRF elemental chromium map obtained from the FDF specimen. (b) Micro-beam Cr K-edge XANES spectrum recorded from a precipitate-free area of the specimen marked by a circle in (a). The inset shows the first derivative of the XANES curve.....	72
7.7	(a) Micro-beam XRF elemental chromium map obtained from the BDF-C specimen having a local burnup of about 68 MWd/kgU. (b) Micro-beam Cr K-edge XANES spectrum recorded from the Cr-rich hotspot area of the specimen marked by an arrow in (a). The inset shows the first derivative of the XANES curve.....	73

8.1	Micro-beam XRF spectrum of PSF-R specimen measured using synchrotron light.....	78
8.2	Comparison of the U L ₃ -edge XAS spectra measured from the FSF and PSF-R samples analyzed. The inset shows the first derivative of the XANES spectra, used to characterize the oxidation state of uranium in the fuels.....	79
8.3	k^3 -weighted FT-EXAFS data shown in the overlap mode for fresh and irradiated UO ₂ samples.....	79
8.4	First shell (U–O) Fourier-filtered experimental (dotted symbol) and best-fitted (solid curve) spectra of (a) pristine UO ₂ , and (b) irradiated UO ₂	81
8.5	Pu L ₃ -edge XAS spectrum measured from the spent fuel UO ₂ (PSF-R) specimen. In the inset, the first derivative of the XANES data is presented.....	83
8.6	Radial distribution function (k^l -weighted) of the Pu L ₃ -edge EXAFS data shown in Fig. 8.5.....	83
9.1	Broad view of the PSF-C specimen investigated by TEM.....	86
9.2	TEM images showing the distribution of gas bubbles decorating the grain boundaries of nano-sized UO ₂ grains observed for the PSF-R specimen. The images are taken in (a) over-focus mode, and (b) under-focus mode.....	87
9.3	Bright-field electron micrograph image showing gas bubbles distribution in the PSF-R specimen.....	87
9.4	(a) TEM image of a gas bubble (size ~85 nm) containing a metallic fission products precipitate (size ~50 nm). (b) An EDX spectrum recorded from the metallic precipitate. The characteristic Mo peak can be observed in the spectrum.....	89
9.5	(a) TEM image of a large fission gas bubble (~45 nm) touching a precipitate, which consists of metallic fission products. (b) An EDX spectrum recorded from the precipitate region. The characteristic Mo peak can be observed in the spectrum.....	90
9.6	(a) Bright-field TEM image of a selected area of the PSF-R specimen showing UO ₂ sub-grains that originate from polygonization of the original ‘mother’ grains. The image was taken from the [011] crystal orientation. Inset: Fast Fourier transform of lattice image from the area outlined by a yellow dotted box. (b) High-resolution TEM lattice fringe image of the region highlighted by the yellow square in (a). (c) Quantitative analysis of inter-planar lattice spacing. Profile in a rectangular frame showing eleven successive lattice strips along the {111} planes.....	91

List of tables

2.1	Details of the BWR fuel samples investigated.....	9
2.2	Details of the PWR fuel samples investigated.....	10
2.3	Excitation energies (in keV) and fluorescent energies (in keV) of the elements of interest analyzed.....	14
4.1	Quantitative EPMA results of element concentrations obtained from the BDF pellet.....	47
6.1	Measured GND densities of standard and chromia-doped UO_2 fuels as a function of burnup.....	63
7.1	Measured edge energy and oxidation state assignment of Cr in various specimens.....	70
8.1	Structural parameters (R , N , σ and E_0) of fresh and irradiated standard UO_2 fuel.....	82

Structure of the thesis

This thesis includes both unpublished results and published studies of the author.

Chapter 1 gives a brief overview of the principal research aspects presented in this thesis, along with a literature survey of fuel behavior under irradiation.

Chapter 2 contains information about the materials investigated, the experimental techniques used for sample preparation and analysis, and the theoretical approach used for the applied analytical techniques.

Chapter 3 details the method used for local burnup determination of the spent fuel pellets. The burnup profile is calculated from the local concentration value of fission product Nd, along with the axial gamma scanning data of ^{137}Cs isotope collected from PIE results of the full-length mother fuel rod.

Chapter 4 provides micro-beam X-ray diffraction results of irradiated standard and doped UO_2 fuels. The study includes an evaluation of the lattice parameter changes brought by irradiation in UO_2 crystals for different burnup levels of the fuel material. Primarily, the effects most likely to influence the lattice dimension are accumulated fission products in soluble phases and the presence of irradiation-induced defects. The anticipated change of UO_2 lattice spacing due to only successive doping with soluble fission products furnish a very small value as opposed to the experimentally measured enlargement of the lattice constant.

Chapter 5 highlights the microscale spatial distribution of in-plane residual strain within irradiated UO_2 crystallites, brought about by the FPs incorporation and neutron irradiation-induced defects.

Chapter 6 concerns the quantitative trend of remnant dislocation contents in spent UO_2 fuels of different burnups. The dislocation density has been determined by using the Cahn-Nye analysis and a measured Laue spot streak length. The obtained experimental results are comparable with both theoretical simulations and limited experimental observations reported in the literature.

Chapter 7 focusses on chemical state and distribution of dopant Cr in irradiated doped fuels. EPMA measurements have shown a homogeneous distribution of Cr within the grains, along with some micron-sized Cr_2O_3 precipitates. For the irradiated fuel,

however, most of the Cr has been found to be expelled from the matrix and migrated towards the grain boundary. Another observation is that the available Cr, being a metallic element, is captured by the other metallic fission products forming intermetallic compounds in the irradiated fuel matrix. In this regard, Cr K-edge XANES data have been measured from fresh and irradiated doped fuels, and the dopant state has been calculated.

Chapter 8 comprises the results from synchrotron based micro-beam XAS study to examine the local atomic scale structure around uranium atoms in the as-fabricated standard UO_2 pellet, and the next neighbor atomic environment of uranium in the irradiated UO_2 spent fuel material having a local burnup of about 50 MWd/kgU in the sample. The measured XAS spectra at the U L_3 -edge are quantitatively analyzed in combination with the least-squares fitting procedure that uses ab-initio FEFF simulations. The atomic scale structural parameters for U–O atom pair in the first coordination oxygen shell around uranium are determined. XAS has also been applied to probe the local structural environment of the actinide plutonium produced in the spent fuel.

Chapter 9 reports preliminary TEM results on reactor-exposed standard UO_2 fuel material. The physical state of intergranular rare gas bubbles, population of bubbles at the grain boundaries and the characteristics of the bubble-size distribution have been studied. Additional results presented are the crystallographic lattice constant data of irradiated UO_2 , measured from experimental TEM images.

Chapter 10 presents the conclusions of the thesis work, and an outlook with recommendations for future work avenues.

1 Introduction

In the year 2022, nuclear power contributed a substantial 2486.83 TWh to global electricity production, accounting for nearly 10% of the total worldwide electricity output [1]. In Switzerland, nuclear energy covers about one-third of the country's total net electricity production [2]. Currently, in Switzerland, there are three nuclear power plants comprising four operational reactors, all of which are light water reactors (LWRs). As the demand for electricity is on an ever-increasing trend globally, the need for nuclear energy (and other clean low-carbon energy sources) are at an all-time high.

1.1 General introduction on nuclear reactors and their fuel

The LWR is a type of thermal-neutron reactor that uses normal water at very high pressure in a primary circuit, wherein the water has dual functions – acting both as coolant as well as neutron moderator. The basic working principle of such a reactor is the fission of enriched uranium fuel, resulting in the generation of heat which converts the water to steam, that in turn, drives the steam turbine followed by conversion to electrical energy. Broadly, there are two major types of LWRs, namely boiling water reactors (BWRs) and pressurized water reactors (PWRs).

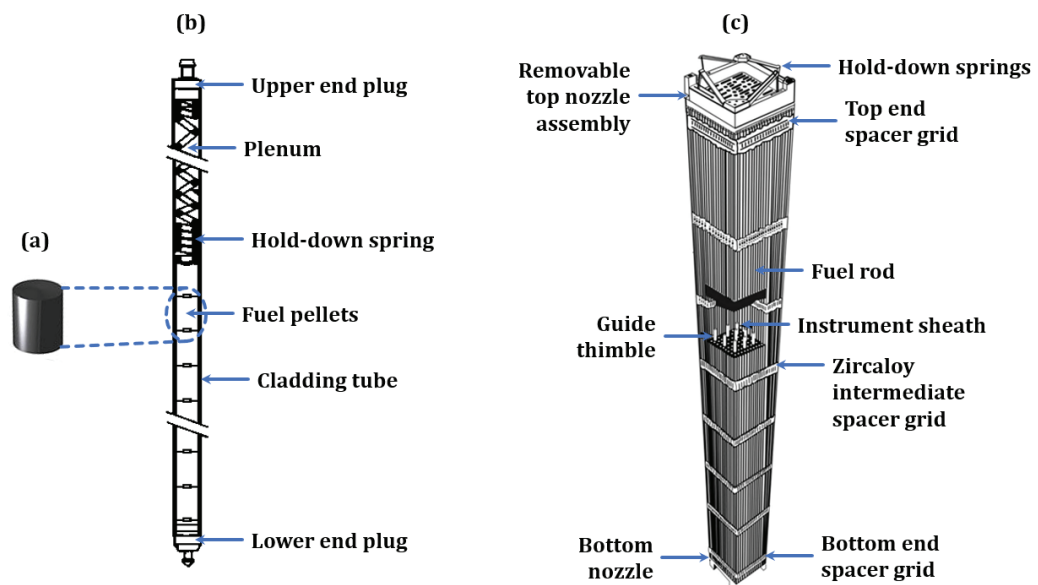


Figure 1.1: Schematic diagram of PWR fuel rod assembly showing (a) the fuel pellet, and (b) the fuel rod. Adapted from [3].

Uranium dioxide (UO_2) is the nuclear fuel material used in Switzerland, and in most LWRs worldwide. Natural uranium is composed of about 99.3% of the non-fissile ^{238}U isotope, 0.7% of the fissile ^{235}U isotope, and traces of non-fissile ^{234}U atoms [4]. Depending on the reactor type, during fuel fabrication, a process called *enrichment* is performed which increases the concentration of the fissile material (*i.e.*, ^{235}U atoms) from 0.7% to 3-5%. Typically, enriched uranium dioxide fuel is in the form of cylindrical ceramic pellets of dimensions roughly 10-18 mm in diameter and 5-10 mm in height (Fig. 1.1(a)). Hundreds of such pellets are stacked end-to-end in a long and thin cladding tube made of zirconium alloy, which constitute a fuel rod. Each fuel rod is sealed at both ends via welded end-plugs under the pressure of inert helium gas. An empty space, referred to as the plenum, exists between the top of the pellet stack and the upper end-plug, which facilitates for the thermal expansion of the pellets and inclusion of fission product gases. Typically, a spring is introduced into the plenum to exert a compressive force on the pellet stack, thereby inhibiting its motion (Fig. 1.1(b)). A bundle of several fuel rods arranged in a grid-like manner form the fuel assembly (Fig. 1.1(c)). Furthermore, each reactor core has some hundreds of such fuel assemblies.

In commercial UO_2 fuel, the neutron fission of heavy metal ^{235}U produces moving fragments of light and heavy elements, which eventually leads to the disruption of the cation-anion pairs of the host UO_2 lattice. During irradiation, the matrix element ^{238}U also absorbs epithermal neutrons thereby producing ^{239}U radionuclide, which successively decays by β -emissions to thermally fissile ^{239}Pu isotope and can undergo subsequent fissioning. The generated fission products (FPs) have different physical and chemical interactions with the irradiated fuel matrix. The solid FPs are either present as soluble oxides or insoluble precipitates in the UO_2 matrix. Gaseous FPs, such as Xe and Kr, however, have a strong tendency to aggregate into bubbles at the regions of radiation defects and grain boundaries owing to their very low solubilities in the matrix. The concentration of the FPs is not uniform throughout the pellet diameter. This is due to the fact that neutron absorption is maximum at the peripheral regions of the pellet as compared to pellet center, and hence, maximum fission activities occur at the periphery, thereby resulting in a higher concentration of FPs. The behavior, concentration and characteristics of the relevant fission products are important for the fuel rod performance, both, during normal operation and transients, *e.g.*, for the thermal conductivity and mechanical properties of the fuel pellet, development of the non-stoichiometric oxygen concentration or impact of corrosive fission products onto the fuel cladding.

After neutron irradiation of UO_2 in the reactor, the fuel microstructure is altered due to the accumulation of the FPs and the pile-up of radiation damage. These factors, in turn, result in the formation of the high burnup structure (HBS) [5-7]. The HBS is characterized by increased porosity due to high number density of fission gas bubbles, accumulation of crystallographic defects, and subdivision and polygonization of the original fuel grains [8,9]. However, the formation of the HBS is not observed in a uniform

manner throughout the pellet, with the effect being more pronounced in the peripheral regions of the pellet. The genesis of HBS occurs along the outermost region of the pellet, a few micrometers thick, and gradually proceeds towards the center [10]. Also, the low thermal conductivity of UO_2 [11] results in a temperature gradient along the pellet diameter, which increases the central pellet temperature and causes different rates of diffusion of the fission gases and thermal expansion of the irradiated matrix. A combination of these factors initiates fuel restructuring, plastic deformation, and cracking. The thermal conductivity of UO_2 is further reduced in the irradiated state. The exact mechanism of formation and propagation of HBS is not yet fully known, though a lot of research is available in the literature [12-18].

A relatively recent addition to the fleet of nuclear fuels used in LWRs is the chromia-doped UO_2 fuels [19]. The prime incentive for fuel doping with additives is to facilitate grain growth and pellet densification. Moreover, chromia-doping has also been found to mitigate the detrimental effects of pellet-cladding interaction by means of reduced fuel swelling, and to lower fission gas release by means of increased diffusion path length for the escape of the gases. The benefit of using doped fuels over conventional standard UO_2 fuels is the possibility of going to higher burnups, and hence, higher power output. The effects of doping conventional UO_2 fuels is also well studied [20-26].

Experimental characterization of UO_2 microstructure in irradiated fuels is necessary to gain insight into the irradiation effects from obtained data set, and modeling predictions of in-pile fuel performance as well as safe operation of the reactor. Besides experimental work to identify operational safety boundaries, theory-based fuel performance codes have been developed and being updated periodically in analyzing the behavior of nuclear fuels that can provide atomic level insights into experimental results. The names of the existing codes for light water reactor fuel performance calculations can be found in Ref. [27]. These codes consist of models containing correlations and algorithms to predict the fuel behavior in-pile. In a recent publication [28], advanced atomic scale simulation methods have been described that are required to model phenomena and to understand the underlying mechanisms responsible for the processes as well as development of mechanistic fuel performance codes. The discrete modelling approaches [28-30] that describe atomic-level processes in oxide nuclear fuels are mostly based on electronic structure calculations employing the density functional theory, classical molecular dynamics simulations using empirical interatomic potentials, the kinetic Monte Carlo and phase field methods, *etc.* To predict the in-pile fuel behaviors on a macroscopic scale, an atomic-level understanding of the fuel structure evolution and fission products behavior is of importance, defining the thermal, chemical, physical and mechanical behavior of the nuclear fuel during operation.

The objective of this thesis was to investigate the unexplored role of dopant Cr (in doped fuels), atomic scale structural changes in the UO_2 lattice of standard and Cr_2O_3 -doped UO_2 in the irradiated state, and the impact of fission products on the atomic

environment of UO_2 lattice. The samples analyzed are a selected group of standard and doped UO_2 fuels. The aim was to gain an in-depth understanding of the irradiation induced structural development (from atomistic to electronic structure) in the fuels and the relative performance of doped and standard UO_2 at a given burnup and under identical irradiation conditions. Since the dopant Cr ions in UO_2 can be oxidized to the toxic hexavalent Cr(VI) form [31] under various conditions, a study was also undertaken to examine the Cr oxidation state(s) and toxicity in fresh and irradiated Cr-doped fuels. The new results shall contribute to the understanding of the chemical behavior and release of fission products in transient conditions and/or in the course of a nuclear reactor accident scenario.

In previous studies and routine post irradiation examination (PIE) work performed on spent fuel pellets, microstructural changes of uranium dioxide materials have been investigated using electron-probe measurements (*e.g.*, SEM, EPMA, TEM, *etc.*). However, the applications of synchrotron-based microprobe X-ray techniques (*e.g.*, XRF, XRD, XAS, *etc.*) for microstructural investigations of irradiated nuclear fuels have been very limited, mostly due to limitations in handling radioactive samples at the corresponding facilities. In addition, the material properties of the restructured UO_2 lattice are not known, and the parameters responsible for initiation and development of new structures are not well-defined in the models. The synchrotron radiation based novel techniques have the ability to probe local atomic scale properties of any crystalline or amorphous objects, and the environment of specific atoms providing speciation and electronic structure. Some basic characteristics which can be observed, for instance in XAS, include atomic geometry, covalence and oxidation state of the probed atom. This allows more advanced conclusions about the analyzed atoms including coordination sphere characteristics or attached functional groups. Since characterization of high burnup spent fuels at the synchrotron radiation laboratory is very difficult due to radiation protection challenges at the beamlines, methods have been developed at PSI-HotLab for sample preparation and synchrotron-based measurements at the Swiss Light Source at PSI (PSI-SLS) overcoming those problems, especially for irradiated UO_2 spent fuels. In order to interpret XAS and XRD results, complementary experimental results of EPMA and SEM investigations on similar UO_2 materials have been used. TEM studies on reactor-exposed UO_2 material have also been undertaken within this project.

1.2 Literature review

The standard nuclear fuel material is uranium dioxide with an average grain size of about 10 μm . Large grain UO_2 with an average grain size of about 50 μm and doped with additives such as chromia, has been developed to potentially provide enhanced performance compared to un-doped UO_2 due to softening and better fission gas retention. Both standard fuel and chromia-doped fuel are currently being used in LWRs worldwide. Many important aspects of the fuel microstructure and behavior of standard

UO₂ material under in-pile conditions have been reported in the open literature [12,32-34]. Additionally, a large dataset of experimental results has been collected including instrumented irradiations in test reactors and irradiations in commercial power plants with subsequent PIE [35-37]. This database with available literature on fuel properties is currently used to review and/or upgrade existing computer codes for nuclear fuel performance calculations to obtain material properties needed for fuel modeling. Necessary to mention is that due to the proprietary nature of the fuel vendors' and power plants' R&D work, only limited information from the studies of operation induced changes in UO₂ based fuel matrix, employing various experimental methods such as EPMA, SEM, TEM, *etc.*, is available in the open literature.

During the burning of UO₂ fuel in operating nuclear reactors, fissile uranium atoms split into lighter atoms as a result of the fission reaction and produce isotopes of lighter elements. Heavy radioactive elements, such as plutonium as well as minor actinides, are also formed from neutron capture reactions with uranium. The fission product behavior and their interactions with the fuel are of outmost importance. In the literature, several publications have emerged concerning UO₂ fuels behavior at rod burnups up to 105 MWd/kgU. For instance, a review of 10 years of high burnup examinations by AREVA (today Framatome) is reported in [38]. The paper describes the European perspective on the occurrence of the high burnup structure (HBS) and the concomitant fission gas release, which increases with burnup and rod power. Many articles on the thermo-physical properties of LWR fuels [39,40], behavior of FPs [41,42] and re-resolution of fission gas atoms in irradiated UO₂ [43] have also been published in the open literature. Based on these results, some statements, not to be discussed here in detail, can be made as follows:

- The chemical reactivity and transport behavior of fission products during irradiation (to form binary fission product oxides, complex oxide fission product phases, fuel-fission product mixtures, intermetallic compound, *etc.*) influence the oxygen content inside a fuel rod, which in turn controls the oxygen potential of UO₂ fuels, being important for the interaction of the fuel pellet with the cladding inner surface.
- The volume fraction occupied by the fission products is determined by their physical state and chemical characteristics. When the volume fraction of the fuel constituent is increased, the resulting swelling can cause the fuel to exert pressure to the cladding inner wall.
- A portion of the gaseous fission products (*e.g.*, Kr, Xe) is not retained in the fuel but escapes to the plenum region of the fuel rod. The pressure of the released fission gas contributes to the internal stresses on the cladding.
- Fission products affect fuel properties, such as its thermal conductivity and melting point, thereby influencing the thermal performance of a fuel rod.

In addition, there exists a vast amount of literature about the fission products, both solid and gaseous ones, and selected references are [44-49]. The complex distribution of FP components (compounds, aggregations, *etc.*) within the fuel pellet depends on the reactor operation (power history) and the resulting boundary conditions. The principal properties of the FPs and minor actinides can be summarized as follows:

- Noble fission gases, (*e.g.*, Xe and Kr) precipitate to form bubbles within fuel grains and at grain boundaries, and these gas bubbles can have different number density and size distributions depending on the fuel burnup and power history.
- Noble metal fission products (*e.g.*, Mo, Pd, Rh, Ru, Tc) are distributed throughout the fuel matrix as insoluble intermetallic particles in sizes ranging from the nanometer scale to the micrometer scale.
- Other fission products (*e.g.*, Rb, Cs, Ba, Zr) may occur as oxide precipitates or in solid solution (*e.g.*, Sr, Zr, Nb, and lanthanides) within the UO₂ fuel matrix.
- The trans-uranium elements (*e.g.*, Np and Am) are mostly in solid solution within the UO₂ matrix, whereas Pu can form small islands.
- Volatile fission products (*e.g.*, Cs, I) often migrate from their initial region to the grain boundaries and pellet cracks within the fuel matrix, as well as to the fuel-cladding gap region.

Phenomena such as fission product diffusion, accumulation and release, have a strong impact on fuel properties and influence the heat transport. For gaining a deeper insight into structural changes, ion implantation technique of UO₂ with energetic ion beams have been frequently used [50-53]. A very large database on ion implantation induced damage formation and recovery for UO₂ and on fission product behavior has been published earlier by Matzke and Turos [54]. The self-radiation damage by α -decay in fresh (U,Pu)O₂ fuel has been studied [55]. The lattice parameter change and its thermal recovery were reported. The ultimate aim of these experiments has been to gain information on the overall damage buildup in UO₂ due to ion implantation, the nature and amount of the irradiation defects produced, the mechanisms involved in the observed structural transformations, and the parameters that trigger the structural changes. Results of these studies illustrate the evolution of implantation-induced defects, structural disorder and the damage properties of UO₂. Concurrently, computational modeling work at the atomic scale has been taken up to gain insights into the nature and the behavior of defects generated during irradiation. Previous molecular dynamics simulations [56] of primary damage produced by cascade overlaps in UO₂ have shown no amorphization of the UO₂ fluorite matrix. It is revealed that at the end of cascades, the residual damage state consisted mainly of vacancies located in the cascade's core and interstitials distributed at the periphery of the sub-cascade branches. Although the simulation carried out highlights the fact that fast Frenkel pair re-combinations play a key role in the resistance to amorphization [56], however, the

basic mechanisms for strong radiation tolerance of UO_2 matrix is not yet clarified. In addition, the material properties of the restructured UO_2 lattice occurring over a distance of inter-atomic spacing in the fuel matrix are not known, and the parameters responsible for micro-damage initiation and development of the macroscopic structure or the physical form in spent fuels are not certainly known.

On the fuel modeling side, theories, model-based evaluations and fuel performance analyses have been carried out by different researchers, and the study results have been published in the open literature, such as Refs. [57,58]. Different methodologies have been employed, which include atomistic molecular dynamics or Monte Carlo simulations, phase field approach (for simulation of microstructures and dislocation dynamics), and continuum-based finite element methods. Stan [59] has presented a model of oxygen diffusivity in UO_{2+x} , which can be used to predict point defect concentrations, oxygen diffusivity, and fuel stoichiometry for different temperature ranges and oxygen partial pressures. It is a consensus, however, that in spite of the availability of advanced fuel performance codes [60-63] as modelling tools, the simulated results are not always very conclusive and sufficiently accurate. This is mainly because many nuclear fuel codes are dedicated to study irradiation effects for specific applications, and use specific empirical correlations to evaluate these material properties [59]. In this regard, one of the important concerns is that the accommodation of FP ions and/or neutral atoms in UO_2 under irradiation conditions is less understood because of constraints on methods for in situ analysis and insufficient characterization possibilities. Also, mechanisms of diffusion as well as bonding of mobile FPs with Urania lattice and FPs migration at and close to grain boundaries are still unclear. All these phenomena are very much related to microstructural changes in UO_2 fuel under irradiation, and should be further investigated with the use of modern experimental methods, such as the desired synchrotron based XRD and XAS experiments, as done in this thesis work.

At present, there are certain limiting factors affecting the performance of standard UO_2 in the fuel rods, such as pellet-cladding interaction (PCI), the swelling of the fuel pellets, and fission gas release. These phenomena can cause or lead to fuel rod failure, which become significant in high burnup fuel. Therefore, in order to improve the operational performance and increase the safety margin of UO_2 -based fuels during normal LWR operating conditions as well as incidental or accidental events in the reactor core, the development of advanced nuclear fuel, such as chromia (Cr_2O_3)-doped UO_2 [64], gained importance in the nuclear industry during the last two decades. In Cr-doped fuel, the average grain size in the as-fabricated UO_2 pellet is about five times larger than the grains in a standard UO_2 fuel pellet. The larger grains microstructures promote reduced fuel swelling during irradiation and facilitate the retention of fission gases within the irradiated fuel pellet due to the longer diffusion path length for the gas atoms to escape via grain boundary diffusion followed by gas release to the fuel rod plenum. Previous studies found a decrease in the fission gas release rate by diffusion for the large grain-

size doped UO_2 , such as Ref. [65]. Investigations of an optimal synthesis and fabrication route for commercial nuclear fuel have revealed that one of the feasible ways to produce large grains, without altering the sintering times and/or changing temperatures, is the doping of UO_2 with certain metal oxide additives in small quantities [66,67]. In particular, chromium oxide (Cr_2O_3) is currently the most widely used additive to form large grain sized UO_2 pellet on sintering [19,20,68]. Experimental irradiation test results of Cr-doped fuel have also shown a better fuel-cladding compatibility (*i.e.*, PCI margins) and improved fission gas retention capability relative to standard UO_2 fuel [68,69].

A previous study on Cr-doped UO_2 preparation was focused on the grain growth behavior and microstructural evolution during all stages of sintering [70]. The added Cr_2O_3 is known to have a limited solubility in the UO_2 , and the excess of insoluble Cr_2O_3 always forms (sub)micrometer-sized precipitates. These precipitates remain as secondary phase particles (SPPs) in the UO_2 matrix. In recent years, different researchers have published many articles on the synthesis as well as characterization of model Cr-doped fuel materials [71-77]. Several mechanisms have been suggested to date to explain the role of Cr in promoting grain growth of UO_2 , such as incorporation of Cr^{3+} [74,76] or Cr^{2+} [71,75] into the UO_2 lattice through substitution of host uranium ions. It is noteworthy to mention that UO_2 grain growth process during sintering, distribution of Cr in the UO_2 matrix as well as the underlying incorporation mechanisms of Cr into the UO_2 lattice are complex, and still a controversial research subject that warrants future investigations.

In the case of irradiated nuclear fuels, identification and analysis of fission products as well as microstructural examination of the UO_2 pellets are of main importance in post irradiation examination (PIE) of used fuel pins. PIE results are useful to guide the course of the subsequent irradiations, serve as feedback for the quality of the fuel, assist in the evaluation of burnup limits, and there are PIE reports [19,78,79] on the in-reactor performance of doped UO_2 fuel rods. However, available PIE data obtained from chromia-doped fuels is not adequate to determine physical, chemical and structural properties of irradiated doped fuels, and to gain atomic-level insights into the underlying mechanisms involved. The scientific challenge is the identification of the chemical and structural mechanisms by which the dopant is incorporated into the UO_2 , how this interacts with chemically reactive fission products and/or creates any intermediate product phases, and the comparison of this mechanism with related processes in relation to other actinide surrogate oxide species, such as PuO_{2+x} . Our understanding of the role of dopant or fission products embedded in the UO_2 (or PuO_2) lattice in irradiated fuels is also incomplete. Thus, the use of synchrotron based X-ray diffraction and X-ray absorption fine structure (XAFS) spectroscopy technique is of utmost interest. The ability of XAS, both extended X-ray absorption fine structure (EXAFS) and X-ray absorption near edge structure (XANES) to yield atomic scale structural information and chemical information, has been well documented in the literature.

2 Materials and Methodology

This chapter presents the materials that have been investigated in this study, along with their irradiation histories, the sample preparation methods used for handling them considering the radioactivity limits, and the analytical techniques that have been employed to investigate these materials.

2.1 Fuel materials used

In the present study, standard UO_2 and chromia-doped UO_2 fuels have been analyzed. Table 2.1 and Table 2.2 list the properties of the analyzed UO_2 fuel samples and the respective sample denominations. The final fuel specimens that have been investigated are, hereafter, named as FSF (fresh standard fuel), FDF (fresh doped fuel), BSF (BWR-irradiated standard fuel), BDF (BWR-irradiated doped fuel), and PSF (PWR-irradiated standard fuel), and -C and -R stand for center and rim, respectively.

Table 2.1: Details of the BWR fuel samples investigated.

Fuel type	Sample name	Average pellet burnup (MWd/kgU)	Fissile ^{235}U content (wt. %)	Cr content ($\mu\text{g/g}$)	Average grain size in fresh fuel pellet (μm)
Standard UO_2	FSF	–	4.9	< 5	10
	BSF (-C/R)	68.5	4.95	< 5	10
Chromia-doped UO_2	FDF	–	4.95	1080	48
	BDF (-C/R)	68.7	4.95	1080	48

The samples mentioned in Table 2.1 have been used for the studies of unit cell modifications (Chapter 4), local strain energy quantifications (Chapter 5), and defect calculations (Chapter 6). In addition, samples FDF and BDF have been used for chemical state determination of dopant Cr (Chapter 7).

Table 2.2: Details of the PWR fuel samples investigated.

Fuel type	Sample name	Average pellet burnup (MWd/kgU)	Fissile ^{235}U content (wt. %)	Cr content ($\mu\text{g/g}$)	Average grain size in fresh fuel pellet (μm)
Standard UO_2	FSF	–	4.9	< 5	10
	PSF (-C/R)	39.3	4.91	< 5	10

The FSF and PSF samples mentioned in Table 2.2 have been used for chemical speciation studies of matrix element U and actinide Pu (Chapter 8). Furthermore, TEM investigations of PSF samples have been presented in Chapter 9.

The UO_2 fuel pellets, investigated in this project, had an enrichment of $\sim 4.9\%$ of ^{235}U . The average grain size of fresh standard UO_2 fuels has been observed to be about 8-10 μm , whereas the grain sizes are enhanced by doping with additives, such as chromia, to roughly about 60 μm .

The fuels have been irradiated at the Swiss commercial nuclear power plants – KKL and KKG (BWR and PWR, respectively). The doped and standard fuel pellets of similar burnup values (*i.e.*, ~ 40 MWd/kgU and ~ 68 MWd/kgU) have been irradiated in the same fuel assembly under practically identical irradiation conditions (burnup cycles, neutron exposure, *etc.*) in the reactor.

2.2 Sample preparation methods

The methodologies used for sample preparation of the materials were predominantly determined by whether they were non-irradiated or irradiated.

For the fresh fuel, the sample preparation was relatively uncomplicated. Fuel specimens were extracted from a fresh UO_2 pellet, and wedge-shaped samples were created using the pre-thinned near-apex method. It was crucial to generate thinner regions to facilitate micro-beam XRD analysis in transmission mode.

For the irradiated fuel, however, the sample preparation was done remotely in the PSI HotLab facility by various trained specialists. This is because of the extremely high radioactivity of the irradiated fuel pellets. The procedure implemented for sample preparation depended upon the type of experiment to be performed.

2.2.1 EPMA investigations

The Electron Probe Micro-Analyzer (EPMA) used for our experiments is well-equipped to handle high radiation dose rates due to its placement within a shielded cell inside the HotLab facility. Hence, it was possible to take the entire fuel pellet inside the instrument for analysis.

For the sample preparation, the fuel pellet was cleaned using an ultrasonic bath for about a minute. Then, the fuel pellet was embedded in a one-inch steel sample holder with EPOFIX™ resin, followed by several rounds of polishing using CAMEO and Buehler APEX plates with water and diamond paste polishing suspensions (1 μm and 0.25 μm). The pellet was then subjected to a couple of turns of successive ultrasonic cleaning, followed by carbon-coating. The coating with carbon is necessary as it forms a conductive electron-transparent layer on the surface to minimize the charging effects on the sample by conducting the excess electrons away from the highly focused electron beam used during EPMA analysis. The polished and carbon-coated fuel pellet is then transferred to the EPMA instrument for measurements. The instrument used for EPMA measurements is a shielded JEOL 8500F microprobe coupled with field emission gun and four wavelength dispersive spectrometers (WDS).

The entire sample preparation was performed remotely in different hot cell compartments in the PSI HotLab.

2.2.2 Replica print

Owing to the very high dose rates of the irradiated fuel pellets, it is not suitable for synchrotron analysis in accordance with the radioactivity limits allowed for measurements at the respective PSI-SLS beamlines. For this purpose, the so-called peeling method or replicate method was used for sub-sample preparation.

Figure 2.1 details the various steps used for sample preparation via the replica method.

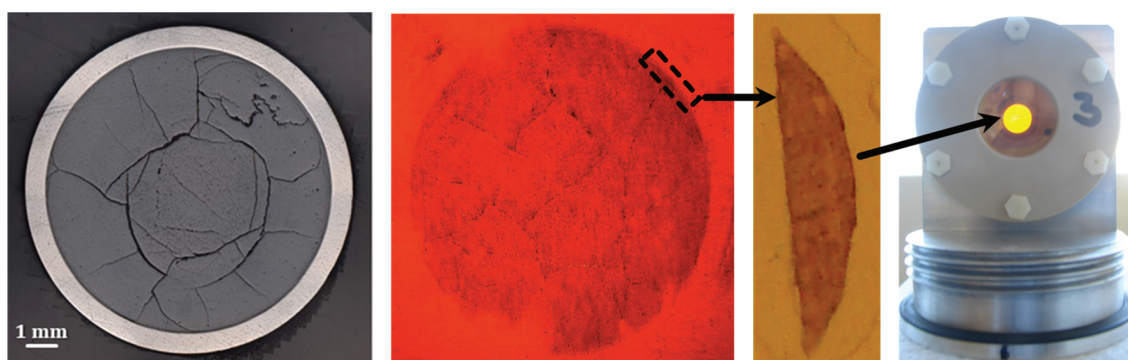


Figure 2.1: Sample preparation via replica method.

The surface of a fuel pellet was lightly ground under conditions for precision grinding using silicon carbide paper, which resulted in loose fuel particles on the surface. This method involves a turning-and-grinding process to produce micron-sized particles, and the instantaneous locations of the loose particles on the pellet surface were preserved as much as possible. The surface containing the freed particles was then printed on an adhesive Kapton tape, thereby “replicating” the pellet surface on the tape. The activity of the printed tape is also very high, so to further reduce the dose rate, several smaller strips were cut containing the regions of interest. These cut-strips ($\sim 2 \times 2 \text{ mm}^2$) contain only a couple of micron-sized fuel particles, which ensures the radioactivity is well below the permissible dose limits. The cut strips are then mounted inside the specialized radioactive sample holder, suitable for transport.

2.2.3 FIB milling

The Focused-Ion-Beam (FIB) instrument is a very effective tool used for micrometric sub-sample preparation. The FIB instrument utilizes a finely focused beam of ions, usually Ga^+ ions as also in our case, to image (in low current mode) or sputter, mill and polish (in high current mode) highly selective targeted regions of the sample. Most often, the FIB is used in combination with a Scanning Electron Microscope (SEM) that facilitates high resolution imaging and direct characterization of the sample. In our case, the FIB-SEM was used to prepare very small samples suitable for synchrotron micro-beam investigations as well as Transmission Electron Microscope (TEM) studies.

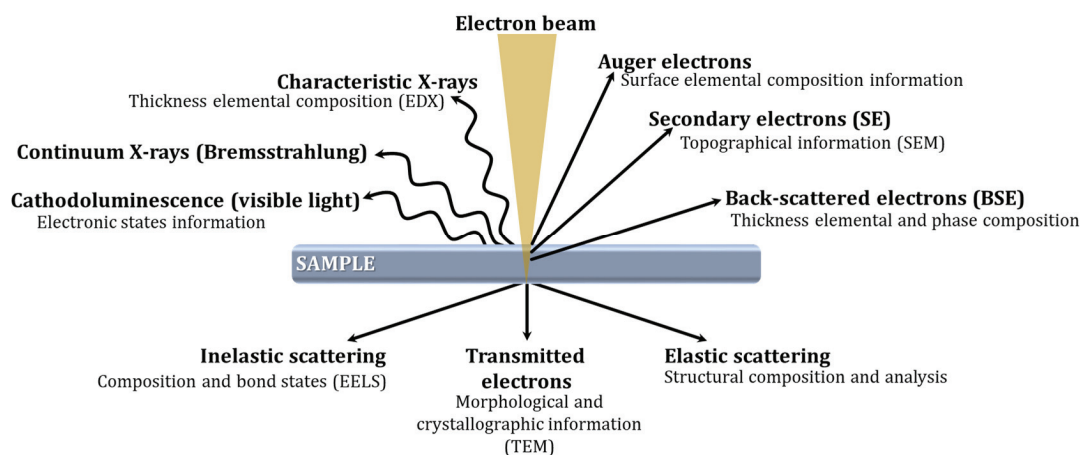


Figure 2.2: Types of interactions of electron with matter.

The SEM utilizes a highly focused electron beam and electromagnets to produce a high resolution and largely magnified image of the sample. When electrons interact with the atoms of the target sample, there occurs (a) elastic and inelastic electron scattering, and (b) photon and X-ray production in the electron-interaction volume. Figure 2.2 summarizes the interactions of electron with matter. Out of these, the SEM detects the emitted secondary electrons and back-scattered electrons to image the sample.

The back-scattered electrons (BSE) originate due to elastic collision of the primary electrons from the incident beam with the target atoms, thereby changing the trajectories of the electrons. Since lighter atoms scatter electrons less strongly as compared to heavier atoms, therefore, they generate a lower signal. As a consequence, BSE images distinguish very well the differences in atomic number, *i.e.*, heavier elements appear brighter. On the other hand, the secondary electrons (SE) are a result of inelastic collision of the primary electron beam and the sample. Since these SE have much less energy as compared to BSE, most of these get lost within the bulk of the matter due to self-shielding effects. The surface secondary electrons escape and reach the detector, and hence, SE images provide detailed information about the sample surface.

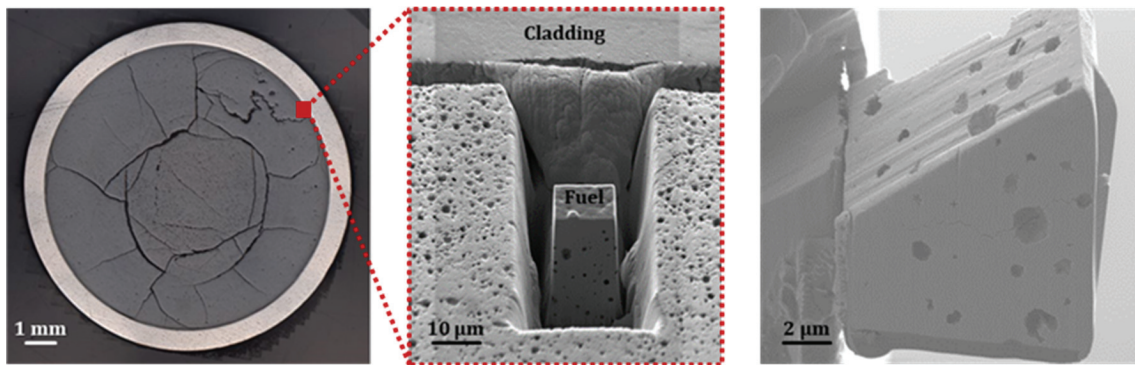


Figure 2.3: Sample preparation via FIB-SEM for synchrotron analyzes.

In the next step, FIB-milling was done to produce sub-samples from targeted regions of the irradiated fuel pellets, as shown in Fig. 2.3. The interaction of Ga^+ ion beam with the sample is similar as in the case of electron beam (refer to Fig. 2.2), however, owing to the much higher kinetic energy of the Ga^+ ions, it causes a sputtering of the surface atoms of the sample. The FIB-SEM instrument used for milling is a shielded Zeiss Crossbeam XB 540, equipped with WDS, EDS and EBSD detectors. By virtue of selection of specific milling shapes and areas in the target sample, it facilitated the preparation of finely polished tiny fuel specimens of dimensions roughly $30 \times 30 \times 30 \mu\text{m}^3$. Such thin samples are not only required for reducing the radiological risks, but it also allowed to perform synchrotron-based micro-beam X-ray diffraction studies in the transmission mode.

2.3 Beamline setup and experimental conditions

The synchrotron light based investigations involving the techniques of X-ray fluorescence (μXRF), X-ray diffraction (μXRD), X-ray absorption fine structure (μXAFS) were performed at the microXAS (X05LA) and PHOENIX (X07MA/B) beamlines of the Swiss Light Source facility (PSI-SLS). The SLS provides a highly intense photon flux beam, with a beam current of 400 mA and electron energy of 2.4 GeV in the storage ring.

The end-stations of different beamlines operate at different energy ranges, and this enables the identification and analysis of a broad spectrum of elements. Table 2.3 lists the excitation energies and fluorescent energies of the elements analyzed in this study.

Table 2.3: Excitation energies (in keV) and fluorescent energies (in keV) of the elements of interest analyzed.

Energy (keV)		Elements		
		Cr	U	Pu
Excitation energy	K 1s	5.989	115.606	121.791
	L _I 2s	0.696	21.757	23.104
	L _{II} 2p _{1/2}	0.584	20.948	22.266
	L _{III} 2p _{3/2}	0.574	17.166	18.057
Characteristic X-ray energy	K α ₁	5.415	98.439	103.734
	K α ₂	5.405	94.665	99.525
	K β ₁	5.947	111.300	117.228
	L α ₁	0.573	13.615	14.279
	L α ₂	0.573	13.439	14.084
	L β ₁	0.583	17.220	18.294
	L β ₂	–	16.428	17.255
	L γ ₁	–	20.167	21.417

2.3.1 microXAS (X05LA) station

At the microXAS beamline, the undulator facilitates the emission of high-brightness X-rays with an energy range of 3-23 keV, complemented by the capability of micro-focusing. By utilizing the liquid nitrogen-cooled Si(111) double-crystal Bragg monochromator, the microXAS beamline can be configured to deliver monochromatic X-rays of desirable photon energy. The X-ray beam on the sample was focused to get a spot size of 1 μm \times 1 μm dimension. The end-station of the microXAS beamline, showing the sample stage and the various detectors, is shown in Fig. 2.4.

A specialized radioactive specimen holder, engineered to accommodate vertical sample orientation, was placed on a three-axis motion manipulator to ensure precise sample positioning in relation to the photon beam. The standard beam-sample-detector geometry was followed, wherein the detector was horizontally positioned at an angle of 45° to the incoming beam, and the sample was mounted at a 10° angle from the vertical plane of the beam direction. The sample holder was designed to enable μXRF , μXRD and μXAFS measurements of active samples. The local lead shielding of the end-station allows highly radioactive samples to be investigated at this beamline.

All diffraction and absorption data were acquired at room temperature (295 K). An ultrathin Si-diode was used to measure the incident X-ray intensities. In order to minimize the self-absorption effect, fluorescence signals were measured, using a SiLi drift solid state detector (SSD) from KETEK, at grazing exit geometry. The first step involved the localization of the irradiated fuel particles on the adhesive Kapton tape and determination of the region of interest for the XRD and XAS analyses. For this purpose, μ XRF mapping with a high spatial resolution was undertaken. Furthermore, μ XRD was performed at the same area as μ XRF so that a direct comparative relation can be made for the sample position and the diffracting volume. For μ XAFS measurements, sub-regions of interest were chosen from the μ XRF map.

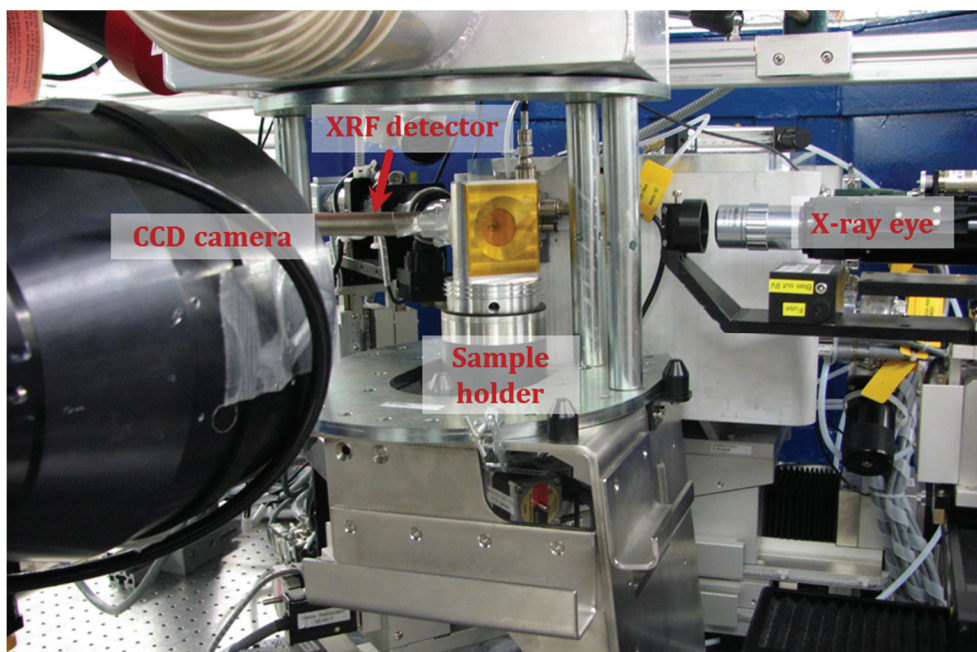


Figure 2.4: The end-station of the microXAS (X05LA) beamline, used for the measurements of the radioactive fuel specimens.

With regard to μ XRD measurements, a monochromatic beam of desirable energy was used, and a charge-coupled device (CCD) camera (from Photonic Science, UK) was employed to record the diffraction patterns in transmission mode, with a beam exposure time on the sample ranging from 2-5 seconds. The CCD camera was shielded from the non-scattered X-rays using a tungsten '*beam stop*'. The sample-detector distance, rotation and tilt angles were calibrated by recording Laue diffraction patterns of reference corundum (α -Al₂O₃) powder sample.

2.3.2 PHOENIX (X07MA/B) station

The experiments at the PHOENIX beamline are performed inside a high vacuum chamber ($\sim 10^{-5} - 10^{-6}$ mbar pressure) at room temperature (295 K). The Apple-II undulator delivers tunable soft X-rays restricted to the 0.8-8 keV energy range, which is necessary to investigate the absorption edges of low-Z elements, such as K-edge of Cr. The μ XRF and μ XANES analyses were performed with a focused beam of dimensions roughly $2\text{ }\mu\text{m} \times 1\text{ }\mu\text{m}$.

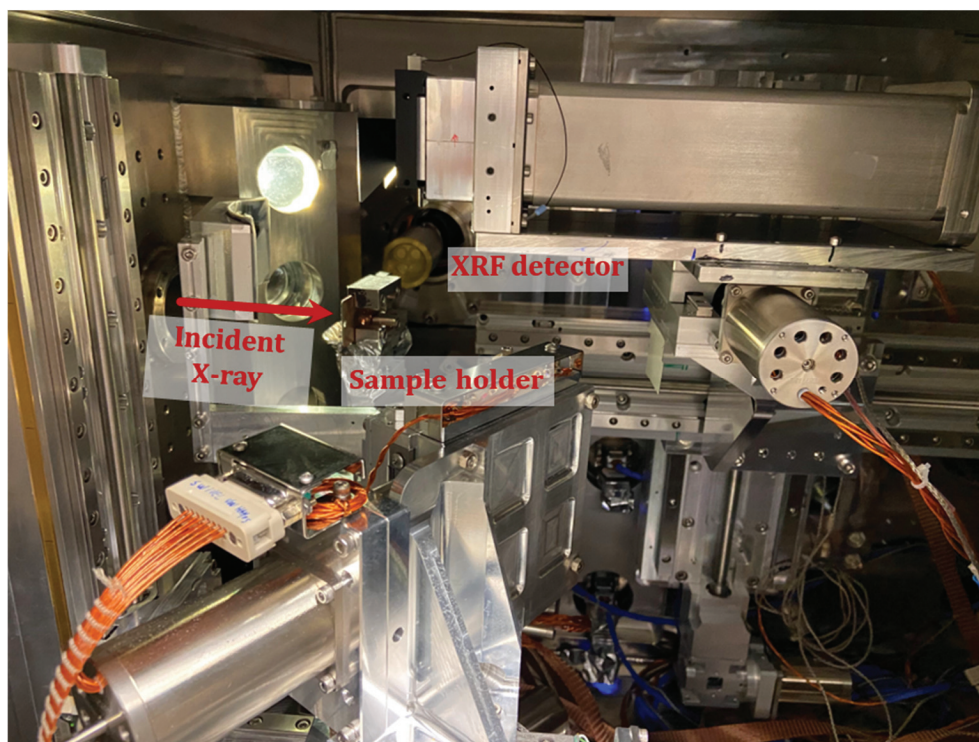


Figure 2.5: The end-station of the PHOENIX (X07MA/B) beamline.

Fuel specimens were measured in a scattering chamber under high-vacuum conditions, which enabled the detection of very low concentrations of Cr present in the DF specimens and yielded high counting rates to give higher peak intensities for the Cr-XRF signal emitted from the samples. The μ XRF uranium and chromium maps, obtained with high spatial resolution, were used to localize the sampling areas in the fuel samples. XANES measurements were performed at ambient temperature and the fluorescence X-rays were recorded at a grazing exit geometry and using a four-element silicon detector. Multiple XANES energy scans in every measurement location for a given specimen were recorded and averaged to improve the data statistics and the signal to noise ratio. Figure 2.5 shows the end-station of the PHOENIX beamline.

2.4 Experimental data reduction

2.4.1 XRD data

Captured Laue images were processed and analyzed using Fit2D [80] and XRDUA [81] software. These codes allow both the interactive mode as well as the batch mode for processing large data sets.

The first step in the XRD data analysis was the calibration of the XRD detector, and determination of the Bragg angles in relation to the positions of the diffraction spots appearing in the CCD images. For this purpose, quantitative XRD measurements have been made using a standard Al_2O_3 powder sample (reference material), for which the crystal structure is well known. This is an important step, which has been used to determine the sample-detector distance, the rotation and tilt angles of the CCD and other global parameters related to the experimental setup.

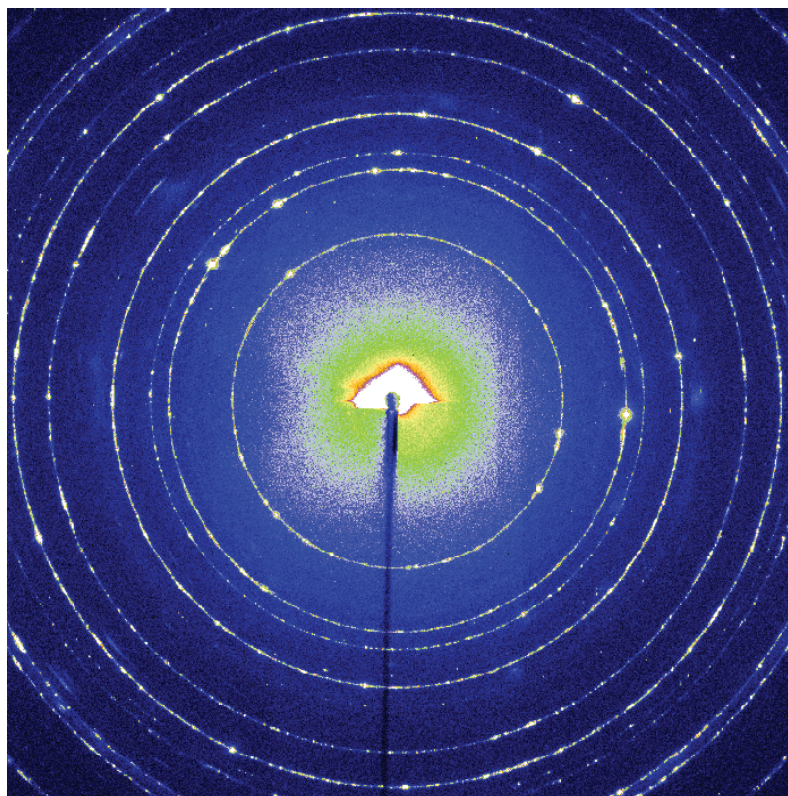


Figure 2.6: An example of a two-dimensional μXRD pattern acquired from corundum $\alpha\text{-Al}_2\text{O}_3$ powder sample measured at 17.2 keV energy.

An example of a two-dimensional diffraction pattern obtained from the Al_2O_3 reference powder sample is shown in Fig. 2.6. The 2D diffraction pattern of Al_2O_3 powder reveals concentric Debye rings corresponding to various $\{hkl\}$ reflection planes of the sample,

captured out to 35° (2θ value). This diffraction range, measured in units of 2θ , represents the scattering angle between the incident beam and the diffracted X-rays. The detection range depends on both the sample-detector distance as well as the width of the CCD.

Debye rings are the equivalent of Bragg's peaks in a 2D XRD image, and each ring corresponds to a particular d -spacing or 2θ angle in the 1D diffraction spectrum. Since a direct correspondence exists between the radial coordinates and the peak positions in the XRD spectrum, integration over a given angular range has been performed in the radial direction to obtain the average peak intensities versus 2θ plots, as shown in Fig. 2.7 as an example.

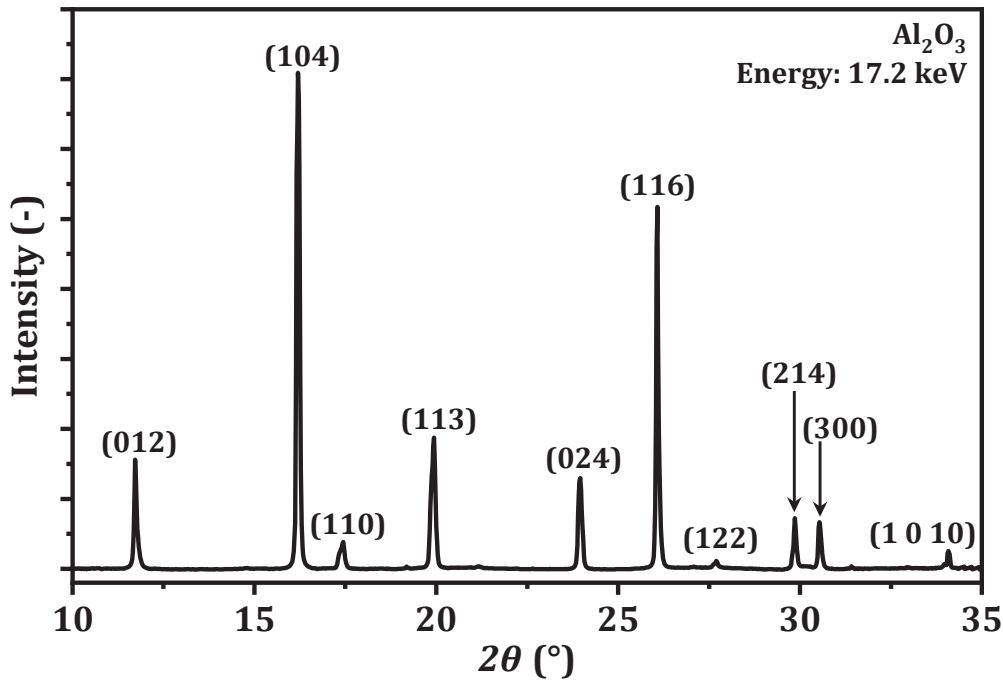


Figure 2.7: Example of 1D diffraction spectrum of reference Al_2O_3 powder sample.

The standard deviation of the d -spacing of different $\{hkl\}$ planes, obtained by analyzing the XRD data of Al_2O_3 powder is shown in Fig. 2.8. Along the ordinate are values of standard deviations that correspond to error bars for each data point representing a given interplanar spacing of the crystalline Al_2O_3 plane. Comparing the standard errors between data points, one can observe that the error in the low d value region is low. This implies that lower d -spacing (or higher 2θ) peaks in the measured XRD spectra should be preferred in the determination of peak centroids since the error associated with each of them is substantially smaller than those of low-angle Bragg peaks. Therefore, for enhanced precision, the (220) and (331) reflections of UO_2 (marked in red in Fig. 2.8) were specifically chosen, which provided a measurement accuracy of $\pm 0.002 \text{ \AA}$.

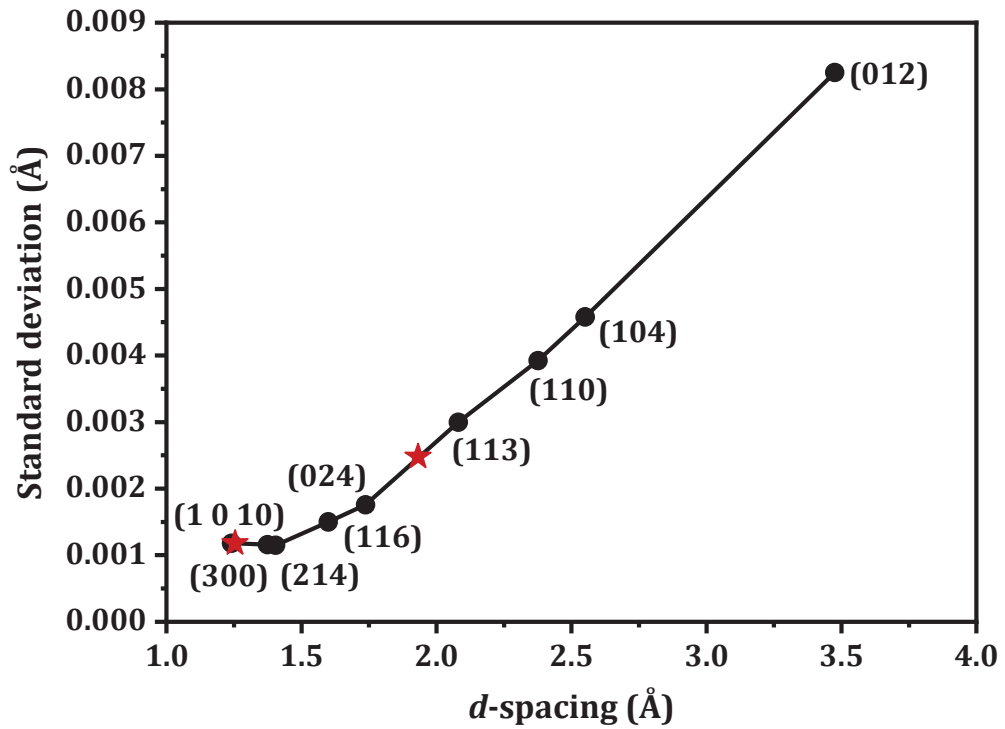


Figure 2.8: Plot of standard deviation on d -spacing versus d -spacing, obtained by analyzing the XRD data of reference Al_2O_3 sample.

The second step was the analysis of the XRD data measured from fresh and irradiated fuels, both standard and chromia-doped UO_2 materials. Uranium dioxide belongs to the fluorite crystal family, and its crystalline structure takes the $\text{Fm}\bar{3}\text{m}$ (225) space group. The stoichiometry and crystallinity of UO_2 play very important roles for its nuclear fuel related applications. In a perfectly stoichiometric and well-crystallized product, UO_2 adopts a cubic structure and uranium atoms are octahedrally coordinated with oxygen atoms in the unit cells of the lattice network (as shown in Fig. 2.9).

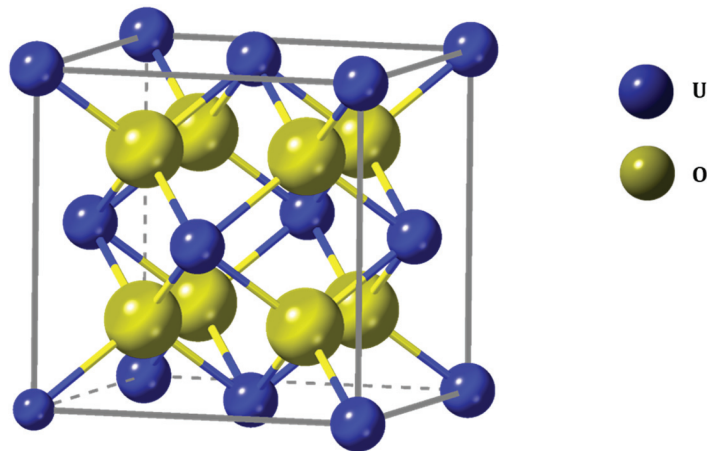


Figure 2.9: The cubic fluorite unit cell of uranium dioxide.

After careful visual analyses of many Laue diffraction photographs obtained in a Laue μ XRD map, a set of single-spot Laue images from several different spot locations within the mapped UO_2 sample have been selected and individually processed by the XRDUA Laue data reduction package. The pixel intensities in each 2D- μ XRD image were integrated radially to yield corresponding 1D-XRD patterns. In the final step of data reduction, 1D-XRD plots have been extracted which plot the diffracted intensity of various Bragg reflections from the $\{hkl\}$ planes as a function of the radial angular positions (2θ values). All the X-ray $\{hkl\}$ peaks of the XRD-pattern were indexed using the Match program [82]. Selected diffraction $\{hkl\}$ peaks were fitted using a symmetric Pseudo-Voigt function to determine the angular centroid positions ($2\theta_{hkl}$) and full width at half-maximum (FWHM) in the one-dimensional line profile analyses. The $2\theta_{hkl}$ values thus obtained were used to determine interplanar distance d_{hkl} of the $\{hkl\}$ reflection for UO_2 crystal using the Bragg formula [83].

The next step involved the analysis of the XRD data set of irradiated standard and Cr-doped UO_2 fuel specimens, using the batch-wise processing tool available in the XRDUA software, in order to obtain a quantitative evaluation of the residual strain present in spent fuel materials. The in-plane lattice strain in irradiated UO_2 crystallites is estimated by measuring the shift of the Bragg peaks (*i.e.*, $2\theta_{hkl}$ angular positions in a diffraction pattern) relative to those from the fresh (unstrained) UO_2 fuels. We have probed the strain distribution within small areas at local regions to the neighborhood of irradiated UO_2 crystallites using microscale XRD measurements, and obtained 2D residual strain maps of the irradiated UO_2 crystals in the spent fuel specimens. For this purpose, the 2D Laue images, collected at each point in the high-resolution raster scan on the UO_2 fuel particles, have been analyzed using the XRDUA software in a batch-wise processing mode (details in Appendix A). These μ XRD results, which provide two-dimensional strain maps in the investigated specimens, will be presented and discussed in greater detail in Chapter 5.

Lastly, to investigate irradiation induced damage accumulation and dislocation density evolution with burnup, a set of single-spot Laue diffraction images (*i.e.*, μ XRD CCD frames) were carefully selected from the whole μ XRD mapping data sets, and each 2D- μ XRD image was processed and analyzed using the Fit2D software package [80]. In the data reduction phase, specific Laue spots originating from the same family of $\{hkl\}$ lattice planes in a given single frame Laue image were selected and converted to ψ - 2θ space. It creates 2D images to provide the azimuthal (ψ) angular distributions of the intensities (given by image pixel intensities) against the radial angles (2θ) of those selected Laue spot patterns. In particular, we have analyzed the azimuthal width of recorded Laue spots and determined the dislocation density in irradiated fuel specimens. A more detailed description of the data reduction process from 2D- μ XRD images to characterize Laue spots can be found in Refs. [84,85].

2.4.2 XAS data

XAS data processing and analysis [both, X-ray absorption near edge spectra (XANES) and extended X-ray absorption fine structure (EXAFS) spectra] were performed using the computer program Demeter [86]. The background subtraction in the pre-edge and post-edge regions of experimental spectrum was done using the *autobk* algorithm. Thereafter, the background-removed EXAFS function $\chi(k)$ was extracted and normalized by the edge jump height. The $\chi(k)$ was then multiplied by k to emphasize the higher k region. The EXAFS function was Fourier transformed (FT) into real space with k weighting factor to obtain the radial distribution function (RDF). In the next step, the extracted experimental EXAFS signals were best-fitted to the well-known EXAFS equation [87]. Theoretical backscattering amplitude and phase shift functions, needed for the curve fits, were calculated using the FEFF code for a fluorite lattice of pure UO_2 cluster with a unit cell parameter of 5.472 Å. The set of optimized structural parameters derived from the fits were coordination number (N), bond length (R), and Debye-Waller factor (σ). The degree of mismatch between the fitted theoretical standard and the data is given by the EXAFS \mathcal{R} -factor [88], a standard measure of the quality of the fit.

2.5 Theoretical approach to the experimental techniques

The following sub-sections provide the theoretical explanations of the experimental techniques implemented for this thesis. Most of the studies are done with non-destructive synchrotron light, whereas electron beam analyzes have also been performed and discussed.

2.5.1 X-ray fluorescence (XRF)

X-ray fluorescence (XRF) is a non-destructive analytical technique that utilizes the interaction of X-rays with matter to determine its elemental composition. Broadly, there are four main types of interactions between X-rays (or photons) and matter (Fig. 2.10), which are as follows:

- (1) **Elastic scattering** occurs due to elastic collision between the incident photon and the electrons of the matter. Since the collision is elastic, the energy of the photon remains unchanged before and after the collision.
- (2) **Photoelectric absorption** of the photon occurs when the photon transfers all of its energy to an inner shell electron. When the energy of the incident photon is higher than the binding energy of the inner shell electron, the electron gains sufficient kinetic energy to be ejected out of the atom. This electron vacancy makes the atom unstable, and to regain its stability, the vacancy is replaced by higher energy (outer shell) electron. During the process of transition from the outer shell to inner shell, the electron loses its extra energy in the form of

characteristic X-rays, named so since they are characteristic of a given element. Another possibility is the absorption of the emitted characteristic X-ray by another outer shell electron resulting in the emission of the Auger electron.

- (3) **Compton scattering** occurs when the photons undergo inelastic collision with a single electron of the matter. After the event of collision, the energy of the incident photon gets shared between the scattered photon and the electron.
- (4) **Pair production** occurs when the incident photon of sufficient energy interacts with the atomic nuclei and gets converted into an electron-positron pair.

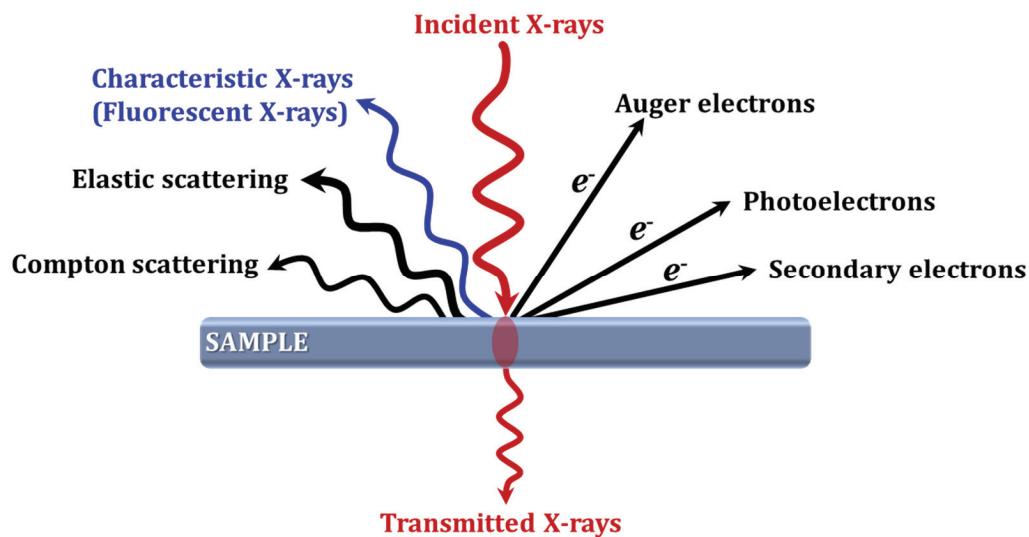


Figure 2.10: Types of interactions of X-rays (photons) with matter.

During the process of photoelectric effect, the transition of an outer shell electron to fill up the inner shell vacancy is associated with the emission of characteristic X-rays, the energy of which is equivalent to the differences in the binding energies of the respective shells. The energy levels corresponding to each element are unique, and hence, the emitted X-rays are also characteristic of each element. This property allows for non-destructive characterization of elemental composition of a sample. This emission of characteristic X-rays is referred to as *X-ray fluorescence (XRF)*, and the analytical technique is called *X-ray fluorescence spectroscopy*.

Characteristic X-rays are classified as K, L, M, or N, indicating their specific electronic shell origin. Further designation of α , β , γ , *etc.* signifies which higher energy shell was involved in the electron transition process. For instance, a K_{α} X-ray arises from an electron transitioning from the L to the K shell, while a K_{β} X-ray results from an electron transitioning from the M to the K shell, and so on. From L shell onwards, each shell comprises multiple orbits with varying binding energy levels for electrons, further distinction is made using $\alpha 1$, $\alpha 2$, $\beta 1$, $\beta 2$, *etc.* (along with the shells – K, L, *etc.*) to signify

the electronic orbit involved in the transition. A schematic representation of the K and L series electronic transitions is shown in Fig. 2.11.

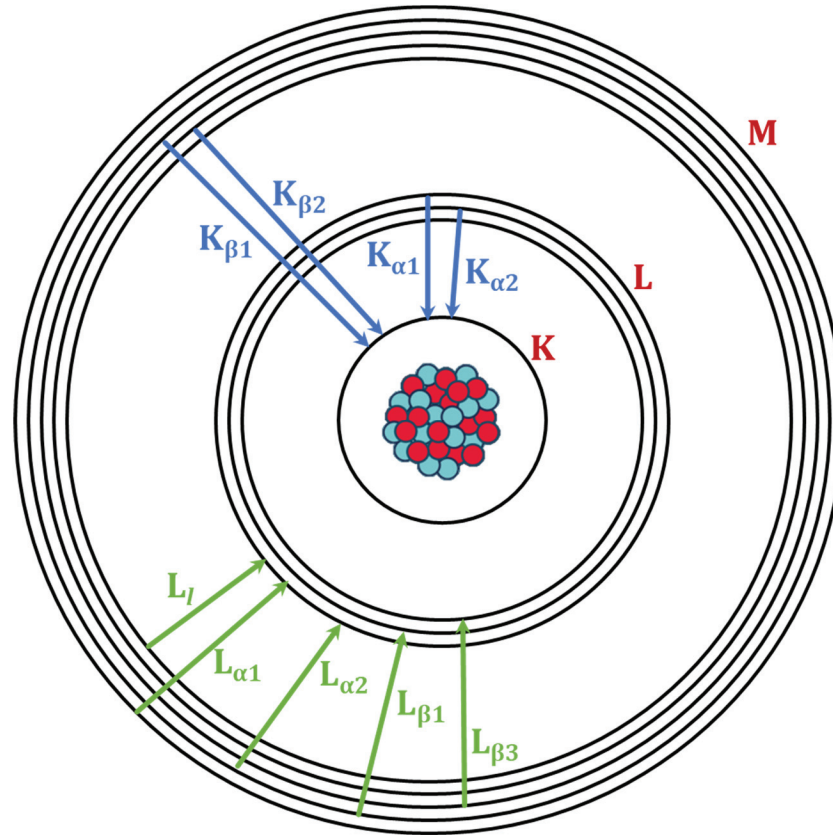


Figure 2.11: Schematic representation of K and L series electronic transition.

This thesis involves XRF investigations done using synchrotron based X-rays. It is worth noting that fluorescent X-rays can also be generated using any other primary excitation sources such as alpha-particles, protons, or high energy electron beam (as in EPMA).

2.5.2 X-ray diffraction (XRD)

X-ray diffraction (XRD) is a non-destructive analytical technique that utilizes the constructive interference between the incident X-rays and the atoms of the crystalline materials for phase identification and crystallographic structure determination. When a beam of mono- and/or polychromatic X-rays is incident on a crystalline material, the atoms of the crystals, by virtue of their orientation, cause the X-rays to diffract in certain specific directions.

Crystals exhibit ordered arrangement of atoms. The atoms, or more specifically the electrons of the atoms, scatter the incoming X-ray waves, thereby generating secondary spherical waves. During the process of elastic scattering (or *coherent scattering*) of incident X-rays, a uniform arrangement of scatterers (*i.e.*, the atoms' electrons)

generates a uniform array of spherical waves. In most directions, these waves interfere with each other destructively and nullify the effect of one another. However, in certain directions, they behave constructively.

Laue diffraction, discovered by Max von Laue in 1912, is traditionally used for the determination of single crystal orientation. In this method, a single crystal, with their regular array of atoms, behaves as a three-dimensional diffraction grating for white X-rays. The diffracted X-rays are subsequently recorded, typically on a photographic film, as an array of spots on an elliptical or hyperbolic curve creating the *Laue pattern* (or *Laue diagram*), as shown in Fig. 2.12. Each Laue spot is indexed to a particular plane.

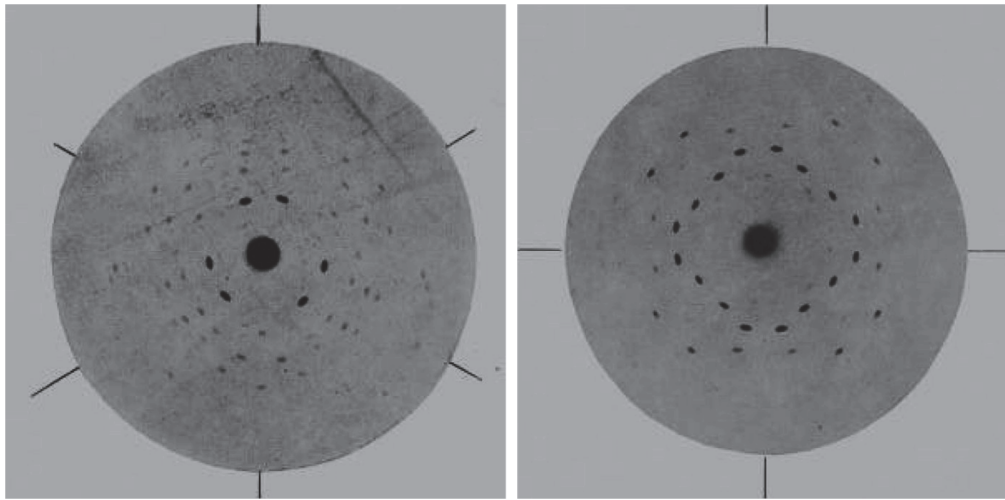


Figure 2.12: Laue photographs of zinc blende (presented by Laue, Friedrich and Knipping on June 8, 1912, at Königlich Bayerische Akademie der Wissenschaften) [89].

The Laue diffraction method can be performed in two ways, namely– the *back-reflection method* and the *transmission method*. In the back-reflection method, the film is positioned between the X-ray source and the crystal. The diffracted beams reflected in the backward direction are captured and recorded, and the diffracted spots are arranged typically on a hyperbola. On the contrary, in the transmission Laue method, the photographic film is present behind the crystal to capture the diffracted beams that pass through the crystal. In this case, the diffracted spots appear on an elliptical curve.

Bragg's law, developed by William Henry Bragg and William Lawrence Bragg, based on experimental results confirmed the findings of Laue. In contrast to Laue, Braggs considered a crystal as layers of atoms, wherein each layer behave similarly to a reflecting plane (*i.e.*, angle of incidence is equal to the angle of reflection).

The Bragg's law states that for constructive interference of X-rays to occur, the path difference of the X-rays reflected by successive atomic planes within a crystal must be

equal to an integral multiple of the wavelength of the incident beam. Mathematically, the Bragg's law is represented as:

$$2d \sin \theta = n\lambda \quad (2.1)$$

Figure 2.13 is a schematic representation for the derivation of Bragg's law showing the uniformly spaced planes of atoms in a crystal.

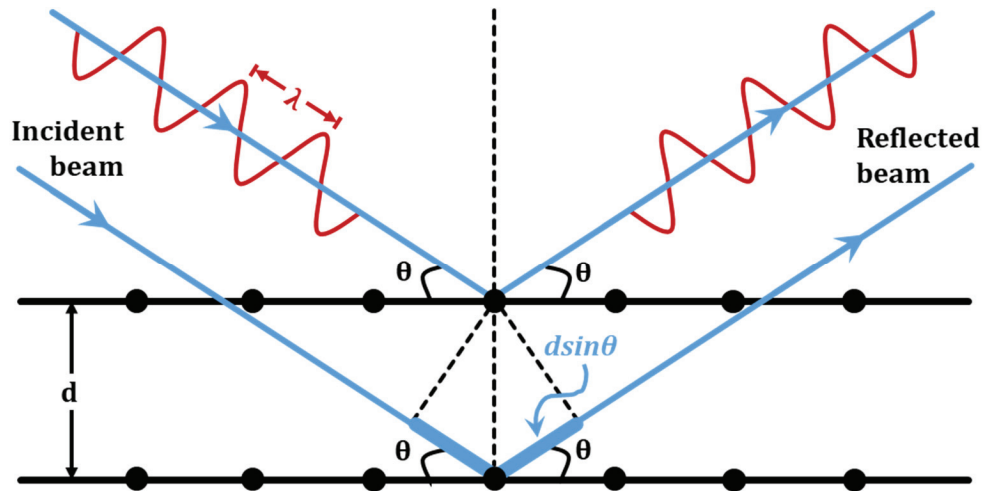


Figure 2.13: Schematic representation of the Bragg diffraction. X-ray with wavelength λ is incident on a crystal of symmetrical arrangement of atoms having interplanar spacing as d at an angle θ . The optical path difference travelled by the two waves is equal to $2d\sin\theta$.

XRD is a powerful and highly versatile tool for crystal structure analysis in diverse fields. In this thesis, XRD investigations have been done using synchrotron light. Using micro-beam X-ray Laue diffraction to probe irradiated fuel specimens, microstructural changes of standard and doped UO_2 have been studied, such as the modified unit cell structure, in-plane residual strain and remnant dislocation content.

2.5.3 X-ray absorption fine structure (XAFS)

X-ray absorption fine structure (XAFS) or *X-ray absorption spectroscopy (XAS)* is an element-specific non-destructive analytical technique that utilizes the phenomenon of absorption of X-rays by the atoms at energies near or above their core-level binding energies. The chemical and physical environment of the absorbing atom affects its X-ray absorption probability, which is given by the absorption coefficient, μ . In XAFS experiments, the modulation of μ is investigated to determine the local electronic and geometric structure of the absorbing atom, such as the valence state and coordination number of the absorber, bond distances with neighboring atom species, *etc.*

Owing to their high energy (~500 eV to 500 keV), X-rays undergo photoelectric absorption through all matter. When the energy of the incident X-rays (E) is higher than the binding energy of the core-level electron (E_0), this electron is ejected from its quantum level by absorbing the energy of the X-ray photon (equivalent to its binding energy, E_0), and the excess energy (*i.e.*, $E - E_0$) is transferred to the ejected photoelectron in the form of kinetic energy. Hence, the momentum (p) of the ejected photoelectron with mass (m) can be expressed as:

$$p = \sqrt{2m(E - E_0)} \quad (2.2)$$

According to de Broglie equation [90], the wavelength (λ) is related to a particle's momentum (p) and Planck's constant (h) as follows:

$$\lambda = \frac{h}{p} \quad (2.3)$$

Using Eq. (2.2) and Eq. (2.3), the wavelength of the photoelectron (λ) can be expressed as:

$$\lambda = \frac{h}{\sqrt{2m(E - E_0)}} \quad (2.4)$$

However, not all X-ray photons are absorbed. The absorption probability of X-rays by the sample is given by the absorption coefficient (μ) in accordance with the Beer-Lambert's law, as follows:

$$I = I_0 e^{-\mu t} \quad (2.5)$$

where, I_0 is the intensity of the incident monochromatic X-ray beam, and I is the intensity of the transmitted X-ray beam after passing through the sample of thickness t .

Alternatively, in the fluorescence mode, the absorption coefficient can be related to the incident intensity (I_0) and the resulting fluorescent beam intensity (I_f), as follows:

$$\mu \propto \log(I_f/I_0) \quad (2.6)$$

In most cases, the absorption coefficient can be expressed in terms of the X-ray energy (E), density of the sample (ρ), atomic number (Z) and atomic mass (A) of the absorbing atom, as follows:

$$\mu \approx \frac{\rho Z^4}{AE^3} \quad (2.7)$$

During an XAFS measurement, the sample is probed with X-rays over a range of energy starting from $E < E_0$ to $E > E_0$. In simple terms, an XAFS measurement is the measure of the intensity of μ as a function of energy, at and above the E_0 of the selected atom. As

$E \rightarrow E_0$, there occurs a sharp rise in the intensity of μ due to photoelectric effect. The first inflection point of this sharp rise is called the *absorption edge* and corresponds to E_0 .

Figure 2.14 represents the XAFS spectrum of uranium, which has an L₃-edge excitation energy of 17.17 keV.

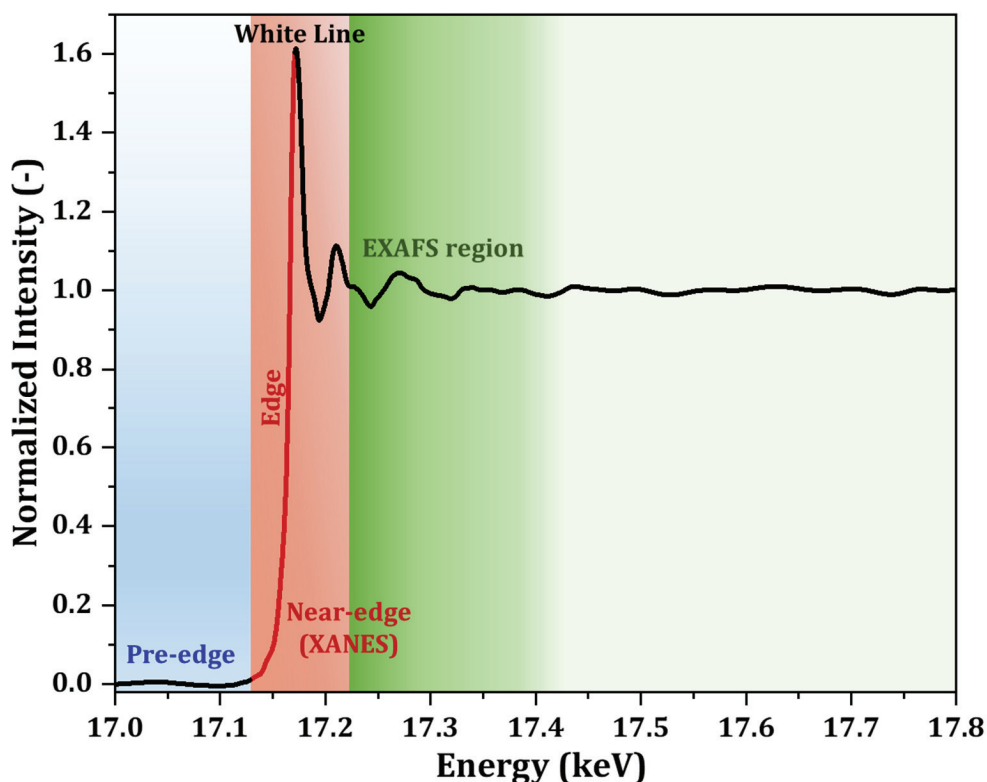


Figure 2.14: Typical L₃-edge XAFS spectrum of uranium.

Typically, a XAFS spectrum can be broadly divided into the following regions:

- (1) **Pre-edge region** where no ionization has taken place. This region contains information regarding the orbital symmetry and Fermi-level in the molecule.
- (2) **Edge** is the main rising part of the XAFS spectrum, and corresponds to the excitation energy (E_0) of the absorbing atom.
- (3) **XANES (X-ray Absorption Near Edge Structure)** is the region 50–60 eV above the edge. This region has characteristic features, and provides information about the electronic and geometric structure of the absorber.
- (4) **EXAFS (Extended X-ray Absorption Fine Structure)** is the region beyond near-edge, usually at $E > E_0 + 50 \text{ eV}$. This region contains information about the geometric structure around the absorber atom.

In some cases, commonly observed for oxides, is another feature called *white line* which refers to a large prominent peak just above the edge, especially in L- or M-edge spectra. The white line feature is more typical for transition metal oxides or rare earth metal oxides, due to empty orbital bands of electronic states.

Explanation of the EXAFS equation:

Some approximations are needed for the quantitative interpretation of the oscillations in the EXAFS region. Empirically, the EXAFS function, $\chi(E)$, is defined as:

$$\chi(E) = \frac{\mu(E) - \mu_0(E)}{\Delta\mu_0(E_0)} \quad (2.8)$$

where, $\mu(E)$ is the measured absorption coefficient, $\mu_0(E)$ is the estimated absorption coefficient of the isolated atom, $\Delta\mu_0(E_0)$ is the measured jump in the intensity of absorption coefficient at energy E_0 .

For better understanding of the EXAFS function, it is more convenient to consider the wave nature of the electron, and therefore, represent the EXAFS function in terms of the wavenumber, $\chi(k)$, of the ejected photoelectron. The wavenumber, k , in units of \AA^{-1} , is expressed as:

$$k = \frac{2\pi}{\lambda} = \sqrt{\frac{2m(E - E_0)}{\hbar^2}} \quad (2.9)$$

According to quantum mechanics, the final state of the ejected photoelectron can be expressed in terms of a spherical wave propagating outwards and centered around the absorber atom. In the case of an isolated atom, the $\mu_0(E)$ shows a sharp rise at E_0 and becomes a smooth function well above the absorption edge, as shown in Fig. 2.15(a). However, in the case of interaction with neighboring atoms (also referred to as *backscattering atoms*), the ejected photoelectron is scattered by the neighboring atoms back to the absorber atom, thereby, causing an interference with itself, as shown in Fig. 2.15(b). A constructive interference between the outgoing and backscattered waves takes place when the two waves are completely in phase. They interfere destructively when the outgoing and the backscattered waves are out of phase. The amplitude and phase of the backscattered photoelectron wave varies with energy and hence, causes the oscillations of $\mu(E)$ in the EXAFS region. The type, number, and distance of the backscattering atoms around the absorber atoms determine the amplitude of the backscattered waves, and uniquely modify the free atom absorption. Therefore, EXAFS provides information of the geometric structure (such as, coordination number, bond distances, *etc.*) around the central absorbing atom.

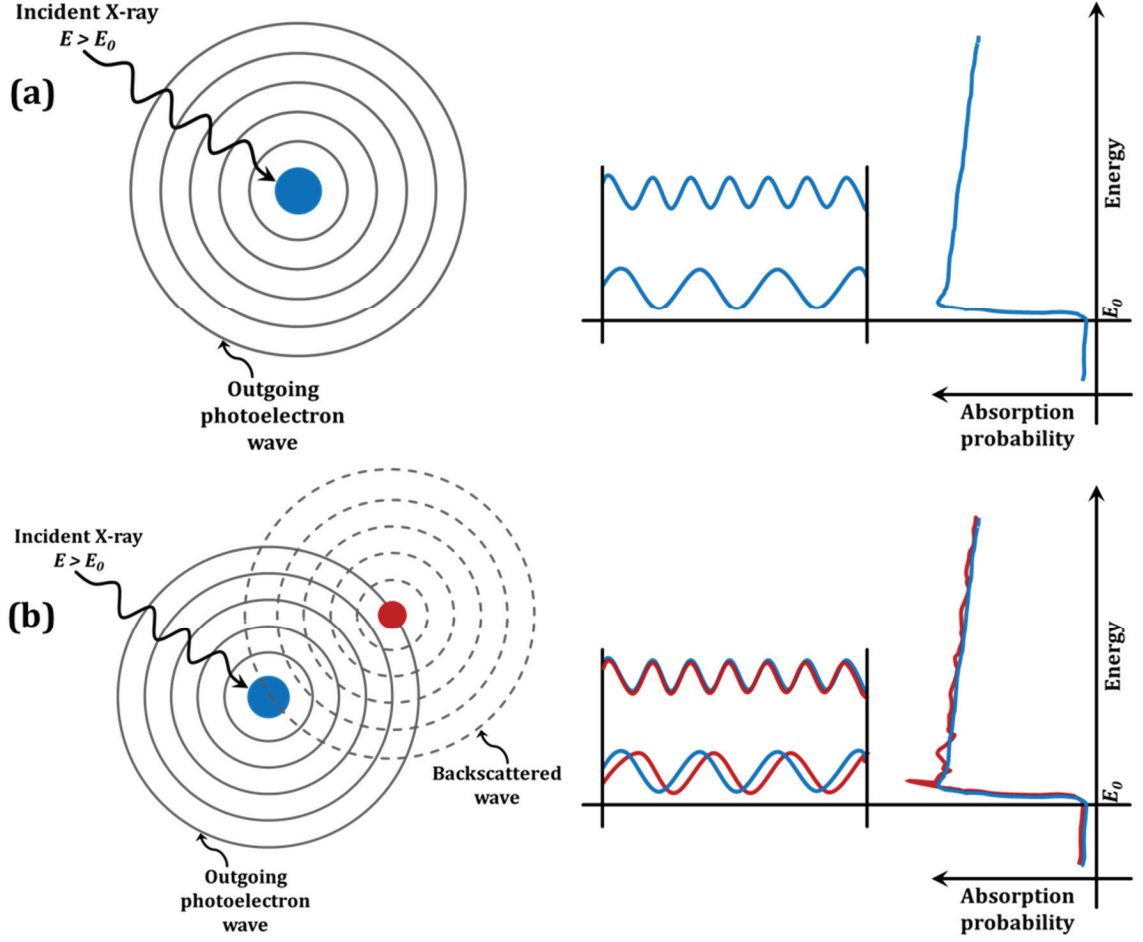


Figure 2.15: (a) Graphical representation of X-ray absorption by an isolated atom. (b) Graphical representation of X-ray absorption in a multi-atom system, wherein the outgoing photoelectron wave experience interference (both constructive and destructive) effect with itself due to the presence of backscattering atoms. Adapted from [91,92].

For deriving the EXAFS expression, it is assumed that the photoelectron undergoes only single scattering and has relatively high kinetic energy (~ 30 eV) when it is ejected out of the absorbing atom. The EXAFS equation as a function of $\chi(k)$ can be represented as:

$$\chi(k) = \sum_{i=1}^n A_i(k) e^{-\beta_i(k)} \cdot \sin \Phi_i(k) \quad (2.10)$$

where, the summation is done over all the *scattering paths* for the ejected photoelectron. The $\chi(k)$ consists of three factors – $A_i(k)$, $e^{-\beta_i(k)}$ and $\sin \Phi_i(k)$. The factor $A_i(k)$ represents the amplitude of each wave, the second exponential factor $e^{-\beta_i(k)}$ is the damping factor, and the third factor $\sin \Phi_i(k)$ results from the phase shifts of the photoelectron.

The sine function can be further elaborated as follows:

$$\sin \Phi_i(k) = \sin(2kR_i - \phi_i(k)) \quad (2.11)$$

The argument of the sine function is made up of two terms– $2kR_i$ and $\phi_i(k)$. The term $2kR_i$ arises due to the phase shift of the photoelectron as it is ejected out of the absorbing atom, gets backscattered from a neighboring atom at a distance R_i , and finally returns to the absorber. An additional phase shift $\phi_i(k)$ occurs due to the spatially varying potentials of the absorbing atom and the backscattering atoms experienced by the photoelectron.

The amplitude $A_i(k)$ of each wave is a function of several parameters, as follows:

$$A_i(k) = \frac{N_i S_0^2 |f_i(k)|}{k_i R_i^2} \quad (2.12)$$

where, N_i denotes the number of backscattering atoms in each shell, or *coordination number*, located at distance R_i from the absorbing atom. S_0^2 is an amplitude reduction factor and is related to inelastic scattering and multi-electron excitations. The last factor $f_i(k)$ is a complex function used to describe the scattering process.

The exponential damping factor is also a product, as follows:

$$e^{-\beta_i(k)} = e^{-\frac{2R_i}{\lambda(k)}} \cdot e^{-2k^2 \sigma_i^2} \quad (2.13)$$

In this equation, the first exponential factor, associated with the core-hole lifetime, is expressed as a function of the mean free path $\lambda(k)$ of the photoelectron. The second exponential takes into account the thermal motion and static disorder of the atoms distributed over an average radius of R_i . These factors are corrected using σ_i^2 , known as the *Debye Waller factor*.

The final EXAFS equation, considering the parameters from Eq. (2.11), Eq. (2.12) and Eq. (2.13), is given by:

$$\chi(k) = \sum_{i=1}^n \frac{N_i S_0^2 |f_i(k)|}{k_i R_i^2} e^{-\frac{2R_i}{\lambda(k)} - 2k^2 \sigma_i^2} \cdot \sin(2kR_i - \phi_i(k)) \quad (2.14)$$

The EXAFS equation, expressed as $\chi(k)$, can be converted into the real space by a Fourier transform to generate the *radial distribution function (RDF)* [93]. The peaks of the RDF spectra are associated to the radii of the scattering shells and gives the distances from the absorbing atom. The Fourier transform of $\chi(k)$ is given by [94]:

$$FT(R) = \frac{1}{2\pi} \int_{k_{min}}^{k_{max}} k^n \chi(k) e^{i2kR} dk \quad (2.15)$$

The advent of the Fourier transform rendered EXAFS a practical and effective experimental tool. From analyzing the EXAFS data, the structural parameters, such as coordination number, radial distance or bond length, and the mean square disorder of neighboring atoms, can be extracted. It is also possible to isolate the contribution of each individual shell, as the EXAFS is sensitive to different types of neighboring atoms due to their different atomic numbers.

The goodness of fit is given by the \mathfrak{R} -factor value, which measures the percentage misfit between a potential model for EXAFS data with the experimental data. A \mathfrak{R} -factor of 0.01 implies a very good fit, with the difference between the experimental data and theoretical curve equal to about 1%. Mathematically, the \mathfrak{R} -factor is described as [95]:

$$\mathfrak{R} = \frac{\sum_i |\chi^c(R_i) - \chi^e(R_i)|^2}{\sum_i \{\chi^e(R_i)\}^2} \quad (2.16)$$

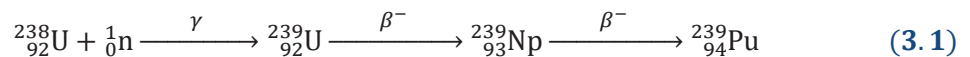
In this thesis, XAFS studies using synchrotron light has been undertaken to study the atomic structure and chemical speciation of U, actinide Pu and the dopant Cr in irradiated standard and doped UO₂ fuel specimens.

3 Local Burnup Determination by ^{148}Nd Method

In essence, accurate fuel burnup analyses are of practical importance to determine the performance of fuel [96] and/or for the identification of potential safety issues as well as economy of nuclear fuel management. For the purpose of local burnup estimation of the fuel particles, the PIE results of the analyzed fuels have been used to determine the radial burnup distribution in the PSF, BSF and BDF pellets by ^{148}Nd fission product monitoring method [97,98]. With this purpose, a more detailed EPMA quantitative analysis has been performed at a micro-scale spatial resolution for U, Pu, O, Nd as well as a variety of additional fission product elements present in the spent fuel pellets.

3.1 Burnup profile in the pellets

During irradiation, the matrix element ^{238}U absorbs epithermal neutrons thereby producing ^{239}U radionuclide, which successively decays by β^- -emissions to thermally fissile ^{239}Pu isotope. This is shown by the following nuclear reaction:



Since the maximum neutron absorption takes place at the peripheral region of a cylindrical UO_2 fuel pellet, the so formed plutonium concentration exhibits a maximum at the outer surface regions in the pellet and decreases towards the pellet center. For this reason, the subsequent fission events of this plutonium cause locally a much higher burnup in the outer zones in the pellet compared to that throughout the rest of the pellet, where the burnup is practically regarded as radially almost uniform [13,99].

Figure 3.1 shows the EPMA line scan profiles of U, Pu and O across the PSF pellet. It can be seen that the radial distributions of these elements are quite flat in the center region of the pellet. At the pellet edges, the concentration of U is decreased indicating a more pronounced consumption of uranium whereas that of Pu is increased, as expected, due to the higher probability of epithermal neutron resonance absorption at the peripheral regions of the pellet. The average plutonium concentration is about 0.79 wt.% at the pellet center, and the plutonium content has reached on average 2.70 ± 0.06 wt.% in the rim area of the UO_2 fuel.

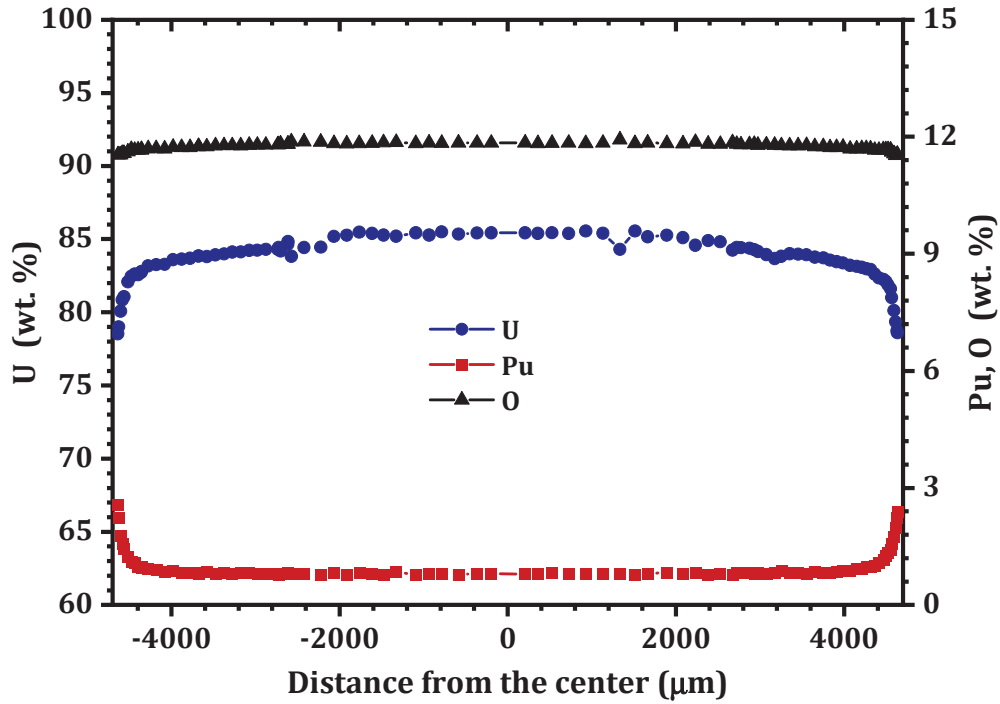


Figure 3.1: Radial distribution of the normalized U, Pu and O content in the spent fuel pellet PSF measured by EPMA.

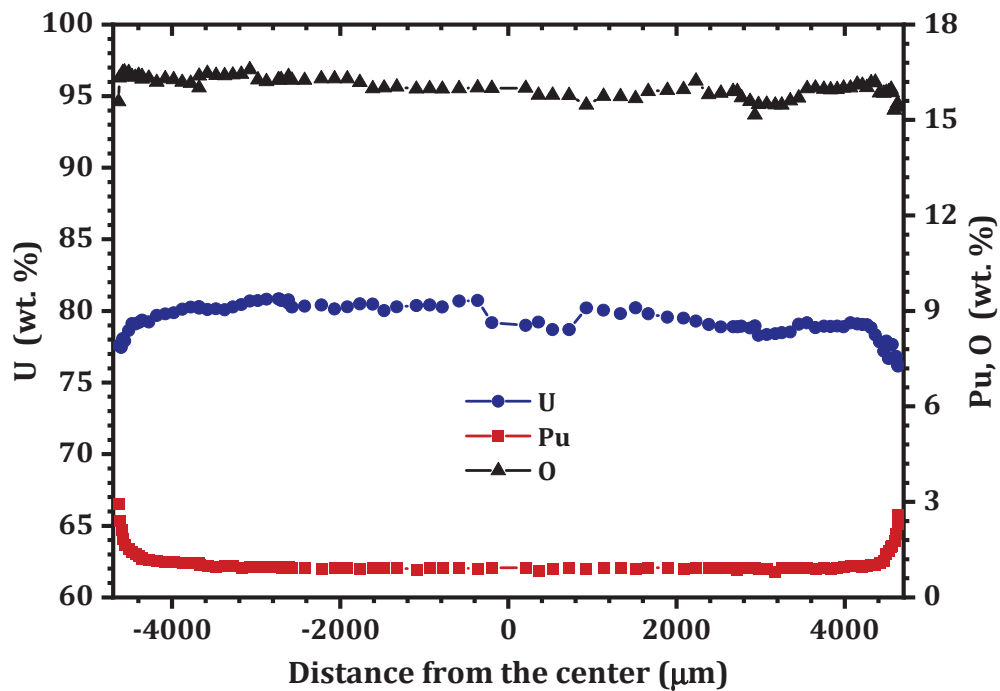


Figure 3.2: Radial distribution of the normalized U, Pu and O content in the spent fuel pellet BSF measured by EPMA.

The EPMA line scan profiles of U, Pu and O across the BSF pellet is shown in Fig. 3.2. The general trend observed in radial distributions of these elements in the UO_2 fuel matrix is similar to that of the PSF pellet, whereas the concentration profiles are slightly asymmetric mostly at the enhanced local burnup regions near the pellet edge. It indicates azimuthal non-symmetry in burnup distribution in the BWR pellet. The degree of burnup asymmetry is known to depend on the rod position within the fuel assembly, especially for BWR fuel [100]. Also, in the case of the BSF pellet with an average burnup of ~ 68.5 MWd/kgU, more uranium has been consumed and the average uranium concentration at the pellet center is about 80 wt.% whereas it is about 77 wt.% at the peripheral regions of the pellet. Regarding plutonium, the average concentration is about 0.92 wt.% at the pellet center and about 2.91 wt.% at the pellet rim.

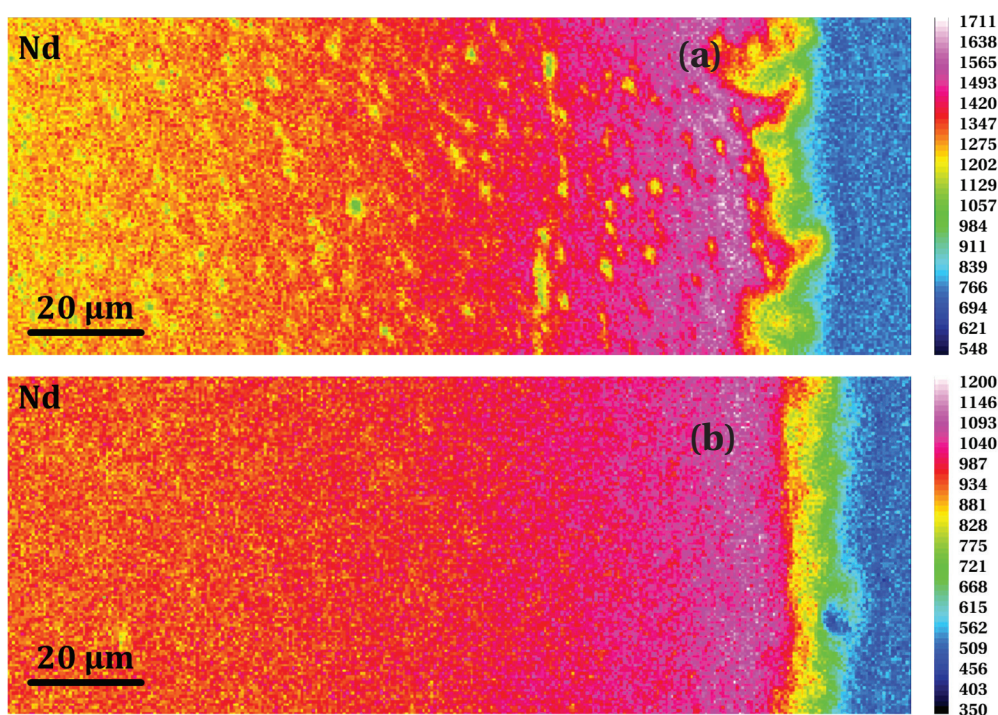


Figure 3.3: EPMA intensity maps of neodymium signal collected from the outer edge region of the (a) BSF and (b) BDF pellets.

To evaluate the radial burnup distribution in the spent fuel pellets, the fission product neodymium (^{148}Nd) which is known to give an indication of the local burnup [97,98], was analyzed by EPMA. The result of this procedure is used to deduce the burnup values of the micron-sized spent fuel particles analyzed by high spatial resolution ($1\ \mu\text{m}^2$) XRF, XRD and XAS measurements. Figure 3.3 shows the EPMA intensity maps of neodymium signal collected from the outer edge region (rim-zone) of the BSF and BDF pellets, showing fine-scale variations in the spatial distribution of the Nd content. Each map is presented in a temperature color display, where pink color represents areas with highest Nd intensity grading downward to red color, and light blue indicates a very low intensity

for the Nd yield at nearly the background level. It can be observed in the map that there is a pellet-cladding interaction layer (characterized by a light green coloration) formed at the pellet edge between the UO_2 fuel and the Zircaloy cladding (represented in blue color).

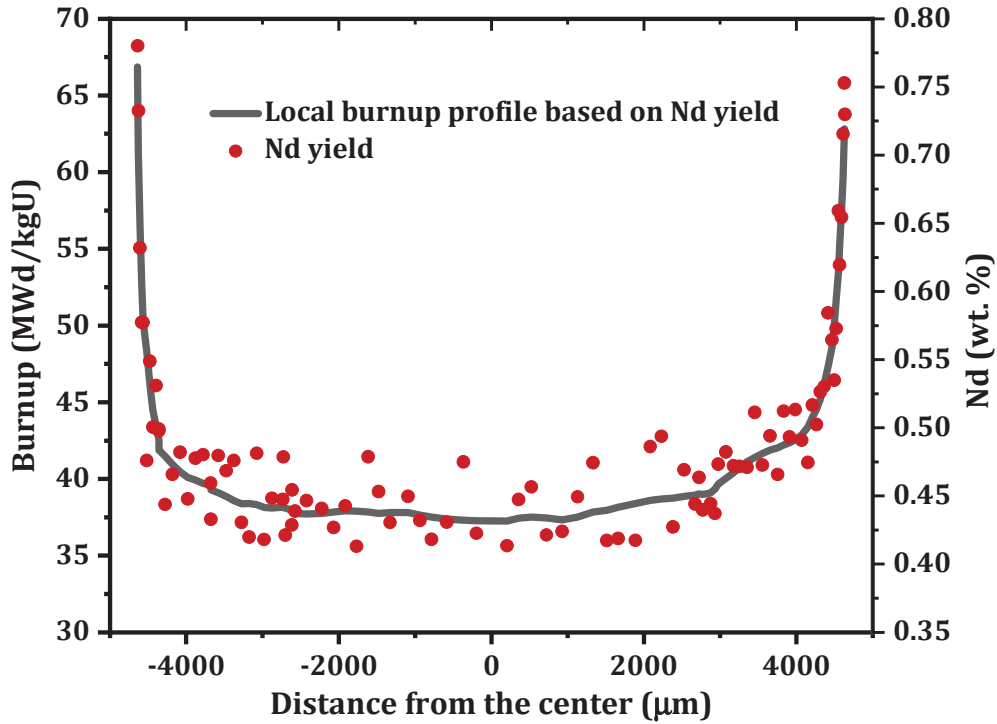


Figure 3.4: Quantitative EPMA of Nd and burnup distribution profile of PSF, measured (with 20 keV, 320 nA and ~300 nm electron beam spot size) along the diameter of the spent fuel pellet.

Figure 3.4 shows the measured radial distribution of Nd in the PSF pellet. The measured concentration profile indicates that in the center region of the fuel pellet, Nd distribution is flat with an average concentration of ~0.43 wt.%. This concentration is increased steeply, up to about 0.75 wt.%, at the pellet rim due to the higher fission rate of uranium and the fission of created plutonium. The estimated burnup profile, reported in Fig. 3.4, is obtained using weighted concentration values of the neodymium yield measured by EPMA, and utilizing the axial gamma scanning data of ^{137}Cs isotope collected from the post irradiation examination (PIE) results of the full-length mother fuel rod. The local burnup in the selected pellet is deduced by comparing the mean value of all measured gamma intensities in the rod with that at the axial position of the fuel pellet. It may be mentioned that the gross axial gamma scan analysis of the discharged rod was performed under a commercial proprietary PIE program, and a detail discussion of PIE results is beyond the scope of this thesis.

In Figs. 3.5 and 3.6, measured Nd concentration profiles obtained by EPMA across the BSF and BDF pellets, and calculated radial burnup distribution profiles against the Nd concentrations are shown. In both the cases, the radial concentration profiles indicate that the average Nd content is about 0.75 wt.% with a nearly uniform radial profile in the center region (at least within up to 1 mm) of both pellets. At the peripheral or rim region, the spatial Nd concentration profile rise sharply to reach a maximum of about 1.40 wt.% within a distance of $\sim 60\ \mu\text{m}$ in the pellets. The EPMA results show that the width of the rim-zone of both BSF and BDF pellets is about $75\ \mu\text{m}$ in the spent fuels.

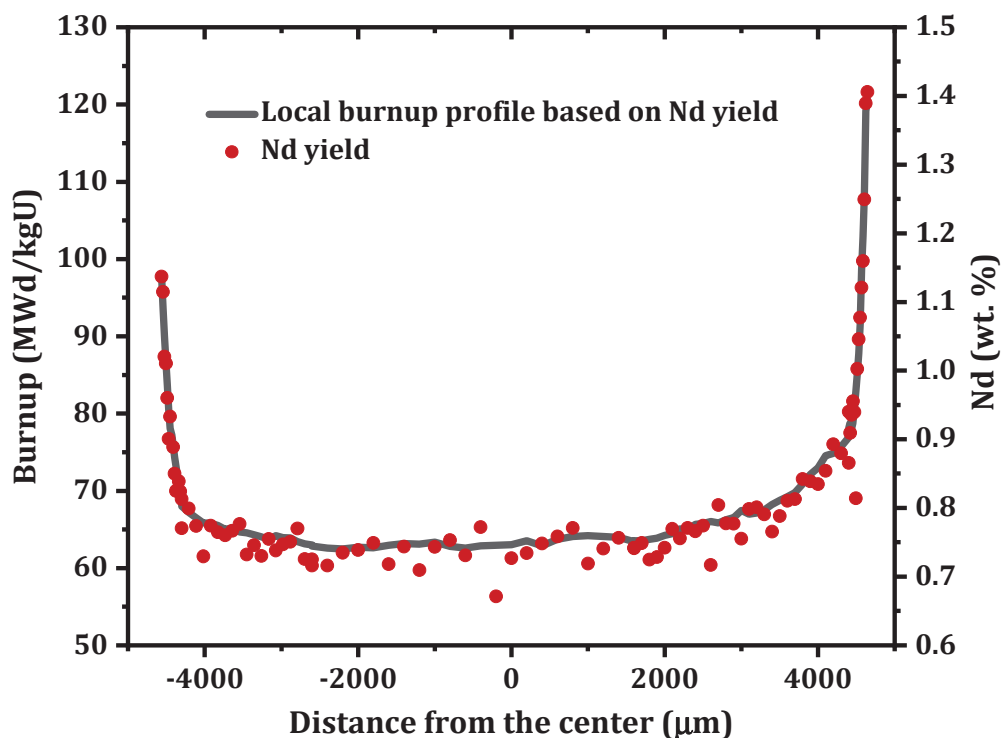


Figure 3.5: Quantitative EPMA of Nd and burnup distribution profile of BSF, measured (with 20 keV, 320 nA and $\sim 300\ \text{nm}$ electron beam spot size) along the diameter of the spent fuel pellet.

The calculated radial burnup distribution profiles against Nd concentrations for the two UO_2 pellets (BSF and BDF) are also displayed in Figs. 3.5 and 3.6. These burnup curves reveal that the burnup distribution in the central part of the pellets is quite uniform with an average local burnup of about 68 MWd/kgU, and the fuel burnup has reached up to 120 MWd/kgU at the pellet periphery. These specific burnup values in units of % FIMA (Fission per Initial Metal Atom) are equivalent to the burnup values of about 7.1% and 12.5% FIMA, respectively (scaled by a conversion factor of 9.6 related to BWR fuels). It may also be noted from Figs. 3.5 and 3.6 that the radial burnup profiles are not symmetric with respect to the central region of the UO_2 pellets, and the local burnup is slightly different at two opposite angular orientations (0° and 180°) for both pellets. PIE results have indicated that this analysis can be related to the fuel pin bundle

configurations, original assembly location of the bundle and neutron moderation in the reactor core.

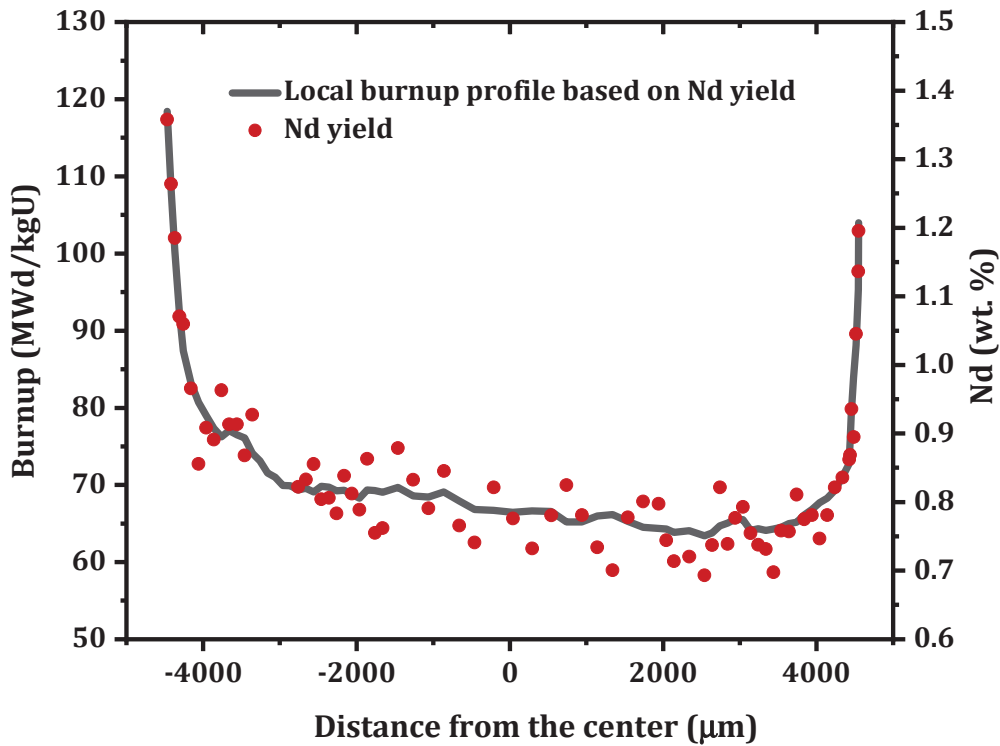


Figure 3.6: Quantitative EPMA of Nd and burnup distribution profile of BDF, measured (with 20 keV, 320 nA and ~300 nm electron beam spot size) along the diameter of the spent fuel pellet.

The burnup distribution data and quantitatively measured local Nd concentration data for the radial profiles of PSF, BSF and BDF pellets are used to obtain information about the local burnup at various sampling locations within the micron-sized UO_2 particles analyzed by high spatial-resolution μXRF , μXRD , μXAS and TEM measurements on the investigated specimens. Values of the fuel burnup obtained by this method with neodymium monitor are derived with a typical accuracy of ~5%, generally applicable for the low concentration Nd content analysis by EPMA.

4 Lattice Parameter Evolution in UO₂

This chapter describes the burnup dependence of microstructural evolutions that occur in UO₂ during irradiation, investigated at the atomic level. It is also of particular interest to compare the in-pile behavior of chromia-doped fuel with undoped standard UO₂ fuel. The study deals with changes in the UO₂ crystallinity investigating the lattice parameter evolution as a function of fuel burnup, brought about by FPs incorporation and neutron irradiation-induced defects. Structural characterization of the prepared fuel samples (FSF, FDF, BSF and BDF) has been carried out using a combined μ XRF and μ XRD synchrotron experiment in a scanning mode. The scanning micro-diffraction measurements provide local information from every small illumination area ($\sim 1 \mu\text{m}^2$) on the sample. The local burnup of each sampling area in the spent fuel specimens was determined from the local concentration of the fission product Nd measured by EPMA (details in Chapter 3). In addition, EPMA data of other FPs as well as activation products have been obtained from irradiated standard and DF pellets to determine the effect of their incorporation in the lattice on predicting the UO₂ lattice parameter evolution in spent fuels.

4.1 Micro-beam XRF and XRD analyses

Scanning micro-beam XRD measurements at room temperature have been performed at the microXAS beamline of the PSI-SLS facility (details in Section 2.3.1). The detailed features of the diffraction instrument and experimental arrangement for investigating highly radioactive fuel materials have been presented in previous publications [83,101].

For the purpose of the present study, a monochromatic X-ray beam of 17.2 keV energy has been focused to a spot size of $1 \mu\text{m} \times 1 \mu\text{m}$ at the sample location, and Laue diffraction features have been recorded on a large-area X-ray charge coupled device (CCD) camera (MAR CCD X-ray detector), in transmission mode. The incident photon energy and the sample-to-detector distance of CCD have been calibrated using the K-edge excitation energy (17998 eV) of Zr in a zirconium metal foil and high-quality alumina powder, respectively. The XRF signals are obtained by an energy dispersive Si detector placed normal to the incident X-ray beam and a grazing exit arrangement.

Before the μ XRD/ μ XRF data collection began, a high-resolution optical microscope was used to determine the sampling locations of UO₂ particles in all specimens on a rough micrometer scale by micrometer driven stages. Thereafter, the fuel specimens were

scanned through the focused X-ray beam using a motorized XY translation stage with (sub)-micron spatial resolution. At each step increment ($1\text{ }\mu\text{m}$ X-ray beam spot size, $1\text{ }\mu\text{m}$ step size and 1 s acquisition time per step) within the scanned region of a specimen, a Laue pattern is recorded, thereby collecting the series of Laue diffraction images using a combination of μXRF and μXRD mapping approaches. The μXRF uranium maps, obtained with high spatial resolution, were used to localize the micron-sized spent fuel particles present on the adhesive Kapton tape, and the changes in the crystallinity of UO_2 were studied using the μXRD with a correlation map representing the spatial variation in the UO_2 crystalline lattice at the micro length scale.

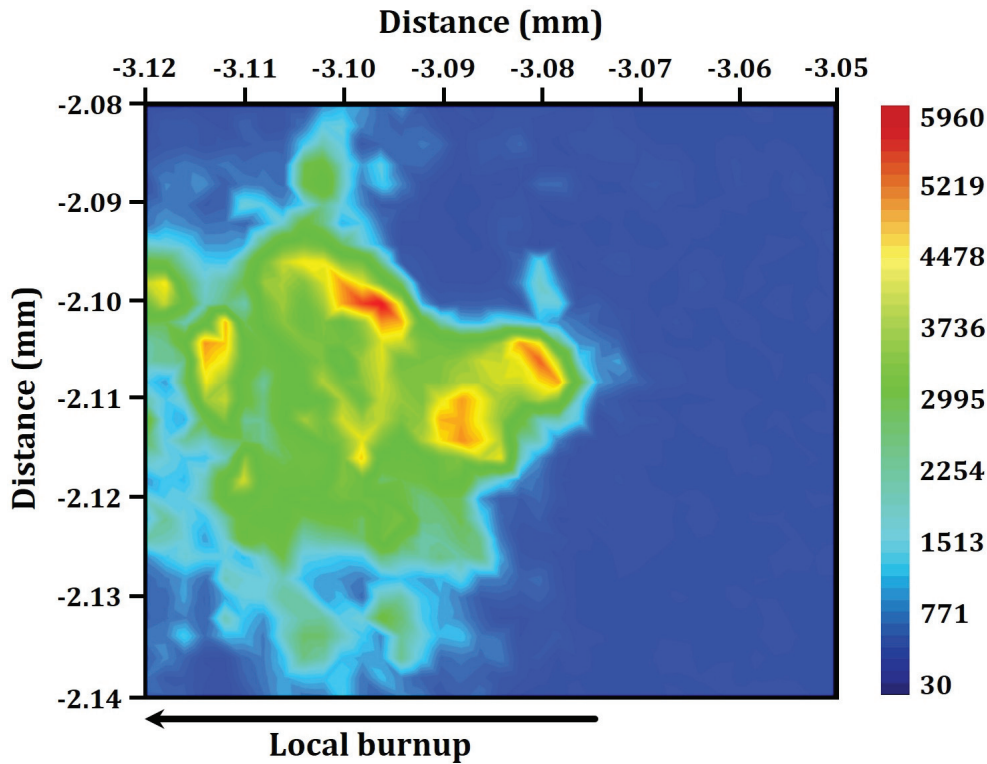


Figure 4.1: Elemental uranium distribution recorded by μXRF mapping from the BDF-R specimen.

An example of a μXRF uranium map (obtained using the La X-ray emission lines), recorded over a $70\text{ }\mu\text{m} \times 60\text{ }\mu\text{m}$ area from the BDF-R specimen, is displayed in Fig. 4.1. Each pixel along the two spatial dimensions in the map corresponds to a specific position of the beam on the specimen and contains an independent XRD frame, and the full field μXRF image comprises more than 1000 CCD frames. The color bar of the RGB color space in the map is represented in arbitrary units with the blue and red color corresponding to lowest and highest uranium concentration, respectively. The μXRF map in Fig. 4.1 shows that the shape of the UO_2 particle is irregular, however, large enough (mean length of about $50\text{ }\mu\text{m}$) to obtain spatially resolved structural information by the μXRD scans. It may be mentioned here that the observed color variation in the μXRF image (Fig. 4.1) is possibly related to the local thickness variation within the

sampling area of the UO₂ spent fuel particle. In the current study, therefore, single-spot Laue diffractograms of the high-resolution scanning μ XRD measurements have been selected from regions where the total volume of the material probed by μ XRD appears rather similar.

4.2 Evaluation of UO₂ lattice parameter

The interplanar distance d_{hkl} values for different $\{hkl\}$ lattice planes of UO₂ have been obtained by straightforward calculations based upon the Bragg's equation:

$$2d_{hkl} \cdot \sin\theta_{hkl} = \lambda \quad (4.1)$$

where, θ_{hkl} is the measured Bragg angle of the $\{hkl\}$ reflection, and λ denotes the wavelength of the incident X-ray. However, due to experimental limitations and uncertainties inherent in the standard calibration process of Laue CCD images given by the standard deviation σ parameter [81], only the experimental result of a high order reflection peak in the high angle 2θ range from 33.1° to 33.6°, *i.e.*, the peak of the (331) interplanar spacing is considered to determine the unit cell constant of the fluorite-type UO₂ lattice using the known relationship between d_{hkl} and the lattice constant, a , of cubic crystal systems given by:

$$a^2 = d_{hkl}^2 \times (h^2 + k^2 + l^2) \quad (4.2)$$

In the present study, the UO₂ unit cell lattice parameter for all fuel specimens is measured with an accuracy of $\pm 2 \times 10^{-3}$ Å [83]. Also, it has to be mentioned that XRD results of the UO₂ lattice constants for industrial-grade FSF and FDF pellets have been previously reported [83] and, therefore, are not discussed in great detail. The experimental results have revealed that doping of UO₂ powder with 0.16 wt.% chromia powder (*i.e.*, equivalent to 1080 μ g/g Cr content) causes a slight lattice contraction of the fluorite-type UO₂ unit cell compared with dopant-free UO₂ fuel. This phenomenon can be ascribed to the effects of cationic substitution of U⁴⁺ by Cr³⁺ ions as well as the redox activity of chromium ions with UO₂ crystallites [83,102]. The lattice parameter (a_0) for the FSF and FDF are found to be 5.472 ± 0.002 Å and 5.468 ± 0.002 Å, respectively. These results are consistent with the experimental results and theoretical investigations on chromia-doped fuels fabricated in the same way under suitable sintering conditions for industrial applications [103].

As a representative example, typical XRD patterns collected from the FDF specimen and the irradiated BDF-R specimen are shown in Fig. 4.2. Experimental XRD patterns recorded from standard UO₂ fuel specimens (both fresh and irradiated ones) are qualitatively similar to those acquired from DF specimens (Fig. 4.2), and are, therefore, not shown. The XRD spectrum of the irradiated UO₂ presented here in Fig. 4.2 was measured using micro-focused X-rays in a single-point spot mode from a localized

region within the BDF-R specimen where the local burnup is estimated to be approximately 70 MWd/kgU. This burnup value has been determined by considering the location of the sampled point and taking the corresponding calculated value of local fuel burnup derived from the EPMA data (see Fig. 3.6).

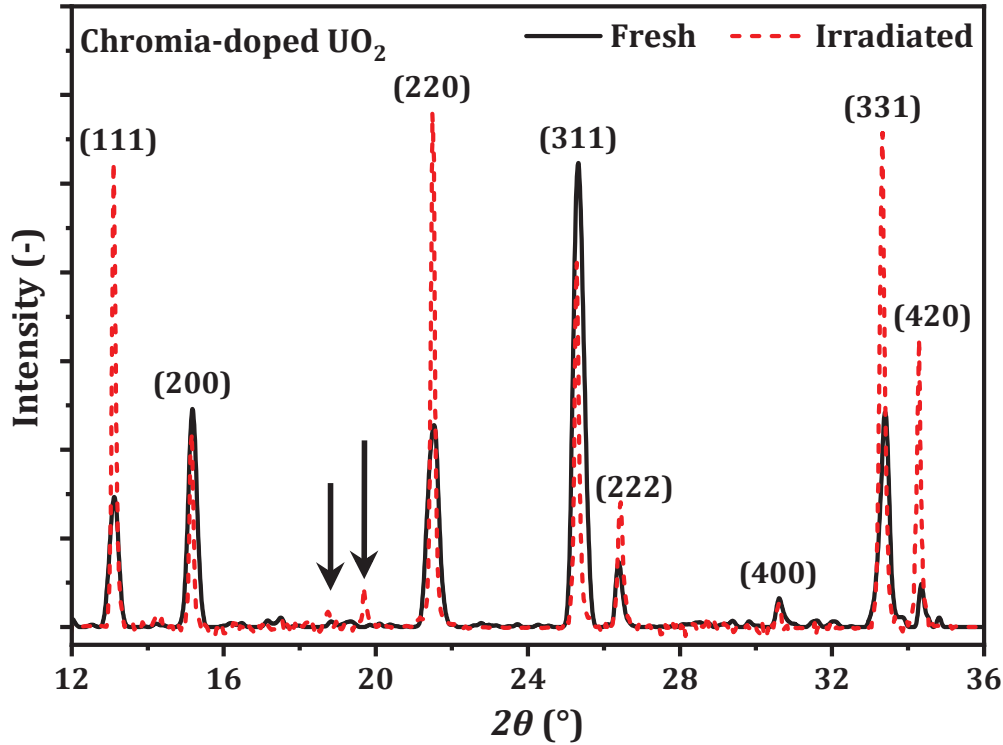


Figure 4.2: Comparison of the experimental XRD patterns for fresh and irradiated chromia-doped UO_2 fuels. The irradiated fuel has a local burnup of about 70 MWd/kgU.

As can be seen in the Fig. 4.2, the UO_2 specimens exhibit several Bragg peaks of $\{hkl\}$ reflections, and variation of diffracted peak intensities occurs over the complete diffraction pattern for each fuel specimen. There is also a change in the relative intensities of major diffraction peaks for fresh and irradiated DF specimens. This change in relative peak intensities is due to the effect of polycrystalline texture (*i.e.*, locally different orientations of UO_2 crystals illuminated by the synchrotron micro-spot beam) on the diffraction intensities that originate from the specimens. In Fig. 4.2, some additional tiny peaks (indicated by arrows in the figure) in the 2θ range 15° to 20° are clearly observed in the XRD pattern of irradiated BDF-R specimen, which may to some extent be ascribed to diffraction from fission products bearing oxides (or composites) in crystalline form present in the spent fuel specimen. A discussion of the more detailed aspects of the fission product phases is, however, outside the scope of this thesis.

In addition to the relative intensities change, shifts of XRD peaks towards lower 2θ angles and broadening of XRD line profiles are observed for all irradiated fuel specimens (of

both standard and chromia-doped UO_2) when compared with those of the corresponding unirradiated UO_2 samples. In Fig. 4.3, typical XRD peak profiles of the (331) reflection at different fuel burnup ranging from 64 to 90 MWd/kgU are displayed. These XRD data have been measured from the BDF-C and BDF-R specimens. The diffraction pattern of the (331) Bragg peak recorded from the non-irradiated reference FDF sample is also included in the figure. It may be noted in Fig. 4.3 that (331) peak intensities of the irradiated UO_2 are scaled to the same maximum intensity of the (331) peak measured from fresh fuel for comparison reason. When comparing the XRD data of fresh and irradiated specimens in Fig. 4.3, it becomes clear that XRD peaks of the (331) reflection for irradiated UO_2 are shifted towards the lower angles of the 2θ scale, and exhibit the shapes of significantly broadened diffraction profiles. The changes observed in the Bragg peak position as well as diffraction line broadening in the XRD pattern of irradiated fuels as compared with unirradiated ones are related to the distortion in UO_2 unit cell structure resulting from neutron irradiation, the residual strain/stress state in irradiated UO_2 crystallites and the population of radiation-induced defects in spent fuels.

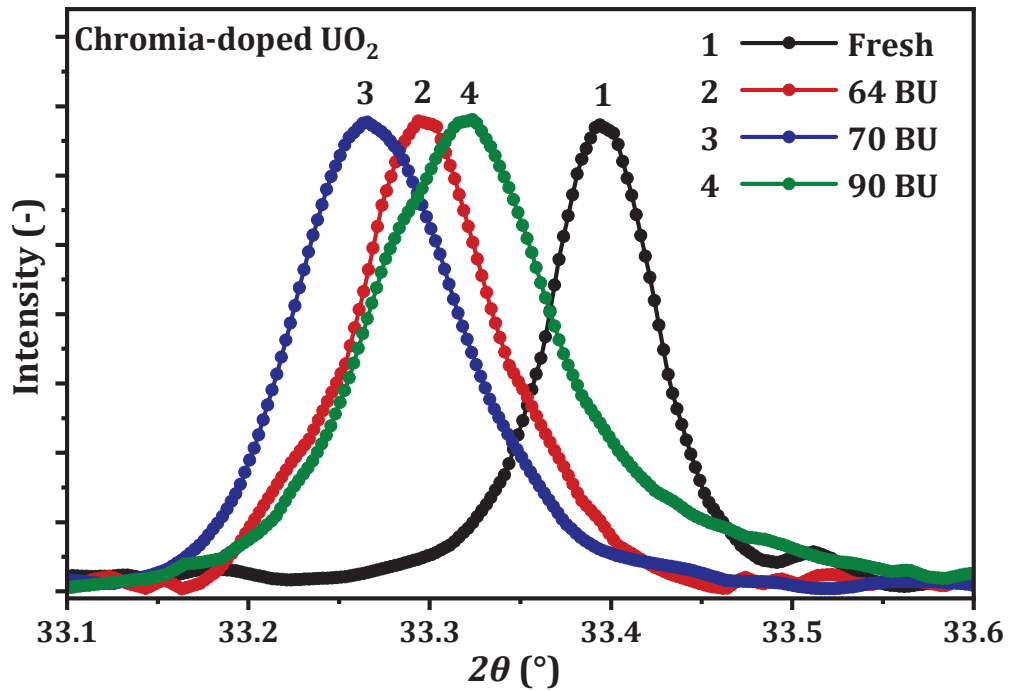


Figure 4.3: XRD reflections (331) of unirradiated and irradiated DF specimens having burnup in the range of 64 to 90 MWd/kgU.

The (331) XRD pattern of UO_2 fuels have been analyzed in terms of the change in centroid position of the Bragg angle, and the experimental value of UO_2 lattice constant has been calculated using Eq. (4.1) and Eq. (4.2). The variation of UO_2 lattice parameter with burnup for standard UO_2 and chromia-doped UO_2 spent fuels is shown in Fig. 4.4. One can observe that the dependency of lattice constant on burnup follows a similar trend in

these two different materials (*i.e.*, undoped and doped UO_2). Regardless, both materials show that at the first stage, the change in lattice parameter (Δa) increases with increasing fuel burnup reaching a maximum of about 0.35% (*i.e.*, relative lattice dimension change, $\Delta a/a$, in percent) at about 70 MWd/kgU, and then decreases in the burnup range between 75 and 100 MWd/kgU. The resultant residual lattice expansion in spent fuels with respect to unirradiated UO_2 , measured in our μXRD experiments with $\sim 0.03\%$ accuracy, is found to be about $11 \times 10^{-3} \text{ \AA}$ (approximately 0.20%, an average value) for both standard UO_2 and chromia-doped material.

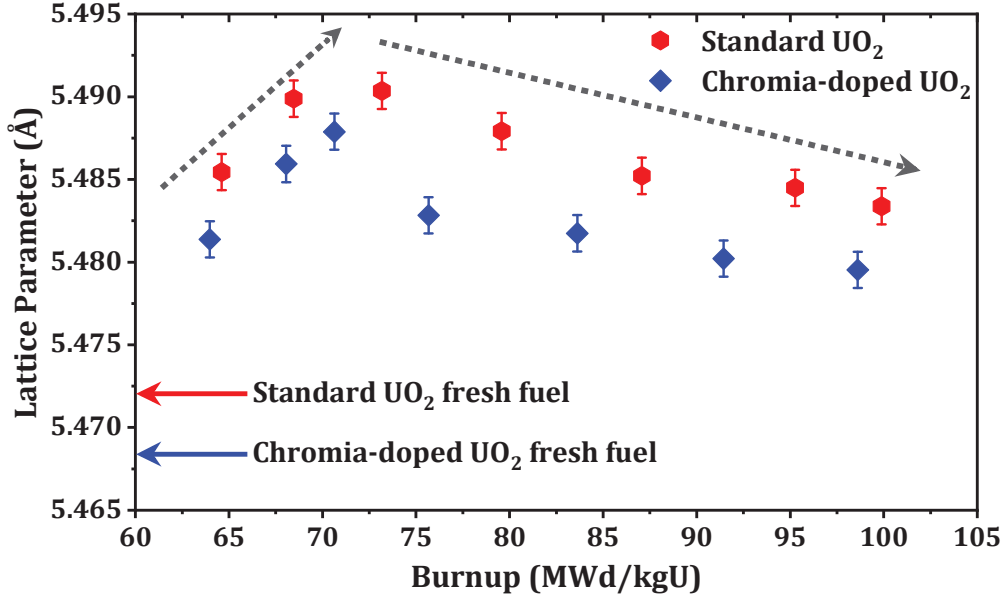


Figure 4.4: UO_2 lattice parameter evolution as a function of fuel burnup for standard UO_2 and chromia-doped UO_2 spent fuels. The data are shown by symbols and the long-dashed lines are drawn to guide the eye. The arrows indicate the lattice parameters for unirradiated standard and doped fuel, respectively. See text for details.

A comparison of our results and other studies shows that the overall trend for the lattice constant evolution with burnup, observed in Fig. 4.4, is in essential agreement with those of Szuta [104] and Spino and Papaioannou [105]. When this trend is compared with the results in Refs. [106,107], however, some difference in the burnup dependence of the lattice parameter can be noted, in particular, the onset of lattice contraction occurring at a threshold burnup below 70 MWd/kgU. The reason for this difference is unclear at present, but may be related to the effects of different irradiation conditions (linear heat rate, power density, neutron flux, power distribution in the reactor core, *etc.* [106]) of the examined materials.

As documented in the open literature for reactor-irradiated UO_2 [83,105-107], the microscopic origin of lattice expansion and contraction of irradiated fuels can be

considered to be due to the combined effect of soluble fission products incorporation, changes in local oxygen potential (*i.e.*, oxygen/uranium or O/M ratio) during irradiation leading to stoichiometry deviation (*i.e.*, hyper- and hypo-stoichiometric compositions, UO_{2±x}) of uranium dioxide, introduction of stable point defects and line defects in the Urania lattice submitted to neutron irradiation, and contribution of alpha-induced self-irradiation damage caused by Pu radionuclides during post-irradiation storage of fuel pellets.

Previous studies [108-110] have reported that oxygen non-stoichiometry (*i.e.*, O/M ratio) leads to a decrease of the lattice parameters for both hypo-stoichiometric UO_{2-x} and hyper-stoichiometric UO_{2+x} phases. For spent fuel produced under normal irradiation conditions, however, the local changes in average oxygen-to-metal ratios with local fuel burnups is expected to be negligible because of the reaction behavior of fission products Mo and Zr that act as oxygen getters to buffer the oxygen potential in the fuel during operation [105,111]. Therefore, the effect on UO₂ lattice constant due to its stoichiometry in spent fuels with a composition very close to the O/M ratio ~2.00 [111] can be neglected.

With regard to alpha-induced self-irradiation effects from alpha-emitters (*e.g.*, ²³⁸Pu) in nuclear fuels, previous studies [112-115] have found that alpha irradiation causes only a small increase of the UO₂ lattice constant, and is thus unlikely to significantly influence the UO₂ lattice parameter change [115]. Another factor that may have an influence on the lattice parameter determination is the increased porosity in the analyzed spent fuel pellets. However, in our study, the contribution of fuel porosities is assumed to be negligible because the effective values of the lattice parameter change due only to porous microstructure [9] are expected to be too small in magnitude (~10⁻⁴ Å) [116-118] in comparison to our observed Δa of about 11×10^{-3} Å for irradiated fuels. Since nuclear fuel undergoes a significant microstructural alteration upon prolonged irradiation and suffers chemical changes associated with the burnup level as well as temperature encountered in-pile, here we focus on selective fission products as well as actinide elements that can dissolve in the irradiated fuel matrix to be accommodated in the UO₂ lattices as soluble components at cationic trap sites, and likely to incur changes to the unit cell size of the crystal lattice at the atomic level.

4.3 Effect of dissolved fission products on UO₂ lattice

Spent nuclear fuel is a complex material in which FP elements are embedded in the UO₂ matrix. The inventory and complex distribution of FP components (compounds, aggregations, *etc.*) within a used pellet depend on the reactor operational parameters (power profile in the core and the resulting boundary conditions) as well as irradiation history, the temperature gradients in the fuel pins, and the final discharge burnup in the fuel assembly.

For LWR fuels, the principal properties of the stable FPs and minor actinides can be summarized as follows: Gaseous fission products (*e.g.*, Xe and Kr) are present as finely dispersed bubbles within UO₂ grains, and these gas bubbles can have different number and size distributions depending on the fuel burnup level. Metallic fission products (*e.g.*, Mo, Tc, Ru, Rh, Pd) are dispersed in the fuel matrix as micrometer- or nanometer-sized immiscible metallic particles. Other fission products (*e.g.*, Rb, Cs, Ba, Zr) may occur as oxide precipitates or in solid solution (*e.g.*, Sr, Zr, Nb, and lanthanides) within the UO₂ matrix. Trans-uranium elements (*e.g.*, Np, Am, *etc.*) are mostly in solid solution within the UO₂ matrix, whereas excess Pu may form some small Pu-rich islands depending on the local burnup level throughout the pellet. Volatile elements (*e.g.*, Cs, I) often migrate into grain boundaries and/or cracks within the fuel pellets, as well as into the gap between the pellet peripheral regions and the metal cladding. The degree of fuel oxidation as well as the formation of (U,Pu,FPs)O_{2±x} and/or (FPs)O_{2±x} phases, as a result of oxygen gettering by various radioelements, are naturally correlated with the ultimate fuel burnup. There exists a vast literature on the fission product topic and a list of selected references are [9,44,45,119-122], including those about the soluble fission product elements that are of prime interest in the present work.

Following previous works on (Pu,U)O₂ mixed oxide (MOX) fuel (originally contained 4.7 wt.% Pu and discharge burnup of 60 MWd/kgU) [84,123] and PWR spent fuel materials (both standard UO₂ and chromia-doped UO₂) irradiated to an intermediate burnup level (40 MWd/kgU pellet-average) [83,102], attempts have also been made in the present study to examine the lattice parameter changes of UO₂ due to fission products doping for higher burnup BWR spent fuel materials (69 MWd/kgU pellet-average). Such analysis, however, requires knowledge of solubility limits as well as quantitative solubility data sets for dissolvable FP oxides in uranium dioxide matrix.

Before performing the numerical analysis to predict changes of UO₂ lattice constants with soluble solutes, the EPMA results of the PIEs on BSF and BDF pellets were taken into account for understanding and possible interpretation of the μ XRD results. For calculating the lattice parameter, the average concentrations of some of the FP elements are taken from those results of EPMA analyses. The element concentration data of a few selective FPs, activation products and actinide isotopes that we did not measure by EPMA are taken from prior work [44,124-128]. In Table 4.1, the average values for the elemental concentrations of U, Pu and several FP elements, as obtained by EPMA line scans along the radial direction of the irradiated BDF pellet, are quoted. The values of the two major parameters (*i.e.*, ionic radii and charges of elements), considered in numerical analysis of lattice constant calculations, are also listed in Table 4.1. These ionic radii data have been collected from Shannon's table [129]. It is noteworthy to mention that corresponding EPMA results of the characterization of the BSF pellet are similar to that of the BDF pellet and are not reported here.

Table 4.1: Quantitative EPMA results of element concentrations obtained from the BDF pellet.

Elements analyzed	Ionic radius (Å), charge of elements	Center region (Average value) (wt.%)	Peripheral region (Maximum value) (wt.%)
U	1.00 (+4)	82	76
Pu	0.96 (+4)	0.92	2.50
Ru	0.62 (+4)	0.43	1.40
Tc	0.64 (+4)	0.15	0.48
Mo	0.65 (+4)	0.50	1.40
Nb	0.79 (+4)	0.008	0.015
Zr	0.84 (+4)	0.60	1.40
Nd	1.11 (+3)	0.75	1.36
Pr	1.13 (+3)	0.14	0.24
La	1.16 (+3)	0.24	0.45
Y	1.02 (+3)	0.06	0.09
Ba	1.42 (+2)	0.36	0.95
Pd	0.86 (+2)	0.12	1.16
Sr	1.26 (+2)	0.06	0.09
Cs	1.74 (+1)	0.47	1.20
Xe	–	0.26	0.63

The lattice parameter changes have been calculated using the proposed methods from the literature and obtained using the following empirical equation [130]:

$$a_{(UO_{2\pm x}, k)}^{doped} = a_{UO_2}^{nominal} + \sum_k (0.0206 \cdot \Delta r_k + 0.0013 \cdot \Delta z_k) m_k \quad (4.3)$$

where, $a_{UO_2}^{nominal}$ (5.468 Å for chromia-doped UO₂ and 5.472 Å for Cr-free standard UO₂ fresh fuels) and $a_{(UO_{2\pm x}, k)}^{doped}$ are the lattice constants of conventional UO₂ unit cell and the resulting oxide solid solutions of UO₂ with k^{th} dopant, respectively. The term Δr_k ($r_{dopant} - r_{host}$) represents the difference between the dopant ionic radius and the host cation U⁴⁺ radius, and Δz_k ($z_{dopant} - z_{host}$) is the corresponding valency difference with the charge number z . The notation m_k denotes mole percent of the added k^{th} dopant which again can be expressed as [130]:

$$m_k = \frac{n_k \cdot M_k}{100 + \sum_k (n_k - 1) M_k} \cdot 100 \quad (4.4)$$

where, n_k is the number of metal ions in the solute oxide and M_k is the mole percent of the k^{th} dopant oxide.

From a simple consideration of dissolvable FP oxides as well as other actinide oxides in the form of binary MO_x relevant to irradiated nuclear fuels, the calculations are performed from Eq. (4.3) through Eq. (4.4) with the use of the concentration data in

Table 4.1 and previously published solubility data with regard to FPs dissolution into the UO_2 lattice. Since there is a wide variation of local FPs concentration for all FPs in the outer peripheral region of the DF pellet, the changes of lattice parameter have been calculated considering the FPs concentration data (column 3 in Table 4.1) measured from the central part of the pellet (which corresponds to average local burnup $\sim 65 \text{ MWd/kgU}$) where these concentrations varied in a negligible range (see Fig. 3.6).

The cumulative effect caused by a number of foreign atoms dissolution in the UO_2 lattice of irradiated chromia-doped fuel is shown in Fig. 4.5. Similar results (not shown) were observed for the lattice parameter changes in irradiated standard (*i.e.*, undoped) fuel. Calculated lattice parameter changes are plotted in Fig. 4.5 by solid circles data points with a dotted line connecting them for visualization of these data, and the dashed line (in red color) is drawn for a trend indication. The variety of metal cations that are predicted to contribute to the lattice parameter change are also indicated in the figure.

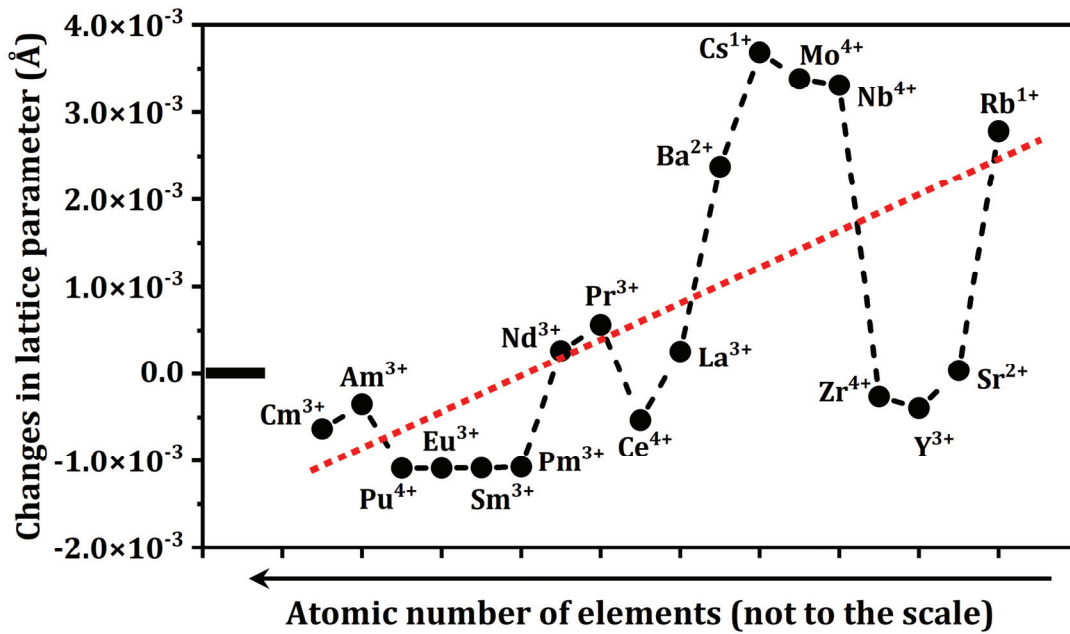


Figure 4.5: Changes in UO_2 unit cell lattice parameter due to various soluble additives with various valences analyzed for chromia-doped UO_2 spent fuel.

It can be noticed in Fig. 4.5 that the introduction of most common additives chosen for this study have only subtle effects on the parent UO_2 lattice, except for Ba, Cs and Rb, which have a tendency to increase the lattice parameter up to some extent. The reason for this is that these dopants have a much larger ionic radius, namely, Ba^{2+} (1.42 Å), Cs^+ (1.74 Å) and Rb^+ (1.61 Å), in comparison to the host U^{4+} ion (1.00 Å), which moderately influence the calculated values of the effective changes in lattice parameters with the consideration (of r_k term) that apply to Eq. 4.3. It is also important to note that in the present study the contents in soluble form of Ba, Cs and Rb in irradiated UO_2

matrix are considered to be very low, in the concentration range 0.06-0.20 wt.%, which are in line with those results published in previous studies [44,124,126,131,132]. Nevertheless, the overall result presented in Fig. 4.5 indicates that dissolved FPs, activation product and other actinide isotopes furnish a very small contribution to changes in the UO₂ lattice constant, the values are in the range of $\sim 1-3 \times 10^{-3}$ Å. From these data, the average cumulated enlargement due to foreign atoms dissolution is estimated to be about 4×10^{-3} Å. This value, however, is significantly lower than the lattice expansion value of $\sim 11 \times 10^{-3}$ Å (Fig. 4.4) obtained from XRD analysis for both the standard and chromia-doped spent fuel samples.

Therefore, the significant differences observed between the experimental result and theoretical estimation of UO₂ lattice parameter changes imply that the fission products incorporation effects alone cannot explain the overall lattice expansion as measured for the irradiated UO₂ crystallites. The change in the lattice dimension can also be related to the crystalline defects formed, such as, point defect complexes and occurrence of local dislocation pile-up. Thus, the current finding signifies that defects due to radiation damage dominate in irradiated UO₂ crystallites, as has also been described previously [105,133,134]. It is to be noted that both Cr-free and Cr-doped fuel materials are found to behave in a similar manner (at a given burnup) with UO₂ lattice expansion occurring upon irradiation where any Cr (*i.e.*, the dopant) induced effect seems insignificant [83].

4.4 Summary

This chapter reports an experimental investigation on the irradiation-induced microstructure evolution in high burnup chromia-doped UO₂ spent fuel considering the role of Cr as dopant and chemical effects of fission product elements, as compared to the standard UO₂ material (*i.e.*, conventional, undoped nuclear fuel). A synchrotron based modern analytical method of scanning micro-beam X-ray Laue diffraction is used to probe the fuel specimens prepared by replica printing technique from reactor exposed UO₂ pellets. To obtain spatially resolved structural information, spatially resolved μ XRF and μ XRD measurements have been made on small sub-samples, covering a wide range of local burnup from about 64 to 100 MWd/kgU. The local burnups of the fuel in the analyzed specimens have been determined using the retained local concentrations of the fission product Nd as measured by EPMA.

The diffraction line profiles of characteristic (331) Bragg reflections are analyzed in detail for a quantitative evaluation of UO₂ lattice parameter with fuel burnup. It is observed that the dependency of lattice constant on burnup for undoped and doped UO₂ follow a similar trend. The resultant residual lattice expansion in spent fuels with respect to unirradiated UO₂ is found to be about 11×10^{-3} Å for both standard and chromia-doped UO₂. Numerical analyses to predict changes of UO₂ lattice constants indicate that components of lattice parameter evolution due to soluble fission product solutes as well as other actinides isotopes furnish a very small contribution to lattice expansion (average

cumulated enlargement $\sim 4 \times 10^{-3} \text{ \AA}$). The fission products incorporation effects alone cannot explain the overall lattice expansion as measured, and the crystalline defects formed, such as, stable point defects complexes and occurrence of localized dislocation pile-up dominate in irradiated UO₂ crystallites.

5 Residual Lattice Strain in UO_2

Understanding the strain/stress state exhibited by irradiated UO_2 fuels is of great importance for assessing the UO_2 behavior during different stages of irradiation and extending the burnup of operating fuel in LWRs. Specifically, the response of fuel pins in-pile under over-power transient conditions accompanied by a marked temperature rise in the fuel, which can lead to a sudden stress release from pellets to cause fine fragmentation of the fuel material. This chapter of the thesis reports a quantitative evaluation of the changes in the UO_2 crystallinity and residual strain present in irradiated UO_2 spent fuel materials. The specimens investigated are commercial grade standard UO_2 and chromia-doped UO_2 materials (BSF and BDF), irradiated with an average pellet burnup of about 68 MWd/kgU. High spatial resolution micro-beam XRD mapping measurements have been performed at the microXAS beamline of the PSI-SLS facility. The obtained XRD data have been analyzed using the XRDUA software in a batch-wise processing mode. The lattice-strain distribution results reported here can be of great importance to model resulting changes as well as microstructural evolution that occur in operating UO_2 fuels when irradiated under LWR conditions.

5.1 Scanning XRD data processing

Scanning μXRD provides an option to analyze subtle changes in the dimension of the unit cell of crystalline materials, and offers to monitor changes on very small length scales. By analyzing the scanning microscopic μXRD data in a batch-wise processing mode, the local residual strain in the irradiated UO_2 crystallites was evaluated. The analysis was carried out using open-source XRDUA data reduction package.

In the first processing step, a single Laue diffraction image has been selected from a scanned μXRD area map of spent fuel particles. Thereafter, the single-spot 2D- μXRD image has been analyzed in detail using peak fitting routines to determine $2\theta_{hkl}$ peak positions as well as number of fit parameters (for different Bragg peaks of $\{hkl\}$ reflections) as input information required for batch process data analyses. Once the XRD quantitative analysis for a single μXRD CCD image is completed, a set of 2D- μXRD maps (for various $\{hkl\}$ reflections) has been generated by performing a batch processing of whole μXRD mapping data sets (details about the batch processing using XRDUA software is given in Appendix A). The same data processing protocol was followed for different $\{hkl\}$ diffraction peaks. The final data sets extracted in a table-matrix form

contain $2\theta_{hkl}$ values (peak centroid positions) of a given $\{hkl\}$ reflection, as well as the row and column indices associated to the measured $2\theta_{hkl}$ data obtained from each sampling point (*i.e.*, each pixel) in the spatial domain. The last step involves quantitative determination of lattice strain as well as conventional numerical analyses of the batch-processed scanning μ XRD data set expressed in the format of a matrix for the construction of corresponding strain distribution maps using a series of in-house MATLAB scripts.

From a matrix containing the diffraction angle $2\theta_{hkl}$ values, the interplanar d -spacing, d_{hkl} , matrix has been constructed by applying Bragg's formula (Eq. 4.1). Consequently, the percentage strain value for each element of the d -spacing matrix has been calculated using the following relationship:

$$Strain (\%) = \frac{d - d_0}{d_0} \times 100 \quad (5.1)$$

where, d_0 represents the interplanar distance in a strain-free UO₂ lattice. The interplanar distances of different $\{hkl\}$ reflections for the fresh fuel UO₂ samples, d_0 , have been determined using Eq. 4.2 and utilizing the measured lattice parameter values ($a = 5.472$ Å for standard UO₂ and $a = 5.468$ Å for Cr-doped UO₂). The resulting numerical data sets in the strain distribution maps were further processed by using additional MATLAB-based tools to better represent the local detail in the intensity distribution of the strain maps produced.

It is yet worth to mention that although lattice strain can be measured for all $\{hkl\}$ peaks of interest, problems were sometimes encountered with the batch-mode data processing method (given in Appendix A) to model diffraction line profiles of all higher order $\{hkl\}$ reflections. This was probably, in part, because of the microscale spatial variation in the shape and orientation of the UO₂ grains in the spent fuel matrix as well as texture characteristics of irradiated UO₂ crystallites, which resulted in large intensity variations for some of the high index $\{hkl\}$ diffraction peaks aroused from different sampling points within the illuminated sampling area in the scanning μ XRD measurements. In other words, for instance, presence of important but weak-intensity diffraction spots (recorded in the CCD) in some μ XRD frames of a raster-scanned μ XRD image series may make it difficult to perform quantitative batch mode analyses of whole datasets. Therefore, the raw XRD CCD images were visually inspected and small regions were selected for the construction of 2D strain maps in the investigated specimens.

5.2 Microscale lattice strain distribution

The following section presents a comparative analysis of the local (microscale) lattice strain distributions in standard UO₂ and chromia-doped UO₂ spent fuel materials. This analysis is based on using the BSF-C and BDF-C specimens, and the obtained strain

maps for these reactor-irradiated fuels are associated with the (311) crystal planes of the UO_2 fluorite lattice. From the large area μXRF overview maps, a region-of-interest in each specimen was selected where the estimated mean local burnups of the spent fuels were about 68 MWd/kgU (see Figs. 3.5 and 3.6). And then, the scanning μXRD data sets were analyzed over a rectangular area of $50\text{ }\mu\text{m} \times 40\text{ }\mu\text{m}$ (comprising 500 μXRD CCD-frame Laue images) of the BSF-C specimen, and in a similar way, on a $30\text{ }\mu\text{m} \times 30\text{ }\mu\text{m}$ square area (comprising 225 μXRD CCD-frame Laue images) of the BDF-C specimen.

The experimental results obtained by combining μXRF and μXRD analyses of BSF-C and BDF-C specimens, that are irradiated to a burnup of about 68 MWd/kgU, are summarized in the overview maps shown in Figs. 5.1 and 5.2. All plots in Figs. 5.1 and 5.2 are displayed as RGB color images. In the μXRF images, presented in Fig. 5.1(a) and Fig. 5.2(a) for undoped and doped UO_2 , respectively, the size of each square-pixel cell is $2\text{ }\mu\text{m} \times 2\text{ }\mu\text{m}$, and the pixel coordinates in the raster μXRF maps are spatially correlated to the sampling locations on the fuel specimens at the sample stage. One may note a slight spatial variation (in micrometer scale) in the net intensity of the U $\text{L}\alpha$ signal in some regions on the μXRF maps, which is the effect of local thickness variation in the analyzed spent fuel particles. The two respective strain mapping images, constructed from scanning μXRD data set, are shown in Figs. 5.1(b) and 5.2(b). To better visualize the spatially resolved lattice strain distributions in the strain maps, the mapping data are shown at different scales.

In each strain map, the magnitudes of local tensile strain within the 2D sampling frame are decoded into different shades of RGB colors, which is especially relevant for easy data visualization purposes. An observation of the strain maps in Figs. 5.1(b) and 5.2(b) reveals the presence of microscale strain inhomogeneities, and that the tensile strain non-uniformly varies in both the lateral and vertical directions. The results of the standard UO_2 material in Fig. 5.1(b) shows that the strain values in irradiated UO_2 crystallites lie roughly between 0.1% and 0.3%. The residual lattice strain values in the Cr-doped UO_2 material (in Fig. 5.2(b)) range from 0.1% to 0.4%. With regard to strain quantities reported here, any contribution of subtle strain results falling below 0.1% limit have been ignored due to experimental constraints in studying highly radioactive nuclear fuel using scanning μXRD , and achievable angular resolution limit of our micro-beam Laue diffraction experimental setup.

A comparison of these measures of UO_2 lattice strain in 68 MWd/kgU (pellet average BU, equivalent to $\sim 7.1\%$ FIMA) burnup spent fuel materials shows that the strain distributions are nearly similar in the chosen mapping regions for both specimens, namely standard UO_2 and Cr_2O_3 -doped UO_2 fuels, with the maximum residual lattice strains of 0.3% and 0.4%, respectively. The importance of these strain quantities with respect to each other is self-evident, as results obtained for similar irradiation conditions are similar, regardless of fuel (material) type.

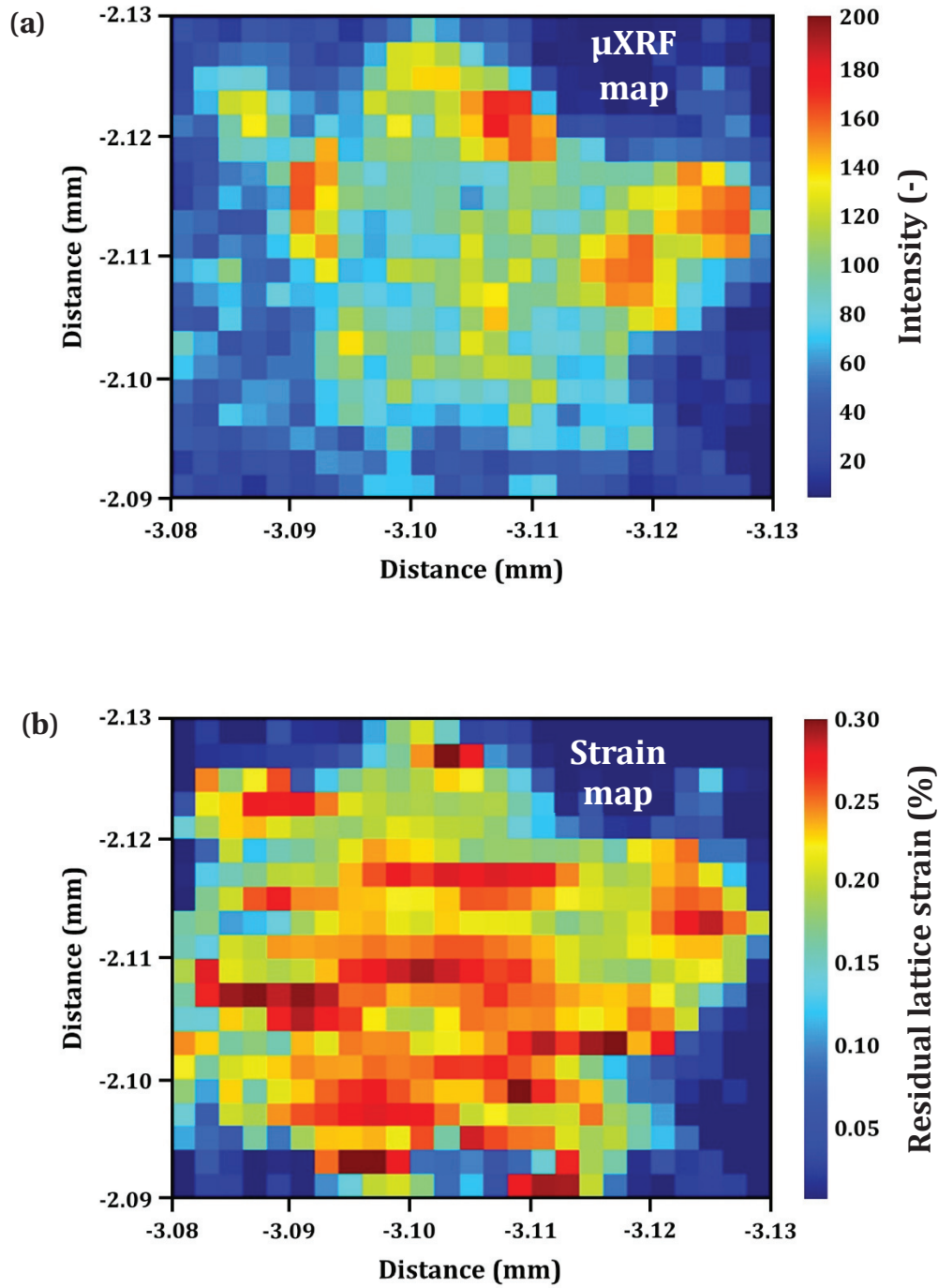


Figure 5.1: (a) The μXRF element mapping (2 μm step size, 2 s exposure) with the U L α fluorescent line of the area under investigation for identifying spent fuel UO_2 particles (local burnup ~ 68 MWd/kgU) on the Kapton tape, shown for BSF-C sample. (b) The corresponding lattice strain distribution map of irradiated UO_2 crystallites for the entire mapped area, obtained by analyzing the scanning μXRD data set in a batch-wise processing mode. See text for details.

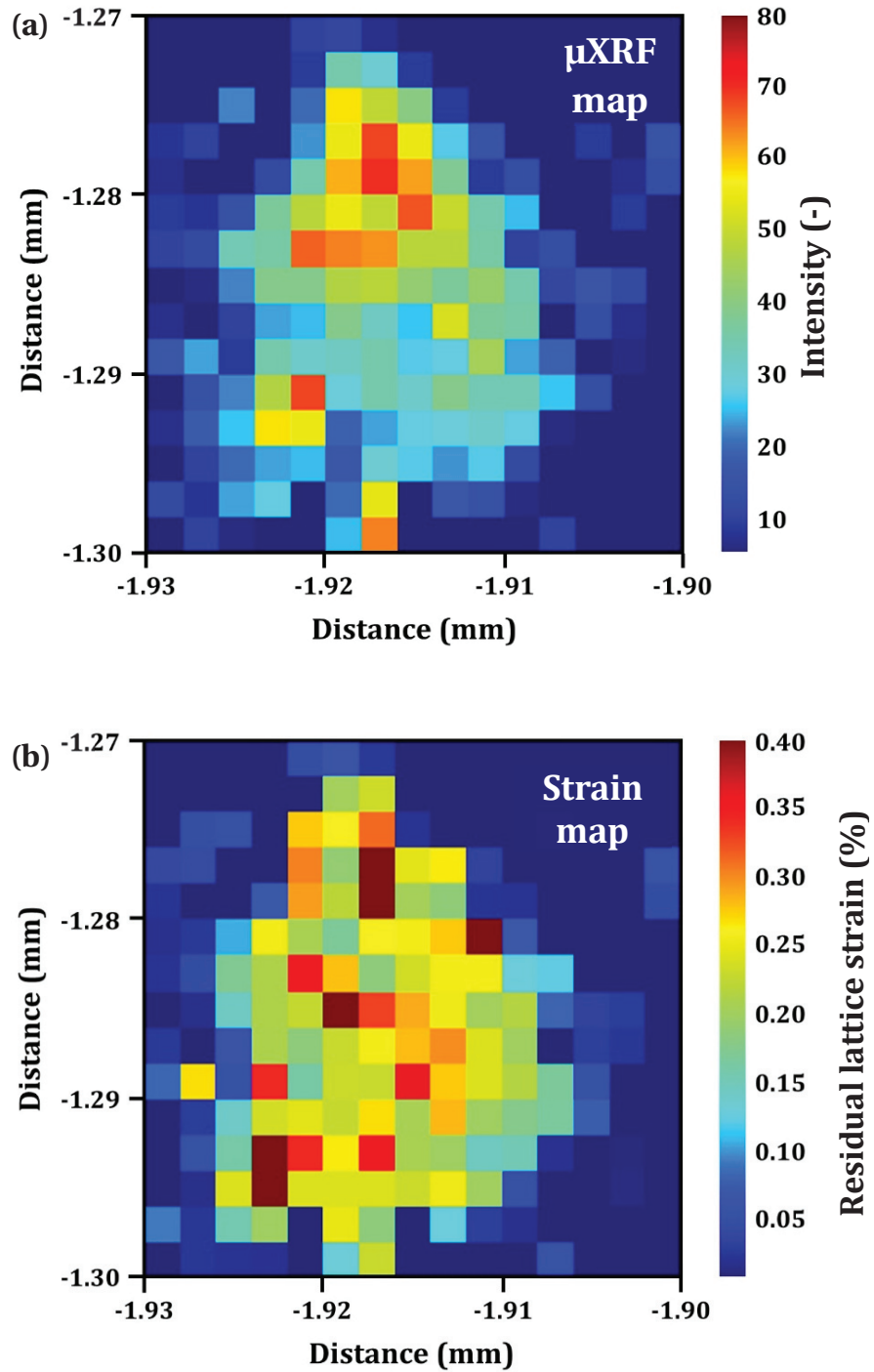


Figure 5.2: (a) The μ XRF element mapping (2 μ m step size, 2 s exposure) with the U L α fluorescent line of the area under investigation for identifying spent fuel UO₂ particles (local burnup \sim 68 MWd/kgU) on the Kapton tape, shown for BDF-C sample. (b) The corresponding lattice strain distribution map of irradiated UO₂ crystallites for the entire mapped area, obtained by analyzing the scanning μ XRD data set in a batch-wise processing mode. See text for details.

In order to compare strains calculated from our data with literature results, we have not come across any published article to date that investigated irradiation-induced residual lattice strain evolution at the microscale in reactor exposed nuclear fuel UO_2 material. Most of the available literature, on both elastic strain buildup accompanied by internal stress development and plastic deformation generation in irradiated UO_2 crystals, refer only to ion implanted samples [135-139]. There are few other studies [106,107,140] on LWR spent fuels by laboratory-based XRD where local burnup dependence of strain energy density due to the accumulation of dislocations has been reported. Within this context, synchrotron radiation-based micro-Laue technique has also been used, and the accumulated strain energies were determined from μ -Laue diffraction data obtained from intermediate burnup (~ 30 MWd/kgU) chromia-doped UO_2 fuel particles [83]. The results in Ref. [83] helped in understanding the first steps of UO_2 polygonization observed even at that burnup level. The development of lattice strain in UO_2 crystals after irradiation is directly associated with the presence of different types of crystal defects, the most important of which is dislocations [141,142]. Another component is the FPs induced strain associated with pressurized fission gas bubble population and solid fission product bearing inclusions in irradiated fuels [143]. In relation to the microscopic strain development in irradiated UO_2 , it is an important performance parameter for its influence on the overall macroscopic stability of the spent fuel pellet, confinement of the FPs in the fuel matrix, fuel swelling and in-pile creep behavior of UO_2 during reactor operations.

5.3 Summary

By combining μ XRF imaging experiments and extracted crystallographic information based on the obtained μ XRD results, microscale maps of local residual strain in irradiated UO_2 crystal lattices have been constructed to determine the spatial variability of strain characteristics inside the spent fuel materials. Samples of both Cr-free standard UO_2 and Cr-doped UO_2 fuels, irradiated to a burnup of 68 MWd/kgU, have been selected and investigated. At this microscale, the UO_2 lattice strain exhibits heterogeneity, though the distribution of strain in the chosen mapping region is nearly similar for both specimens. The results of the standard UO_2 material shows that the strain values in irradiated UO_2 crystallites lie roughly between 0.1% and 0.3%. The residual lattice strain values in the Cr-doped UO_2 material range from 0.1% to 0.4%. The lattice-strain development in irradiated UO_2 crystals causing local lattice distortion for 68 MWd/kgU burnup fuels is attributable to dissolution of solid FPs in the uranium dioxide lattice, precipitation of insoluble FPs, formation of over-pressurized fission gas bubbles and irradiation damage accumulation in the fuel matrix.

6 Dislocation Content in UO₂ Fuel

Many studies [6,9,16,144,145] have shown that the evolution of microstructural features in UO₂ fuel under irradiation, at relevant operating temperatures and different fuel burnup levels, is apparently the combined effect of the damage accumulation in various forms of point defect clusters and extended defects, nucleation and growth of fission gas bubbles, incorporation of soluble FPs in the host UO₂ lattice and formation of solid intermetallic composites out of insoluble FPs in the fuel matrix, movement and spatial rearrangement of extended defects such as dislocations, subdivision of initial grains into sub-grains, and finally, irradiation-induced recrystallization in polycrystalline UO₂. Above a certain local burnup threshold, the so-called HBS forms, which can be mainly characterized as a mixture of fragmented UO₂ grains and newly formed recrystallized grains, and fission gas bubbles distributed among (sub)grains in the irradiated fuel matrix. With regard to damaging effects, dislocations in irradiated UO₂ fuel play an important role on the formation of sub-grains by rearranging themselves into their lowest energy configurations that lead to a reduction in stored strain energy per unit length of dislocation and lower the overall strain energy.

To unambiguously reveal the general trends associated with dislocations formed under irradiation in the UO₂ fuels investigated, in this chapter, the first characterization of dislocation distributions by micro-beam Laue diffraction analyses of high burnup chromia-doped UO₂ materials are reported. In the literature, there exist limited information and experimental data regarding the dislocation structures and quantity of dislocation densities in reactor-irradiated regular UO₂ fuel [8,99,141,142,144,146] analyzed by TEM. However, there are so far no similar studies performed on high burnup chromia-doped fuels. Though TEM is a very good analytical method to evaluate various crystal defects, such as dislocations, it is often a challenge to prepare ultra-thin TEM foils of high burnup nuclear fuel materials, normally characterized by high brittleness. Another limitation is the very small volume probed in TEM analysis, which makes the process quite time-consuming as several examinations of the sampling area are needed to obtain any quantitative results to be statistically representative of the sample analyzed. In this respect, the use of synchrotron based XRD technique is of great interest as it examines a higher volume fraction of the sample compared with that probed by TEM. The application of micro-beam Laue XRD method to analyze dislocation density and dislocation structure arrangements in damaged materials is well documented in the current literature [85,147-151].

6.1 Quantification of dislocation density

6.1.1 Cahn-Nye formalism

By utilizing XRD data obtained by Laue method, modifications of Laue spots shape (and, in particular, the transverse broadening in streaky Laue spots) arising from deformed crystals are commonly analyzed, which can then be interpreted in terms of quantitative values of geometrically necessary dislocation (GND) densities that develop during the plastic deformation phase in the materials to maintain crystallographic lattice compatibility and give rise to lattice bending. To date, many articles have been published on synchrotron radiation based μ XRD studies investigating GND development during plastic deformation in various structural materials [150-153].

In essence, the angular orientation spreads in streaked Laue spots along the azimuthal direction is a consequence of the local angular bending of the crystal, and the radius of lattice curvature, R , and can be calculated using the following relation [154]:

$$R = \frac{\delta}{[2 \sin(\psi/2)]} \quad (6.1)$$

where, ψ represents the average value (in degree) of the transverse broadening of indexed Laue peaks in a recorded Laue diffractogram. The δ term in Eq. 6.1 represents the spot size of the incident X-ray beam. For the quantification of the GND content, the Cahn-Nye equation [155] has been used, which allows for determining the GND density, ρ_{GND} , from the following relation:

$$\rho_{GND} \approx \frac{1}{(Rb)} \quad (6.2)$$

where, R (as in Eq. 6.1) denotes the radius of curvature of the crystal bending, and b is the Burgers vector value [equal here to $(a/2) \cdot \sqrt{2}$; a is the UO₂ lattice parameter, see Fig. 4.4] corresponding to GNDs. The mathematical formulation of Nye's dislocation density tensor, GND density calculations due to plastic deformation of polycrystalline materials, and the experimental quantification of the GND content that exhibits a length scale dependence associated with net dislocation content have been reported previously [156-161], and need no further elaboration here.

6.1.2 GND density evolution with burnup

Dislocations are experimentally characterized by their geometry, size, Burgers vectors, the operative slip planes in the crystal's matrix, and crystal orientations caused by the dislocations. In the case of fluorite-type oxide materials, dislocations can glide on {100}, {110} or {111} planes, and the three main dislocation slip modes of UO₂ described in the literature are $\frac{1}{2}\langle 110 \rangle \{100\}$, $\frac{1}{2}\langle 110 \rangle \{110\}$ and $\frac{1}{2}\langle 110 \rangle \{111\}$ with $\frac{1}{2}\langle 110 \rangle$ Burgers

vector [162]. Besides, it is also known that the activation of these slip systems strongly depends on both temperature and stoichiometry of UO_2 . In the lower temperature regime (< 800 K), the easiest glide system is $\frac{1}{2}\langle 110 \rangle \{100\}$ followed by $\frac{1}{2}\langle 110 \rangle \{110\}$ at elevated temperatures (≥ 1000 K) where both slip systems become active [163-166]. These temperatures fall within the range of operating temperatures for LWR fuel pins and the pellet temperatures experienced by the fuel. From these discussions, it is clear that local dislocation rearrangements, and then, the development of dislocation density as a function of local burnup in UO_2 fuel evolve on the most active $\frac{1}{2}\langle 110 \rangle \{100\}$ and $\frac{1}{2}\langle 110 \rangle \{110\}$ slip systems, though some cross-slip events involving $\{111\}$ glide planes have also been observed [164,167].

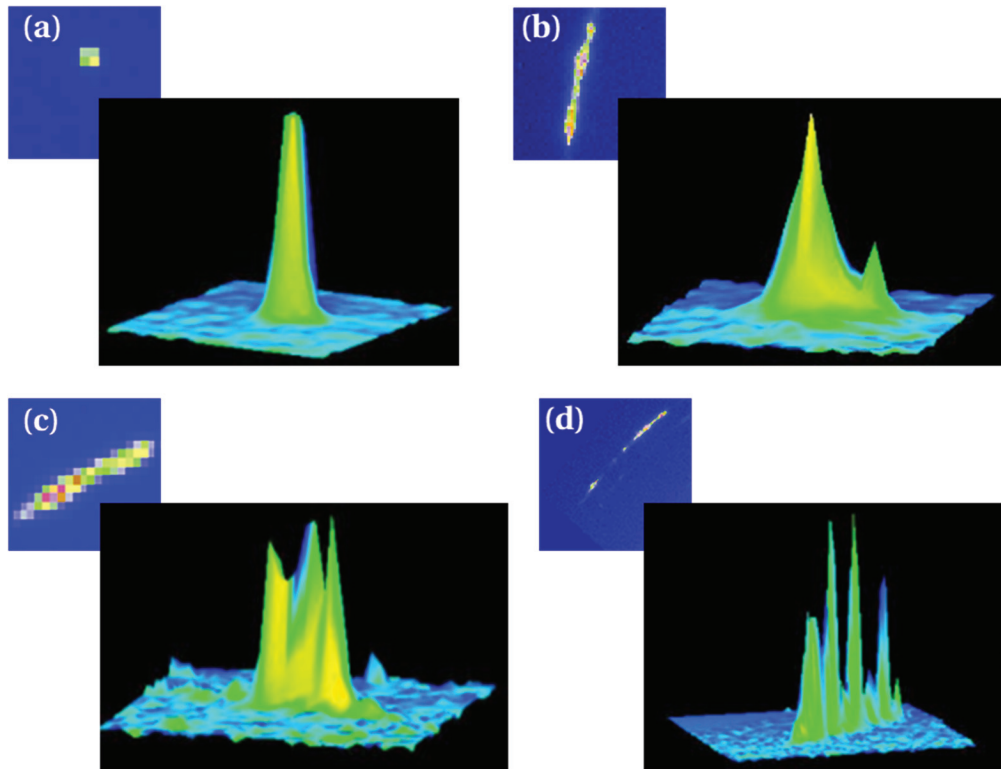


Figure 6.1: (a) Singular circular Laue spot observed in fresh non-irradiated fuels. In irradiated fuels, modifications are observed in the Laue spot in the form of (b) uniform streaking, (c) non-uniform streaking, and (d) splitting. The peak heights correspond with the intensity.

Referring to our scanning micro-beam XRD experiment on spent fuels, transverse broadening of Laue spots with fully elongated streaks has been observed for all $\{hkl\}$ reflecting planes obtained in the 2θ range of $12\text{--}36^\circ$ (see Fig. 4.2). For our purpose, here, the diffraction spots of the (220) reflex have been analyzed as it is one of the active slip planes responsible for the generation of the dislocations. It is also of some interest to mention that in our spatially resolved scanning μXRD experiments with high burnup spent fuels, complex Laue patterns exhibiting strongly blurred diffraction peaks,

non-uniform streaking and even pronounced splitting in spots (indicating subdivision of mother UO₂ grains, also known as fuel polygonization [84]) are also seen in some recorded Laue diffractograms, which is shown in Fig. 6.1. All these characteristic features of diffraction spots evidence the presence of several types of defects in irradiated UO₂ polycrystals and severe irradiation damage accumulation locally leading to microscale structural heterogeneities in the irradiated fuel matrix. In the present study, those Laue images with split reflections were not identified that arose from polygonised UO₂ grains because it is not the focus of this work.

As mentioned above, only the (220) Laue peak streaking observed on the Laue diffractograms have been investigated, and selected sets of single-shot Laue diffraction images (chosen data sets from the whole μ XRD mapping data sets) of BSF-C, BSF-R, BDF-C and BDF-R specimens have been analyzed. Those Laue images were carefully selected on the basis of visual inspection of (220) Laue spots distortion, and only those (220) Bragg reflexes have been considered which are long and display a rod-like elongated streak with uniform intensity distributions within the streaks. The GND density is then calculated using the expressions for R and ρ_{GND} given by Eq. 6.1 and Eq. 6.2, respectively.

Figures 6.2 and 6.3 summarize μ XRD results of GND density evolution with burnup for standard UO₂ and chromia-doped UO₂ fuels. Figure 6.2 shows the evolution of the (220) Laue diffraction spots with burnup, observed in the BDF-C and BDF-R specimens. A raw Laue diffraction image of the FDF specimen is also included in the figure. In each of the 2D images, only the magnified view of the region of interest from the original μ XRD CCD-frame is shown, and the procedure for determining the local effective burnup value (written in the Fig. 6.2) at multiple sampling locations is exactly the same as described in Chapter 3. It is easily seen that the (220) UO₂ Laue spot of the unirradiated fuel exhibits a well-defined and symmetric peak shape as appeared on the 2D CCD area-detector. It is also clear that the Laue spot of the (220) reflex becomes elongated (streaked) for irradiated UO₂, and the streak length of the Laue spots increases with burnup. Laue images belonging to the standard UO₂ spent fuel (BSF-C and BSF-R specimens) displayed characteristic features of Laue diffraction patterns, such as spots broadening (streaking) in the transverse direction, similar to those found in chromia-doped spent fuel, and are, therefore, not shown.

The 2D images shown in Fig. 6.2 were azimuthally integrated to obtain the average intensity distribution profiles over a specified range of azimuthal angle of the (220) reflection spots. The angular width ($\Delta\psi$) of the azimuthal intensity distribution curve were measured, also representing the FWHM (full width at half maximum) of the streaked peak in the unit of azimuthal angle, for each diffraction spot in the recorded Laue patterns shown in Fig. 6.2. The measured FWHM for fresh fuel (both standard and doped UO₂) is about $0.82 \pm 0.07^\circ$, the error involved is the angular resolution determined by the pixel size in the CCD and the standard deviation of the fitted curve.

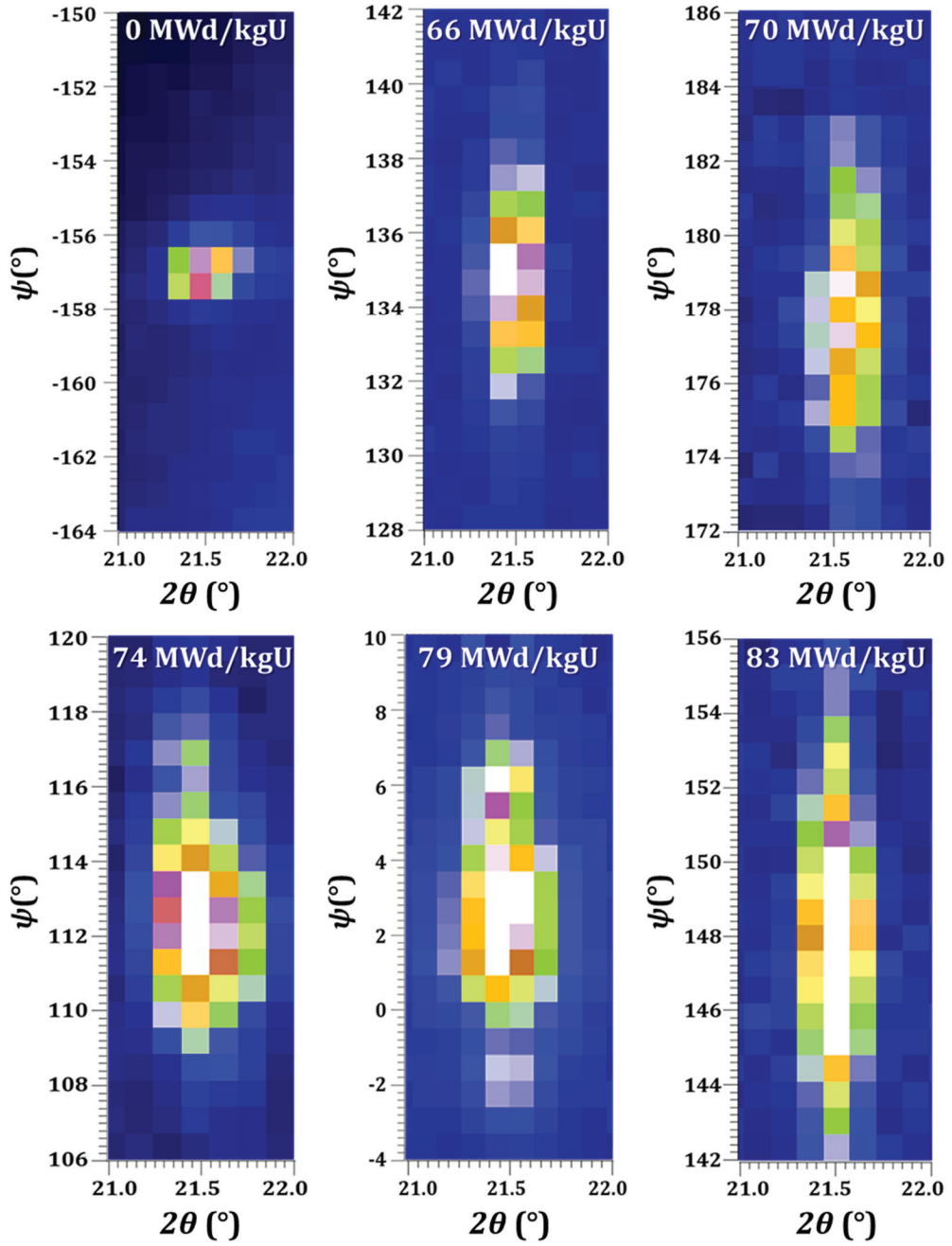


Figure 6.2: Two-dimensional Laue images showing the typical shapes of the (220) Laue diffraction spots observed from chromia-doped fresh fuel and irradiated specimens at various burnups.

For the irradiated chromia-doped UO_2 materials at different burnups in the range of 66 to 83 MWd/kgU, the $\Delta\psi$ values lie in the range of $6.81\text{--}12.54 \pm 0.21^\circ$ (see Fig. 6.2). A similar trend has been observed for the spent UO_2 standard fuel. The $\Delta\psi$ values of (220) Bragg reflexes are determined by analyzing the two mentioned specimens and are found to be in the range of $6.62 \pm 0.14^\circ$ to $11.58 \pm 0.19^\circ$ that cover fuel burnups of 65 to 84 MWd/kgU in the investigated materials. From these streak data, the GND content for

both undoped and Cr-doped fuels at five different burnup levels between 65 and 84 MWd/kgU has been calculated.

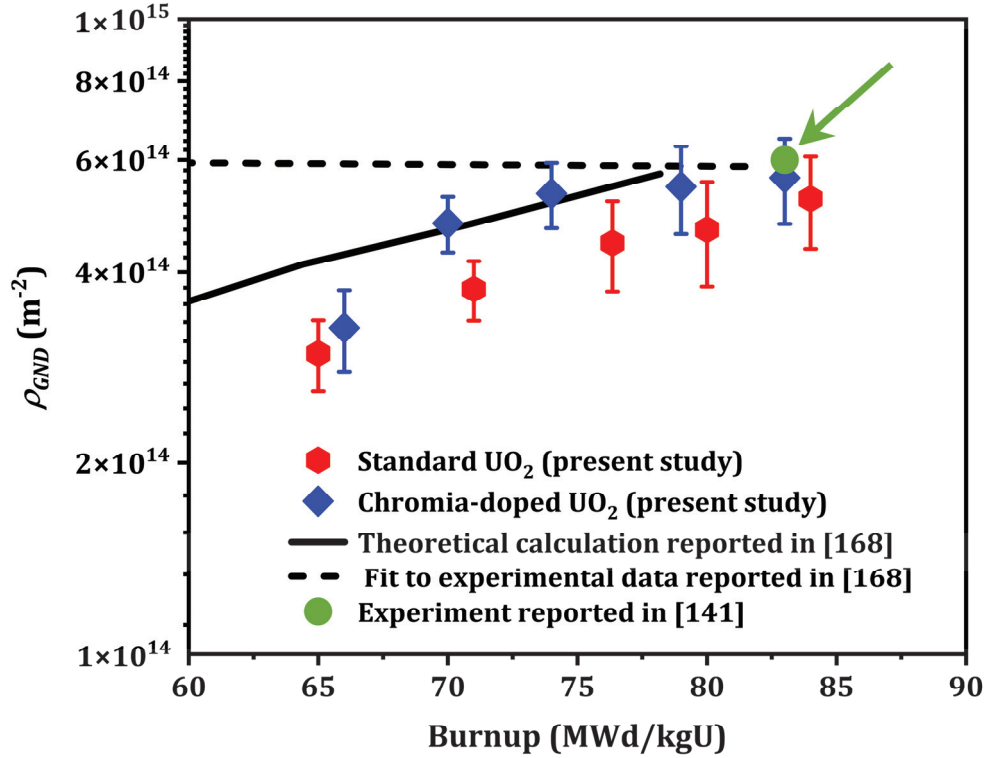


Figure 6.3: GND density versus burnup for standard UO_2 and chromia-doped UO_2 nuclear fuels.

The GND density evolution with burnup in standard UO_2 and Cr-doped UO_2 nuclear fuels is shown in Fig. 6.3. The corresponding numerical data of GND density is provided in Table 6.1. The red and blue symbols in Fig. 6.3 represent experimental results, and the typical error bars for the displayed experimental points are also indicated. Here, it may be mentioned that an estimate of the overall uncertainty is not simple in practice in determining the GND density by accounting all possible sources of experimental uncertainties (*e.g.*, displacement error of microscale samples, effect of incident beam-spot displacement, statistical uncertainties due to the small areas sampled during XRD scans, *etc.*) and the uncertainty caused by error propagation from input parameters of the mathematical models [Eq. (6.1) and Eq. (6.2)]. The error bar associated with each data point in Fig. 6.3 has been generated by taking the corresponding standard deviation derived from fitting azimuthal intensity profile of the (220) reflex. The results from TEM experiments on irradiated UO_2 and theoretical calculations of dislocation density evolution with burnup presented in the literature [141,168] are also included in Fig. 6.3 (black solid line, black dashed line and green symbol) for comparison. As a general trend, the GND density in both undoped and doped UO_2 materials is found to gradually

increase with increasing burnup from 65 to 75 MWd/kgU, and appears to become saturated above 75 MWd/kgU.

Table 6.1: Measured GND densities of standard and chromia-doped UO₂ fuels as a function of burnup.

Fuel type	Local burnup (MWd/kgU)	$\rho_{GND} \text{ (m}^{-2}\text{)}$
Standard UO ₂	65	3.0×10^{14}
	71	3.8×10^{14}
	76	4.5×10^{14}
	80	4.7×10^{14}
	84	5.2×10^{14}
Chromia-doped UO ₂	66	3.3×10^{14}
	70	4.8×10^{14}
	74	5.4×10^{14}
	79	5.5×10^{14}
	83	5.7×10^{14}

The μ XRD results in Fig. 6.3 for the highest burnup fuel samples (83 and 84 MWd/kgU) are in good agreement with the TEM result (indicated in the figure by an arrow) of dislocation density ($6 \times 10^{14} \text{ m}^{-2}$) for a high burnup of 83 MWd/kgU PWR fuel [141]. It is also evident that the magnitudes of the GND densities as measured in the burnup range 70-80 MWd/kgU (Fig. 6.3) are in general agreement with the theoretically determined values of the total dislocation densities estimated for irradiated UO₂ as a function of burnup [168], though the computed dislocation density by J. Rest [168] slightly overestimates the GND density data for the low burnup of 66 MWd/kgU fuel. A comparison between the GND densities measured in the present study and the numerical analysis of dislocation density evolution in relation to burnup for irradiated UO₂ presented in Ref. [169], however, indicates that simulations overestimate the GND density in the higher burnup range ≥ 66 MWd/kgU. This observation suggests that further studies are needed to unravel the differences between experimental findings and the corresponding simulations. This is also because model predictions require a large set of material parameters [163,168-170] to describe dislocation nucleation and evolution in UO₂ fuel during irradiation. The resulting diffraction data in Fig. 6.3 also indicate that magnitudes of GND densities in the non-doped fuel are relatively lower than that of Cr-doped UO₂ in the burnup regime of 65-84 MWd/kgU, though the differences in observed GND density values are not great. At present, the reason for this difference is

not clear, possibly being related to the different elastic/plastic properties as well as stiffness (such as Young's modulus) of the materials [171,172], and differences in elastic responses of the standard UO₂ and Cr-doped UO₂ materials under irradiation [173].

6.2 Summary

In this chapter, the irradiation-induced damage evolution on a microscale level in standard UO₂ and Cr-doped UO₂ spent fuel materials has been studied. The quantitative experimental data on GND density based on lattice curvature measurements using spatially resolved micro-beam Laue diffraction technique is reported. Values of the GND density have been obtained by analyzing the Laue patterns formed by the (220) reflection, and changes in GND density have been investigated in irradiated UO₂ fuels at different burnups in the range of 65 to 84 MWd/kgU. As the burnup increases, the GND content is found to gradually increase in the burnup range 65-75 MWd/kgU and saturates at burnups exceeding 75 MWd/kgU. As a comparative result, it is noted that the variation of GND density with burnup in UO₂ follows a similar trend for non-doped and doped fuels when irradiated under comparable conditions. A comparison of our μ XRD result and the literature data obtained by TEM suggests that the upper limit of measurable dislocation density appears to be approximately $6 \times 10^{14} \text{ m}^{-2}$ for very high burnup UO₂ fuels. This is probably because of the measurement limitations of the employed μ XRD or TEM based technique in analyzing high burnup fuels, and the fact that very complex microstructural evolution and complicated atomic configurations of structural defects are produced by the nuclear fission process during irradiation. The experimental techniques used in the present study, applying a combination of XRD and XRF mapping measurements in a non-destructive manner employing micro-focused synchrotron light, represent a novel experimental approach to directly visualize spatially varying microscale strain distributions within irradiated UO₂ crystallites obtained through strain mapping, and to quantify local residual strain as well as the remnant dislocation contents in irradiated nuclear fuels.

7 Chemical State of Dopant Cr in UO₂

In this chapter, preliminary results of the chemical state of dopant Cr in fresh and irradiated DF, studied by micro-beam XANES spectroscopy, are reported and discussed. Chromium K-edge XANES spectrum allows direct determination of Cr oxidation state(s) in doped uranium dioxide lattice, and the spectral features of the XANES spectrum are sensitive to the local geometrical arrangement of the chromium ions in the UO₂ crystals. In previous studies [102,174], the grain microstructure and micro-scale spatial distribution of dopant Cr in a fresh DF (*i.e.*, FDF specimen) were examined in our laboratory by optical microscopy, SEM, EPMA and micro-beam XANES analyses. The results have shown that the doped fuel is characterized by large UO₂ grains whose average size is about 48 μm , and the as-fabricated pellet contains undissolved Cr₂O₃ particles dispersed in the UO₂ matrix. These secondary phase particles (SPPs) are formed by the precipitation of excess Cr₂O₃ as inclusions in the pellet due to limited solubility of Cr in UO₂ [68] at the given sintering temperature and conditions applied during the pellet fabrication process. The XANES experiments at the Cr K-edge were then conducted using a micro-focused synchrotron beam at particular SPP-free locations on the surface of the FDF specimen. The results indicated that most of the Cr atoms in the UO₂ lattice have a 3+ oxidation state. Also, the complex spectral shape of the observed XANES spectra reflected highly distorted local structural environment of the Cr ions with surrounding oxygen and uranium atoms. Further details on these results are described in Refs. [102,174]. For the purpose of the present study, a new fuel specimen from a fresh DF pellet have been prepared, and investigated by EPMA as well as micro-beam XANES spectroscopy to ensure the consistency with previous results of a similar study [102]. The second and main objective of the current study is to analyze the presence of toxic Cr⁶⁺ ions, if formed by the process of fuel sintering and fabrication of industrial-grade fresh DF pellets. The existence or absence of hazardous hexavalent Cr in spent fuel is also verified. The preparation of the spent fuel specimen (BDF-C), used in the XANES study, involved a FIB gun and the FIB/SEM examination prior to XRF and XANES analyses using synchrotron radiation-based micro-beam X-ray methods.

7.1 Specimen preparation

As pointed out in Chapter 2, only small-sized specimens, which are acceptable for safe use at the beamline, can be investigated using synchrotron-based experiments on radioactive materials. Therefore, small pieces of FDF specimens were prepared by cutting the original pellet into smaller ones, and a selected piece (about

2 mm × 1.5 mm × 1 mm in size) was mounted on a zirconium metal plate for investigation by XANES. For the preparation of an irradiated specimen, a fuel lamella of about 20 μm × 18 μm × 30 μm was created from the center region of the BDF pellet (*i.e.*, BDF-C specimen) using standard FIB-milling technique. The estimated local burnup of this FIB-ed specimen is about 68 MWd/kgU. This value is determined by the same procedure of ¹⁴⁸Nd method, as discussed earlier in Chapter 3. The final BDF-C specimen was transferred to a D-shaped molybdenum grid. A photographic image of the fresh fuel specimen, and a set of selected SEM images captured during FIB sectioning of BDF pellet are shown in Fig. 7.1.

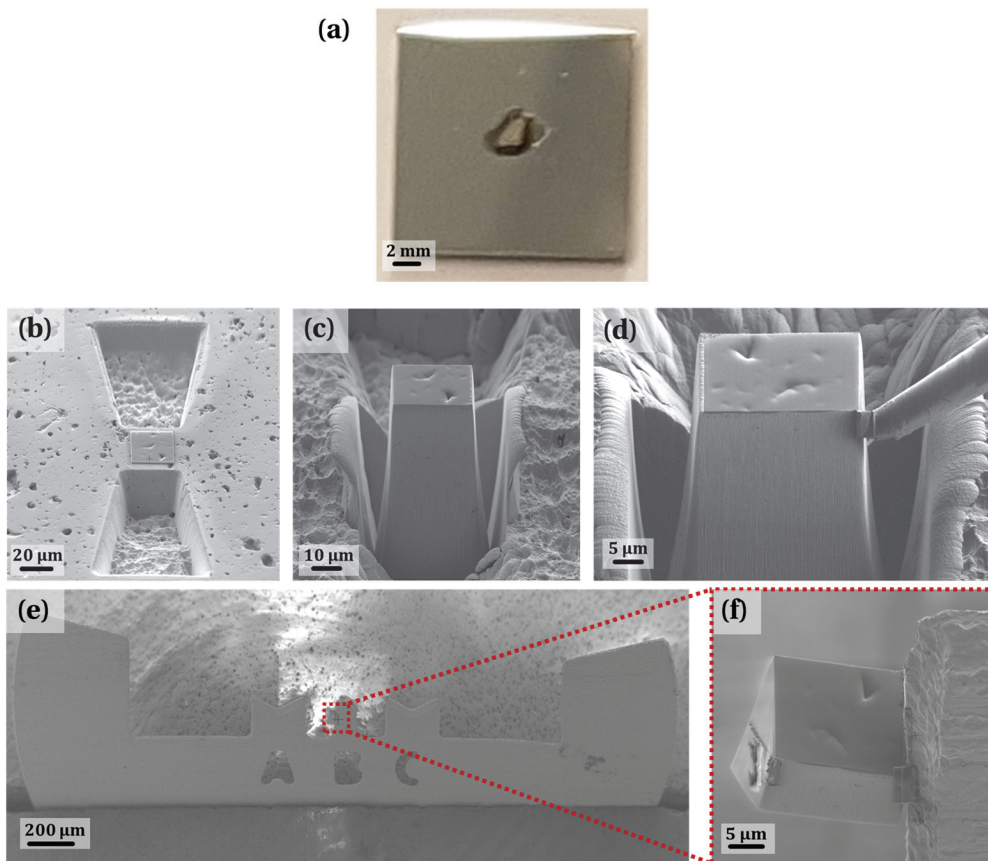


Figure 7.1: (a) Photographic image of the FDF specimen. (b)–(f) Set of selected SEM images collected during FIB-based lamella preparation. (f) The magnified view of the sample BDF-C. The specimens shown in (a) and (e) have been analyzed by XRF and Cr K-edge XANES.

7.2 EPMA studies

Element maps of Cr and O from a representative area of the fresh fuel specimen, obtained using EPMA analyses, are presented in Fig. 7.2. The presence of the Cr-bearing oxide phase, located at Cr and O hotspots, can be easily identified in the maps. The

dopant element Cr is found both dissolved in the UO_2 grains and precipitated as Cr_2O_3 in the fuel matrix.

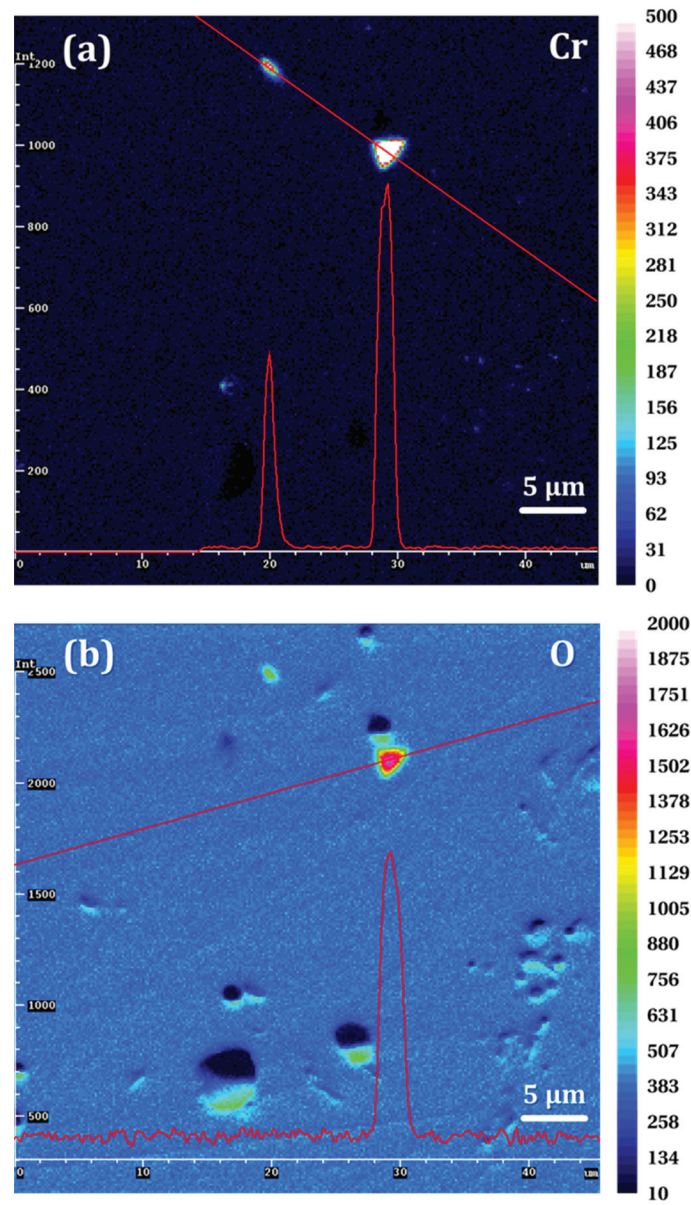


Figure 7.2: EPMA maps showing distributions of (a) chromium and (b) oxygen in the FDF specimen. EPMA line scan analyses of Cr and O across a selected Cr_2O_3 precipitate are shown. Analyses were made under measurement conditions of 10 keV and 90 nA with an electron beam spot size $\sim 0.1 \mu\text{m}$.

It may be mentioned here that the Cr content measured by EPMA in the UO_2 matrix is substantially lower than those of the Cr-bearing SPPs. The quantitative composition analyses suggest a varying non-stoichiometric composition of Cr_2O_3 , and the precipitates are mostly formed near the pores as well as at grain boundaries in the fresh fuel. Further details on the precipitate size distribution, their morphology,

crystallographic structure and the next neighbor Cr atomic environment in second phase chromia particles are described in Ref. [174].

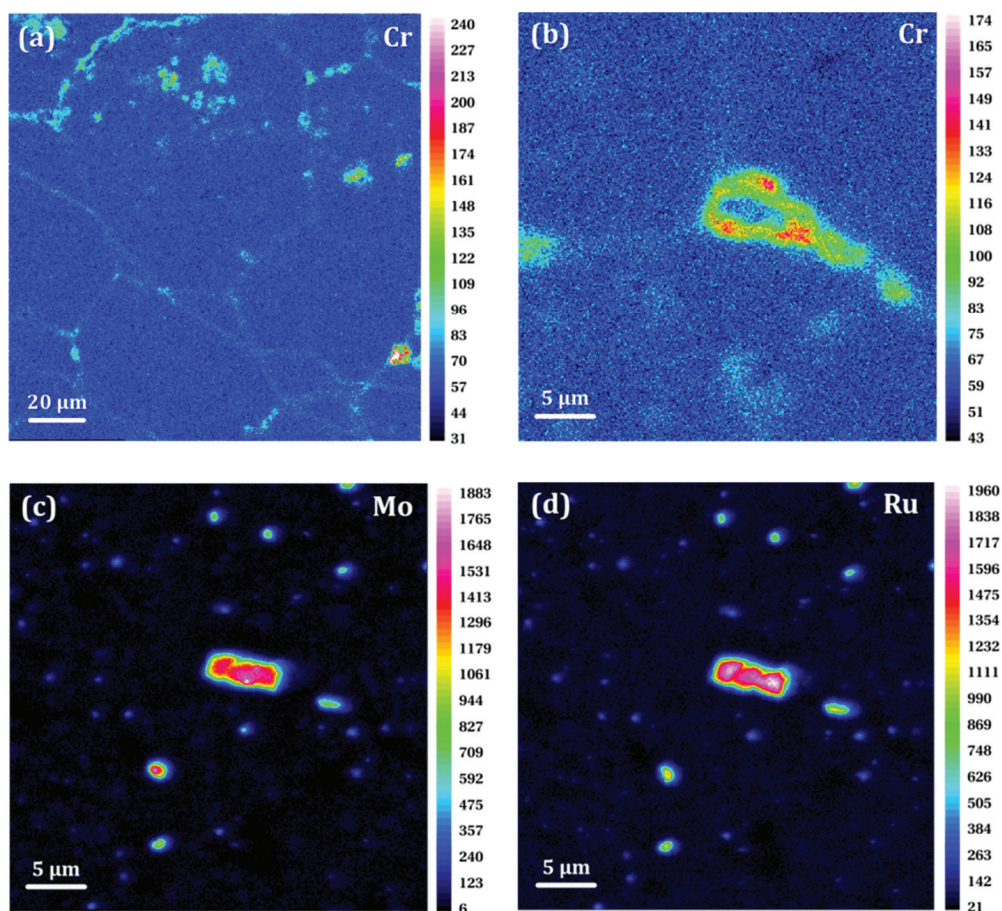


Figure 7.3: (a) An EPMA image of the dopant Cr collected from the center region of the BDF pellet. In (b)–(d), distribution maps of EPMA results for Cr, Mo, and Ru, obtained from the same sample area of the fuel and collected simultaneously, are shown.

The EPMA results of the distribution of Cr in the central region of the BDF pellet are shown in Fig. 7.3. It is observed that most of the Cr atoms are expelled from the UO_2 grains and migrated towards the grain boundaries, as shown in Fig. 7.3(a). Spots of dopant Cr and intermetallic Mo and Ru precipitates with different shapes are also observed (Figs. 7.3(b)–(d)). From these EPMA results, one may notice that there is an apparent spatial correlation of the dopant Cr with the metallic fission products, such as Mo and Ru, wherein the Cr appears to be surrounding the metallic fission product hotspots. The precipitation of chromium inclusions involving metallic fission products is non-homogeneous at those hotspots. To gain insight into the possible chemical binding of Cr with fission products and/or high-temperature redox reactions of solute Cr with the actinide ions, a set of micro-beam XANES spectra have been recorded from a Cr-rich hotspot area of the BDF-C specimen.

7.3 Synchrotron investigations

7.3.1 Micro-beam XRF analysis

Synchrotron μ XRF technique is very powerful for elemental analysis down to trace concentration levels like Cr in the studied specimens, and reveals spatially resolved information on Cr distribution in the DF.

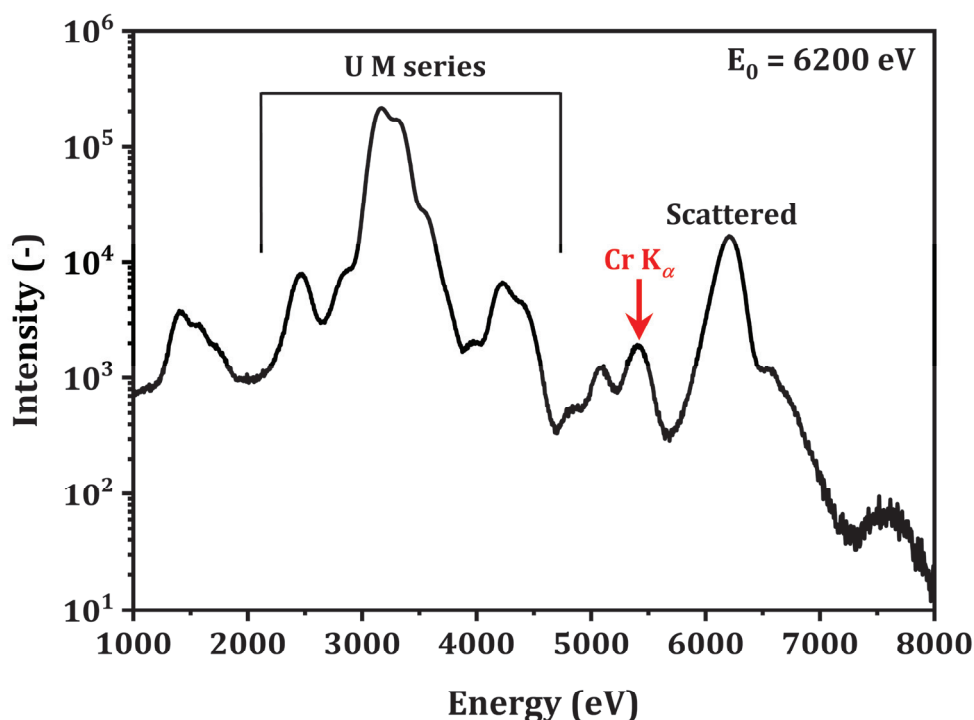


Figure 7.4: Synchrotron radiation induced XRF spectrum measured from the FDF specimen. The element Cr was detected in all regions of the specimen. The XRF peak of Cr is marked in the spectrum. The spectrum is measured with 6200 eV incident photons and collected for 15 s from a single spot location of the specimen.

The high intensity of available Cr-XRF signal has allowed to use shorter measurement times, which has enabled to record a few spectroscopic XANES spectra taken at different locations of the analysed samples. These measurements were carried out at the PHOENIX end-station of the PSI-SLS facility (details in Section 2.3.2). Figure 7.4 shows a representative XRF spectrum of dissolved chromium measured from the FDF specimen. It can be seen from the figure that U and Cr are the major elements present in the sample. Also, one can observe the elastic scattering peak with the spectral energy of 6200 eV which refers to the incident photon energy. At the low energy side between 1000 and 2000 eV, spurious XRF peaks are also detected.

7.3.2 Cr K-edge XANES

To elucidate the XANES spectra of the fuel specimens, Cr K-edge XANES spectra have been recorded from three reference powder specimens. The spectra are shown in Fig. 7.5. The first derivatives of the spectra are depicted in Fig. 7.5 as insets. The edge positions reveal energy values of 5989.0 eV, 5999.3 eV and 6005.0 eV for the Cr metal, Cr₂O₃ and CrO₃ oxides, respectively. This implies a chemically induced shift in Cr excitation energy when going from metallic Cr to Cr⁶⁺ oxidation state in CrO₃. It should be noted that a strong pre-edge peak at about 5992.3 eV is observed in Fig. 7.5(c), and it is only present in CrO₃.

In order to check the existence of any Cr⁶⁺ species in DFs, the pre-edge regions of the XANES spectra recorded from DF specimens have been analyzed. The analyzed results are summarized in Table 7.1.

Table 7.1: Measured edge energy and oxidation state assignment of Cr in various specimens.

Samples		Measured edge energy (eV)	Oxidation state of Cr
Reference materials	Cr metal	5989.0	0
	Cr ₂ O ₃ powder	5999.3	+3
	CrO ₃ powder	6005.0 Pre-edge at 5992.3	+6
Cr-doped fuels	Fresh	5999.5	+3
	Irradiated		
	Local BU: 68 MWd/kgU	5990.0	Mostly 0 when combined with metallic FPs

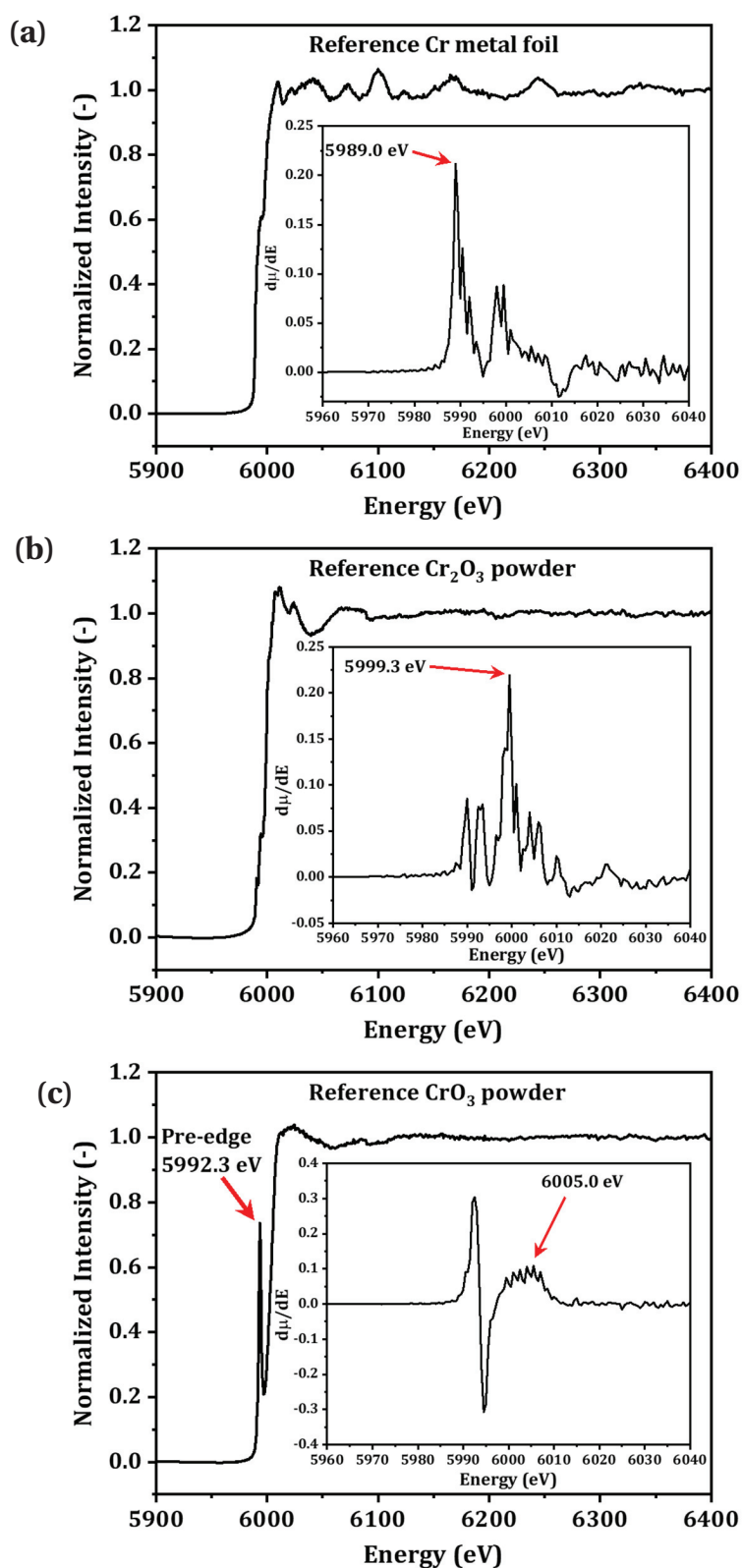


Figure 7.5: Normalized and background removed Cr K-edge XANES spectrum of (a) Cr metallic foil, (b) Cr_2O_3 powder, and (c) CrO_3 powder. In the insets, the first derivatives of the XANES data are shown which reveal the absorption edge energies.

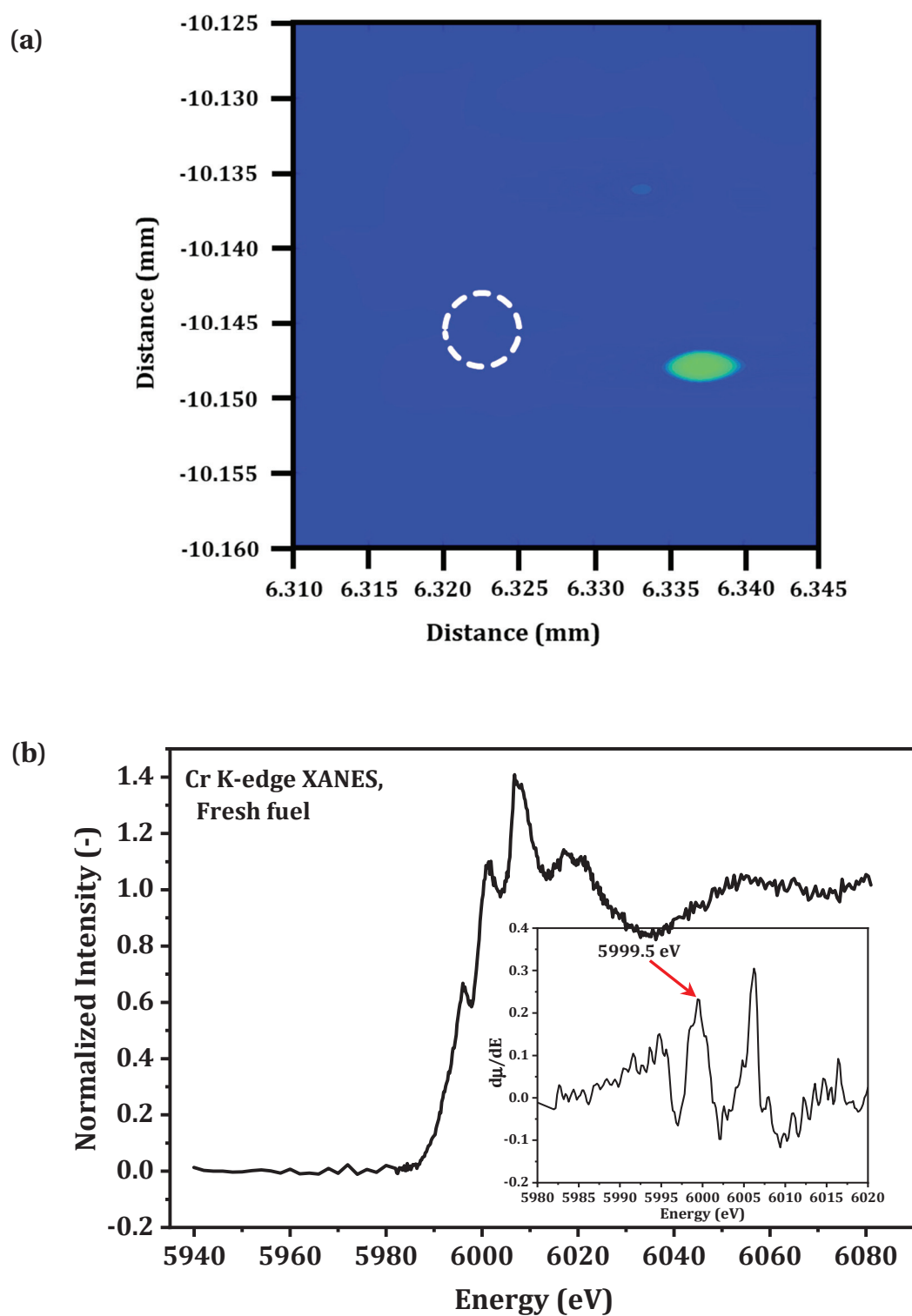


Figure 7.6: (a) Micro-beam XRF elemental chromium map obtained from the FDF specimen. (b) Micro-beam Cr K-edge XANES spectrum recorded from a precipitate-free area of the specimen marked by a circle in (a). The inset shows the first derivative of the XANES curve.

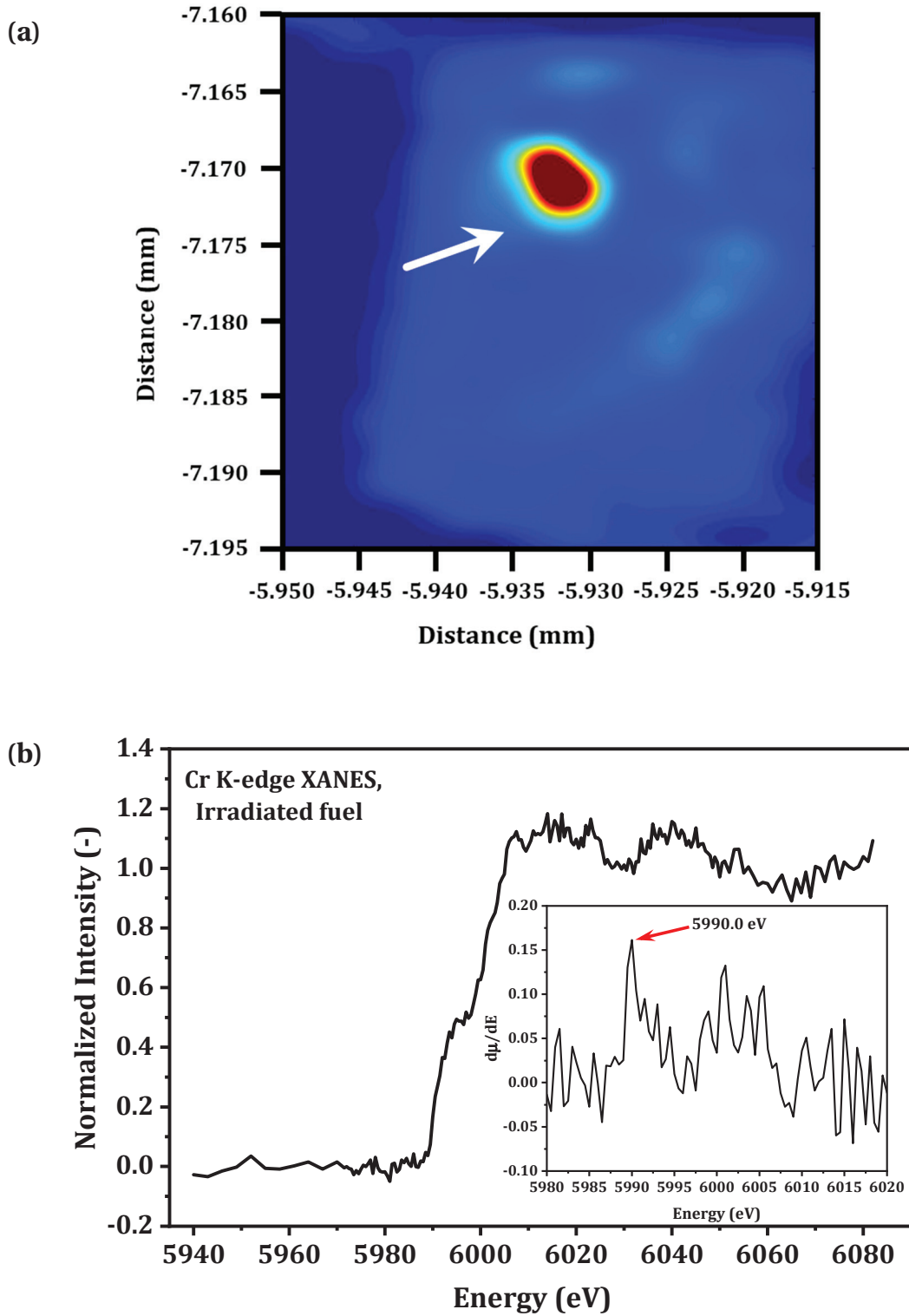


Figure 7.7: (a) Micro-beam XRF elemental chromium map obtained from the BDF-C specimen having a local burnup of about 68 MWd/kgU. (b) Micro-beam Cr K-edge XANES spectrum recorded from the Cr-rich hotspot area of the specimen marked by an arrow in (a). The inset shows the first derivative of the XANES curve.

An XRF intensity map of the chromium signal collected from the fresh fuel, showing spatial distributions of the Cr content in the specimen, is depicted in Fig. 7.6(a). Chromium is detected by μ XRF from both UO₂ grains (the dissolved Cr-component) and Cr-containing precipitates present in the fresh fuel. The presence of undissolved chromia particles as hotspots can be clearly seen in the map of Cr in Fig. 7.6(a). The XANES spectrum of solute dopant, shown in Fig. 7.6(b), provides information about the valence state(s) of Cr in the analyzed region of the sample. The energy position of the main edge, obtained from the first derivative of the XANES curve, is determined to be 5999.5 eV. This implies that solute Cr atoms, located in the UO₂ grains, exist in a trivalent oxidation state. Below the main edge, the presence of a peak-like tiny feature, which provides a centroid energy position at 5995.5 eV in the first derivative spectrum (inset in Fig. 7.6(b)), is also visible in the Cr K-edge XANES. The structural origin of this spectral feature is still unclear, and may be related to the presence of divalent chromium ions in the fuel. These results imply that Cr(III) is the dominant species in the UO₂ grains. It should be noted that there is no evidence of the pre-edge peak at about 5992.0 eV in the Cr K-edge XANES spectrum acquired from fresh fuel. This result confirms absence of any hexavalent Cr(VI) in the fresh fuel.

A micro-beam XRF area map, showing the distribution of Cr in the FIB-ed specimen, is depicted in Fig. 7.7(a). A Cr-rich hotspot can be easily identified in Fig. 7.7(a). It is also clear from the mapping image that there are regions where low and variable concentrations of Cr are accumulated in the irradiated specimen. Combining synchrotron μ XRF and EPMA based results, it appears that these areas with low Cr concentrations represent the grain boundary areas of the UO₂ fuel. In the present study, the marked Cr-rich region in the XRF image (Fig. 7.7(a)) was analyzed by μ XANES spectroscopy. The Cr K-edge spectrum is shown in Fig. 7.7(b). The main absorption edge energy, determined from the centroid position on the first derivative of the XANES curve (inset in Fig 7.7(b)), is found to be 5990.0 eV. This value is 1.0 eV higher and close to the measured K-edge energy of the Cr metal foil (Table 7.1). By comparing the two XANES spectra of fresh and irradiated specimens, one can also observe that the spectral shape as well as intensity of the white line in the Cr XANES of the irradiated fuel have changed drastically. The present XANES results of irradiated DF confirm that the oxidation state of Cr is reduced from Cr(III) (*i.e.*, in FDF specimen) to lower and mixed valence states. The XANES spectral shape reflects the presence of different Cr-bearing species together with intermetallic FPs, and provide an indication that a fraction of chromium is reduced to metallic state. Finally, it should be mentioned that the presence of hexavalent Cr(VI) (the most toxic form of chromium bearing compounds) is not detected in the BDF-C sample.

7.4 Summary

This study describes preliminary results of the EPMA and XANES experiments performed on fresh and irradiated DF to determine the Cr oxidation state in the specimens analyzed. The as-fabricated fuel contains Cr-rich undissolved Cr_2O_3 particles, which were mapped with EPMA and micro-beam XRF spectroscopy. In order to determine the oxidation state of Cr in the fuels, Cr K-edge XANES spectra have been measured with a micro-focused X-ray beam spot. Dissolved chromium ions, located in the UO_2 grains of the fresh fuel specimen, are found to be in the trivalent state. In irradiated fuel, Cr is found in the oxide matrix at and near the UO_2 grain boundaries, and also locally together with metallic FP elements, like Mo, Ru, *etc.*, at central locations in the spent fuel pellet. Preliminary XANES experiments, performed at a selected region on the irradiated specimen, indicate that the oxidation state of Cr is reduced from Cr(III) (*i.e.*, in fresh fuel) to lower and mixed valence states. Another finding is that hexavalent Cr(VI) (the most toxic form of chromium bearing compounds) is not detected in both fresh and irradiated DF.

8 Chemical Speciation of U and Pu in Standard UO_2

This chapter outlines a synchrotron based micro-beam XAS study to examine the local atomic scale structure around uranium atoms in the as-fabricated UO_2 pellet, and the next neighbor atomic environment of uranium and plutonium in the spent fuel (PSF-R) specimen having a local burnup of around 50 MWd/kgU. The spectra at the U and Pu L_3 -edge have been measured and quantitatively analyzed by the conventional least-squares fitting procedure that uses ab-initio FEFF simulations [175]. Prior to the XAS investigation, SEM analysis was undertaken to analyze the UO_2 grain microstructure in the spent fuel pellet. In addition, EPMA has been performed (see Chapter 3) for quantitative analyses of uranium, plutonium, oxygen, and as selective fission product neodymium being a recognized burnup indicator of nuclear fuel. The obtained experimental results of this study on the chemical and local structural specificity of U and Pu in irradiated UO_2 matrix shall be useful for fuel modelling studies that could account for the UO_2 fuel lattice defects evolution as well as fission products and/or actinide products behavior under irradiation conditions. This chapter contains the research results from one of the articles published by the author [176].

8.1 Micro-beam XRF analysis

The $L\alpha$ XRF intensity recorded using synchrotron light from the PSF-R specimen (of local burnup ~ 50 MWd/kgU) provides high counting statistics for short data acquisition time, which enables low concentration of Pu isotope to be detected and analyzed by XAS. Figure 8.1 shows an example of the synchrotron radiation excited XRF spectrum of the spent fuel sample, recorded with an excitation energy of 19000 eV. The characteristic peaks of matrix element uranium and the actinide product plutonium are indicated in Fig. 8.1. U $L\alpha$ and Pu $L\alpha$ fluorescence were measured while scanning the incident photon energy to acquire the XAS spectra.

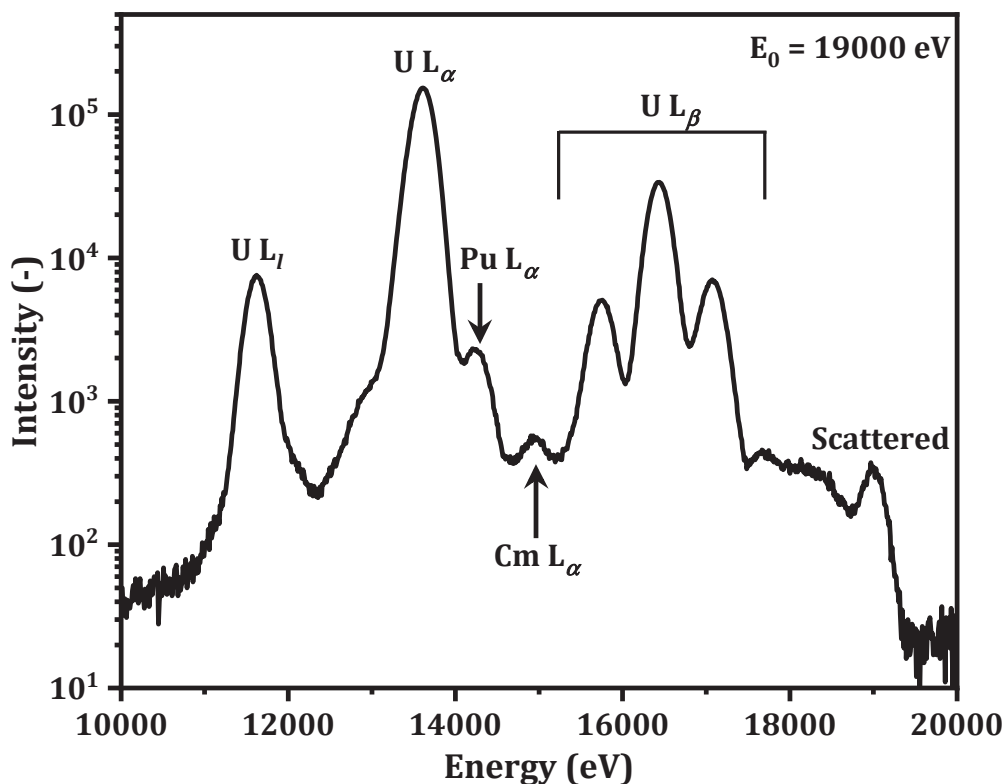


Figure 8.1: Micro-beam XRF spectrum of PSF-R specimen measured using synchrotron light.

8.2 Micro-beam XAS investigations of spent fuel

8.2.1 Uranium speciation

Figure 8.2 shows the U L_3 -edge XAS spectra measured from the two UO_2 fuel samples investigated, namely FSF and PSF-R. Comparison of the two XAS spectra for pristine UO_2 and irradiated UO_2 shows that the spectral features in both XANES and EXAFS regions are notably different. In the case of irradiated UO_2 , the white line intensity at U L_3 -edge XANES is higher compared with that of pristine UO_2 . In the EXAFS region, which extends about 50 eV beyond the edge, the shape of the two absorption curves in Fig. 8.2 are not strictly identical, as also reflected in the RDF spectra in Fig. 8.3. However, the first derivatives in the XANES regions of the absorption curves, replotted in the inset of Fig. 8.2, reveal an E_0 value of 17170 ± 1.0 eV implying that uranium mainly exists in the tetravalent state in both the fuels.

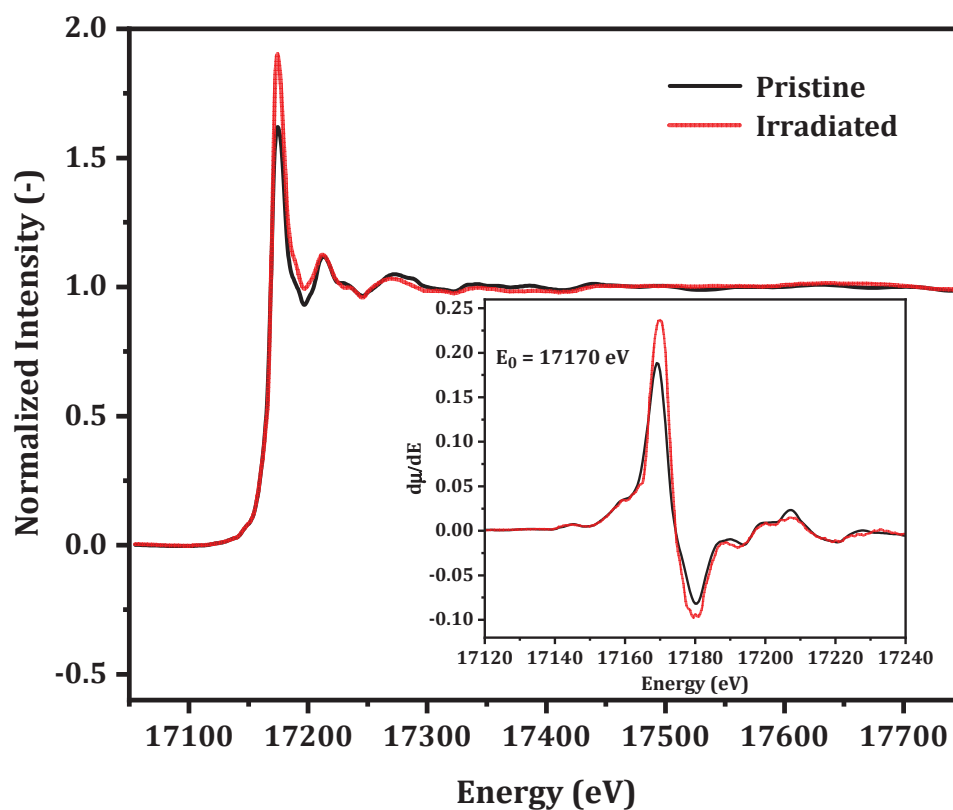


Figure 8.2: Comparison of the U L₃-edge XAS spectra measured from the FSF and PSF-R samples analyzed. The inset shows the first derivative of the XANES spectra, used to characterize the oxidation state of uranium in the fuels.

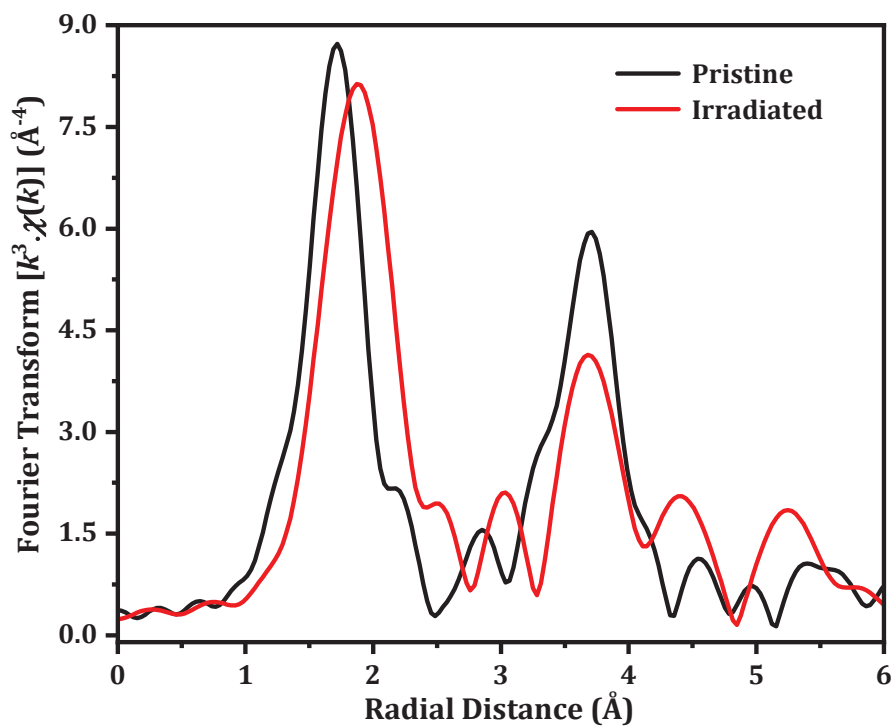


Figure 8.3: k^3 -weighted FT-EXAFS data shown in the overlap mode for fresh and irradiated UO₂ samples.

The k^3 -weighted RDF spectra of the two samples are compared in Fig. 8.3. FT-EXAFS gives two separate peaks at about 1.8 Å and 3.7 Å. The first strong-amplitude peak due to single scattering at about 1.8 Å stems from the first neighbor oxygen atoms of the UO₂ lattice. The magnitude intensity of the second peak near 3.7 Å is sensitive to the coordination number as well as geometry of second neighbor uranium atoms, and contain multiple scattering contributions from distant shells. Differences in the RDF spectra of pristine UO₂ and irradiated UO₂ are clearly visible in Fig. 8.3. The FT-EXAFS of PSF-R specimen clearly shows a shift of the first major peak to a larger R value and a reduction of the peak height compared to that of the pristine UO₂. The FT-EXAFS peak amplitude of both U–O and U–U atom shells in the irradiated sample is effectively decreased implying atomic scale structural modifications of the UO₂ lattice as a result of neutron irradiation.

Modeling of the RDF data beyond the first shell for atoms at distances larger than 2.5 Å in Fig. 8.3 would require individual single scattering paths and multiple scattering contributions as computed by FEFF. In fact, each scattering path has four adjustable parameters (R , N , σ and E_0) to be optimized by fitting the experimental FT-EXAFS. Clearly, when a large number of fitting parameters are involved, a meaningful EXAFS refinement becomes more difficult. Therefore, curve fitting analysis was restricted to the first FT peak near 1.8 Å for an easy derivation of U structural parameters in the first neighbor oxygen shell. After extracting the U–O shell component from the RDF spectra, the Fourier filtered data were best-fitted using R , N , and σ as all free parameters in the standard single-scattering EXAFS formula to obtain more reliable fit results.

Figures 8.4(a) and 8.4(b) show the inverse Fourier transform of the filtered first FT peak of pristine and irradiated UO₂, respectively. The fitted curves are shown with solid lines in Fig. 8.4. As can be seen, there is a good agreement between the experimental data and theoretical best-fit curves.

The extracted structural parameters are provided in Table 8.1. For the pristine UO₂, the values of structural parameters are: a U–O coordination number $N = 7.8 \pm 0.2$ at a distance of $R = 2.36 \pm 0.02$ Å, a Debye-Waller factor of $\sigma^2 = (60 \pm 5) \times 10^{-4}$ Å² and $\Delta E_0 = 1.6$ eV. These best-fit values are in a good agreement with those reported in the literature [177,178]. The fitting procedure in the EXAFS analysis of irradiated UO₂ resulted in $N = 7.1 \pm 0.2$, $R = 2.41 \pm 0.02$ Å, $\sigma^2 = (89 \pm 8) \times 10^{-4}$ Å² and $\Delta E_0 = 1.6$ eV (held fixed at this value derived from the experimental data of the pristine UO₂ sample). These results show structural variations in the neutron irradiated UO₂ compared to the crystallographic data of pristine UO₂. The observed changes are a lengthening of the mean U–O bond distance (~2.41 Å) in the first coordination shell of uranium compared to the crystalline value of 2.36 Å, and there is a significant reduction of the coordination number of the first U–O shell in the spent fuel sample relative to the un-irradiated UO₂ sample. The σ^2 value of the U–O pairs in irradiated matrix is notably higher compared to that of the pristine UO₂, implying local distortion around the metal centers and

positional disorder in the oxygen sub-lattices due to strong radiation damage in the irradiated spent fuel matrix.

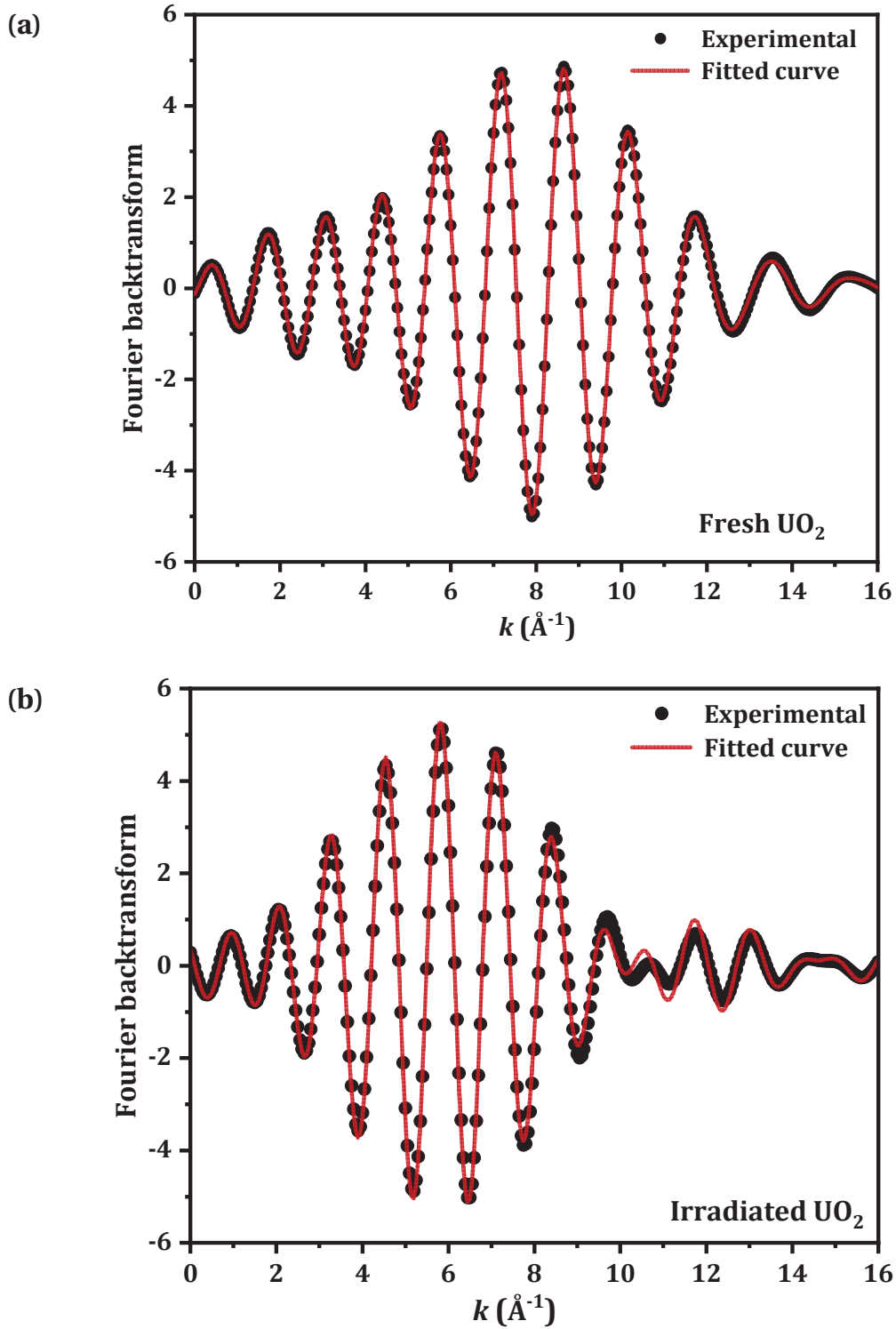


Figure 8.4: First shell (U–O) Fourier-filtered experimental (dotted symbol) and best-fitted (solid curve) spectra of (a) pristine UO_2 , and (b) irradiated UO_2 . See text for details.

Table 8.1: Structural parameters (R , N , σ and E_0) of fresh and irradiated standard UO₂ fuel.

Structural parameters	Fresh standard UO ₂	Irradiated standard UO ₂ (Local BU: 50 MWd/kgU)
ΔE_0 (eV)	1.6	1.6
Bond distance, R (Å)	2.36 ± 0.02	2.41 ± 0.02
Coordination number, N	7.8 ± 0.2	7.1 ± 0.2
Debye-Waller factor, σ^2 (Å ²)	$(60 \pm 5) \times 10^{-4}$	$(89 \pm 8) \times 10^{-4}$

8.2.2 Plutonium speciation

An example of the measured Pu L₃-edge XAS spectrum of the irradiated UO₂ sample is shown in Fig. 8.5. The edge position, taken as equal to the maximum value of the differential coefficients of the spectrum near the edge, provides an energy value of 18062.5 eV implying Pu⁴⁺ as the predominant oxidation state in the spent fuel. The peak position of the white line in the XANES region lies at 18068.6 eV, which is very close to the reported energy value of the white line peak measured at the Pu L₃-edge in PuO₂ material [179].

To evaluate the Pu speciation in the spent fuel, the XAS data reduction has been performed, and extracted FT-EXAFS signals in the limited k range have been preliminarily examined. Figure 8.6 shows k^l -weighted FT-EXAFS data (in the k range 1.5–7.0 Å⁻¹ and phase-uncorrected). The first FT peak occurs approximately at about 1.7 Å, which represents the first shell Pu–O pairs of (U_{1-y}Pu_y)O₂ solid solution formed inside the irradiated UO₂ pellet. It is noted for the Pu L₃-edge spectrum, as shown in Fig. 8.5, that the spectral features in the EXAFS regions of the absorption curve display noisy ripples and bumps in the data. The origin of this noise is related to the poor detection efficiency of low concentration XRF-Pu with a high counting rate of XRF-U in XRF/XAS measurements. Therefore, due to limited data quality, a complete quantitative analysis of the local structure around the Pu(IV) ions cannot be correctly performed using the XAS data presented in Fig. 8.5. New experimental work, using energy dispersive multi-elements XRF detectors and/or wavelength dispersive spectrometers, could be undertaken to circumvent the problems encountered.

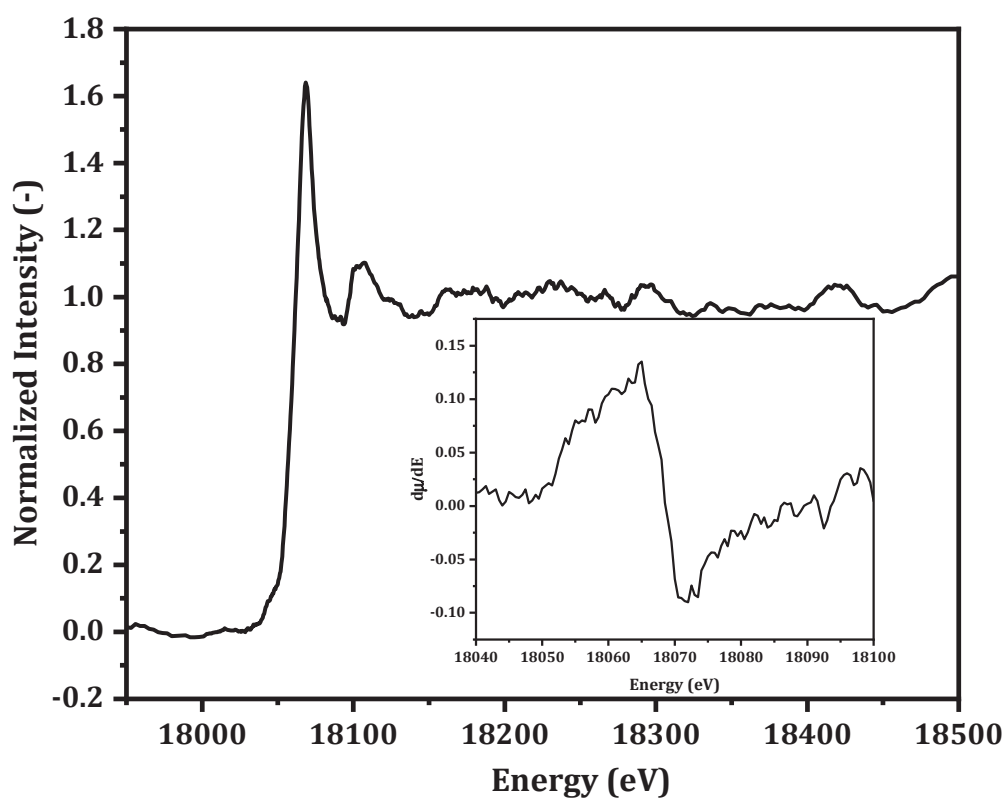


Figure 8.5: Pu L₃-edge XAS spectrum measured from the spent fuel UO₂ (PSF-R) specimen. In the inset, the first derivative of the XANES data is presented.

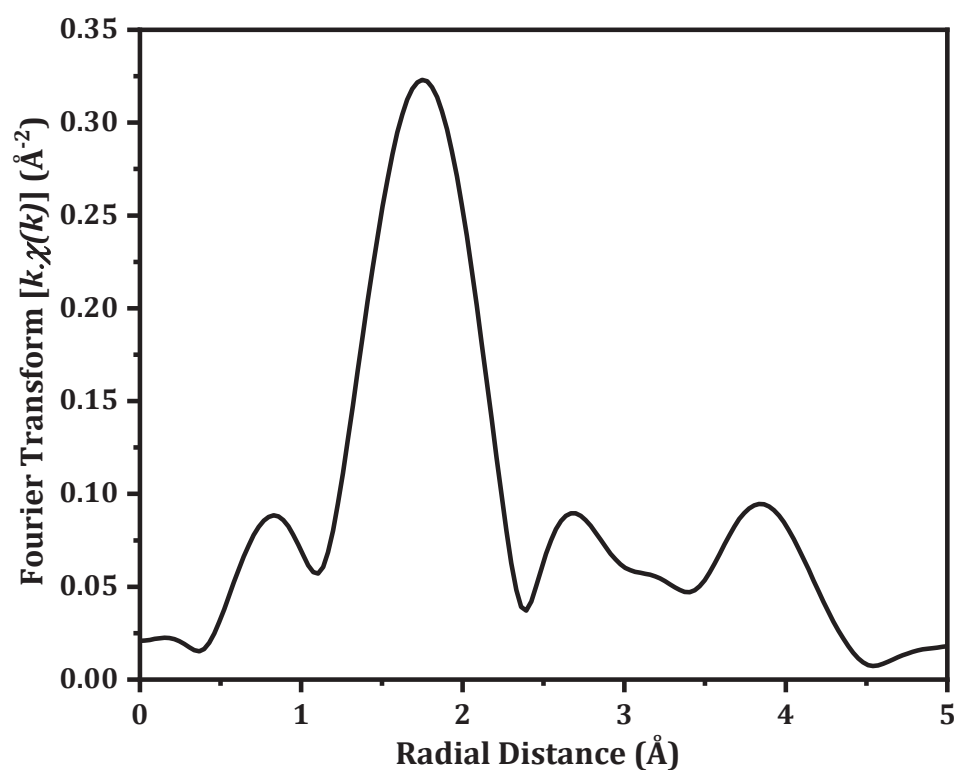


Figure 8.6: Radial distribution function (k^l -weighted) of the Pu L₃-edge EXAFS data shown in Fig. 8.5.

8.3 Summary

This chapter reports the application of μ XAS to the study of atomic-scale uranium and plutonium environment in reactor exposed UO₂ fuel material. XANES was applied to investigate chemical (oxidation) state of uranium and plutonium in a spent fuel specimen. EXAFS has been used to probe U–O local bonding configurations in the spent fuel. The results show a distortion of the U(IV) coordination environment by oxygen atoms in the irradiated matrix, and the EXAFS technique has provided sub-Ångström scale measure of the local distortion resulting from irradiation effects. Preliminary assessment of the Pu L₃-edge XAS data reveals that Pu has a chemical valence of four and is present as U–Pu solid solution in the irradiated fuel.

9 Analysis of Fission Gas using TEM

In previous chapters 5 and 6, experimental results of spatially varying microscale strain distributions within irradiated UO_2 crystallites and the dislocation density yield as a function of local fuel burnup in spent fuels are presented and discussed. The lattice strain and extended defect development are attributable to dissolution of soluble FPs, precipitation of insoluble FPs, formation of over-pressurized fission gas bubbles and irradiation damage accumulation in the fuel matrix. In this chapter, the results of preliminary TEM investigations of irradiation-induced microstructural evolution in spent fuels are reported. Of particular interest are the accumulation of fission gas atoms (*e.g.*, Xe and Kr) into pressurized bubbles and re-solution of gas atoms from fission gas bubbles. It is well known that gas atoms depletion in UO_2 fuel and subsequent bubbles precipitation induce local strain fields in the irradiated UO_2 matrix, which may then cause micro-scale crack initiation and lead to increased gas release from the fuel matrix.

Under normal irradiation conditions in the reactor, the majority of the fission gases are mostly retained within the fuel matrix. The precipitated gas bubbles within the fuel grains can have a spatial variation in local population density and size distribution depending on the local fuel burnup (*i.e.*, fission gas yield), temperature experienced by the fuel, and applied power history in the fuel pin. In addition, pressure of gas bubbles can differ significantly, ranging from MPa to GPa values, which depends on the sizes of the bubbles. In the present study, TEM analyses of PSF-R and PSF-C specimens were carried out to quantify the mean size, spacing size distribution and number density of gas bubbles, which are needed for the better understanding about the role of gas bubbles on the microstructural evolution in irradiated nuclear fuels.

9.1 Distribution of fission gas bubbles

The diffusion process of fission gas atoms can be adequately characterized by two separate processes. Once formed within the fuel grains, the gas atoms tend to migrate to the grain boundaries and/or regions of defects owing to their very low solubility in the UO_2 matrix. These diffusing atoms also cluster together to form precipitates followed by nucleation and growth of gas bubbles by trapping local gas atoms. During irradiation, many of the nanometric intragranular gas bubbles are destroyed, both partially and completely, due to collision with other fission fragments, the so-called *re-solution* process that tends to dissolve the enclosed gas in the original bubbles [33,180]. The

saturation of the intragranular bubbles within the irradiated matrix is known to occur rather quickly [181].

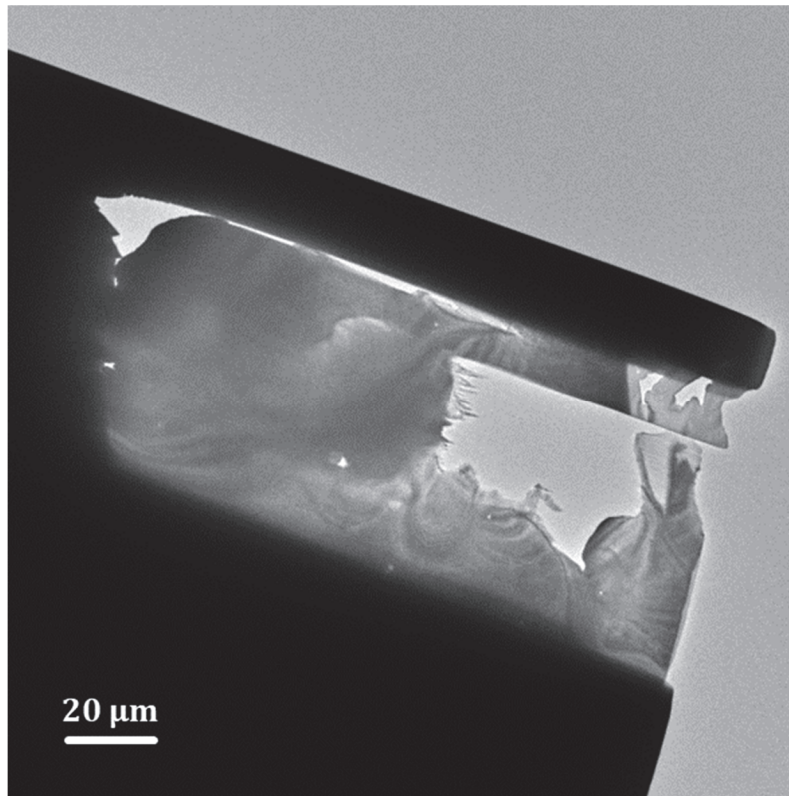


Figure 9.1: Broad view of the PSF-C specimen investigated by TEM. See text for details.

Two TEM lamellae, prepared by FIB-milling method from the PSF pellet, were investigated by JEOL ARM-200F (NeoARM) TEM instrument. The microscope is probe-corrected, and equipped with cold field-emission electron gun and double electron dispersive spectrometer (EDS) detectors. The instrument operates at 200 keV energy (wavelength of ~ 0.025 Å). Figure 9.1 shows the electron micrograph of the TEM lamella prepared from the center region of the PSF pellet (PSF-C specimen). The final TEM lamellae have a thickness variation in the range from 80 to 120 nm within the active layers of the specimens.

Fig. 9.2 shows the distribution of nano-sized fission gas bubbles anchored at the grain boundaries of nano-sized UO_2 grains in the fuel, observed for the PSF-R specimen that has a local burnup of around 65 MWd/kgU. The grain boundaries are regarded as sinks for the fission gases, and these grain boundaries serve as pathways for fission gases to be released from the fuel pellet.

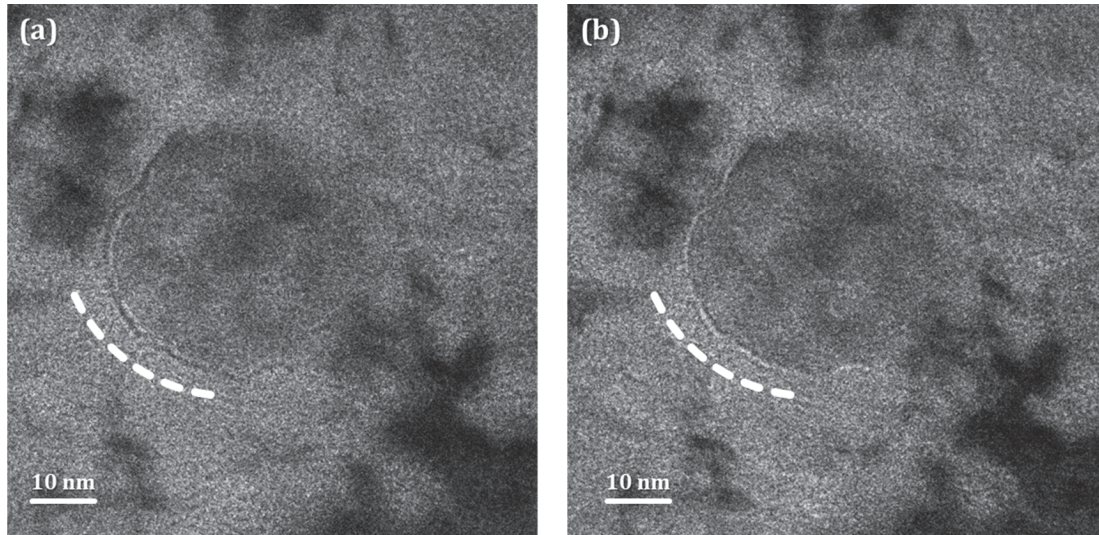


Figure 9.2: TEM images showing the distribution of gas bubbles decorating the grain boundaries of nano-sized UO_2 grains observed for the PSF-R specimen. The images are taken in (a) over-focus mode, and (b) under-focus mode.

A second observation is the high density population of nanometric fission gas bubbles, distributed heterogeneously throughout the irradiated matrix. Fig. 9.3 shows the bright-field TEM image of PSF-R specimen. For this 65 MWd/kgU burnup fuel, the mean diameter and number density of fission gas containing bubbles are estimated to be about $2.54 \times 10^{22} \text{ m}^{-3}$ and 5-6 nm, respectively.

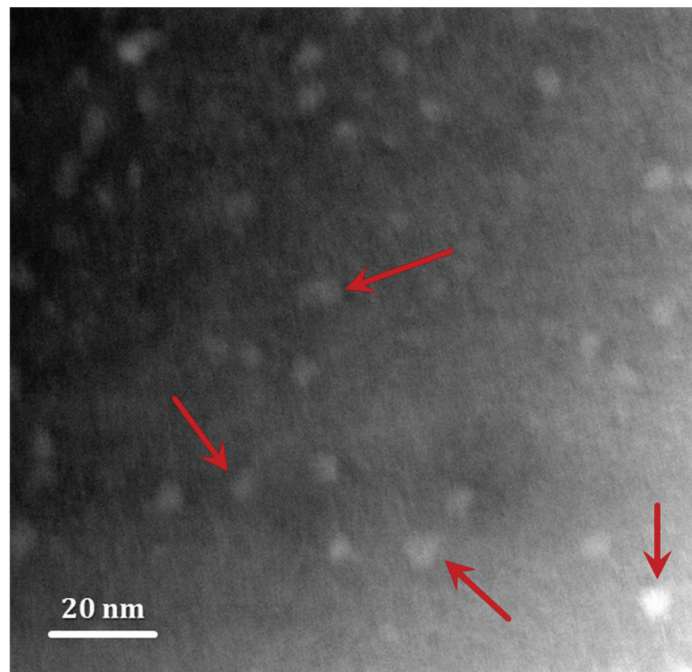


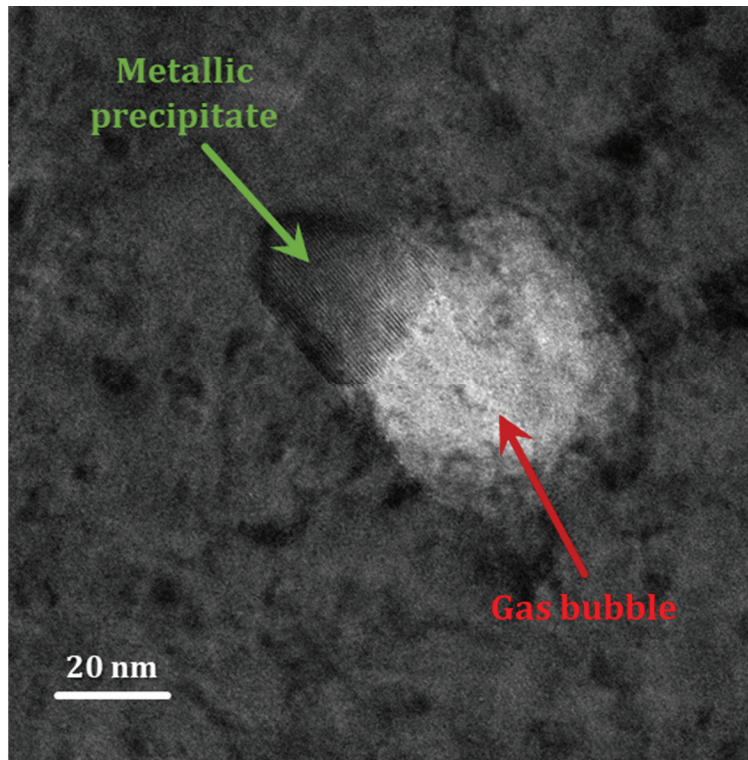
Figure 9.3: Bright-field electron micrograph image showing gas bubbles distribution in the PSF-R specimen.

These values are in reasonable agreement with the findings (bubble size ~8 nm, bubble concentration $1-2 \times 10^{22} \text{ m}^{-3}$) of Ray et. al [182]. At the same time, it is also noted that the number density of gas bubbles determined in this study differs significantly from those reported in Refs. [183,184]. The reason for this discrepancy is unknown, but may be specimen related and the differences in the irradiation conditions of the reactor exposed fuels analyzed in this study.

For the lower burnup (~40 MWd/kgU) PSF-C specimen, fission gas bubbles were also observed in the TEM micrographs. Attempts were made to acquire high-magnification TEM images from different locations of this specimen for the quantification of the bubble number density and bubble size via image analysis. Although the presence of small isolated bubbles in nano-scale (in the range of 2-4 nm) could be easily detected at some locations of the TEM specimen, it was difficult to determine their area number densities because of difficulties in isolating all gas bubbles from some cloudy-like contrast features, perhaps related to nano-sized pores/voids of irregular shapes, which were also observed in bright-field TEM images.

In some areas of the PSF-C specimen, larger fission gas bubbles of sizes ranging from 30-100 nm were also seen. It is noted that these large bubbles are sparsely distributed in the UO_2 matrix, and they are mostly attached to metallic fission product (*e.g.*, Mo, Tc, Ru, Rh, Pd, *etc.*) precipitates, as evidenced from EDX measurements. Representative TEM images of large fission gas bubbles and precipitates of metallic fission products, observed for the PSF-C specimen, are shown in Figs. 9.4(a) and 9.5(a). The EDX spectra from metallic precipitates are shown in Figs. 9.4(b) and 9.5(b). Nano-area EDX analysis shows that the main elements are U and O from the fuel matrix, along with minor amounts of Cs and Mo that are present locally in the sample. At this point, it is necessary to mention that the obtained results on bubble size and bubble distribution, reported in this study, are only preliminary. Further TEM examinations at various locations of the samples are essential to obtain statistically significant information about the bubble number density and the bubble size distribution considered here, and to provide a better representation of our experimental results.

(a)



(b)

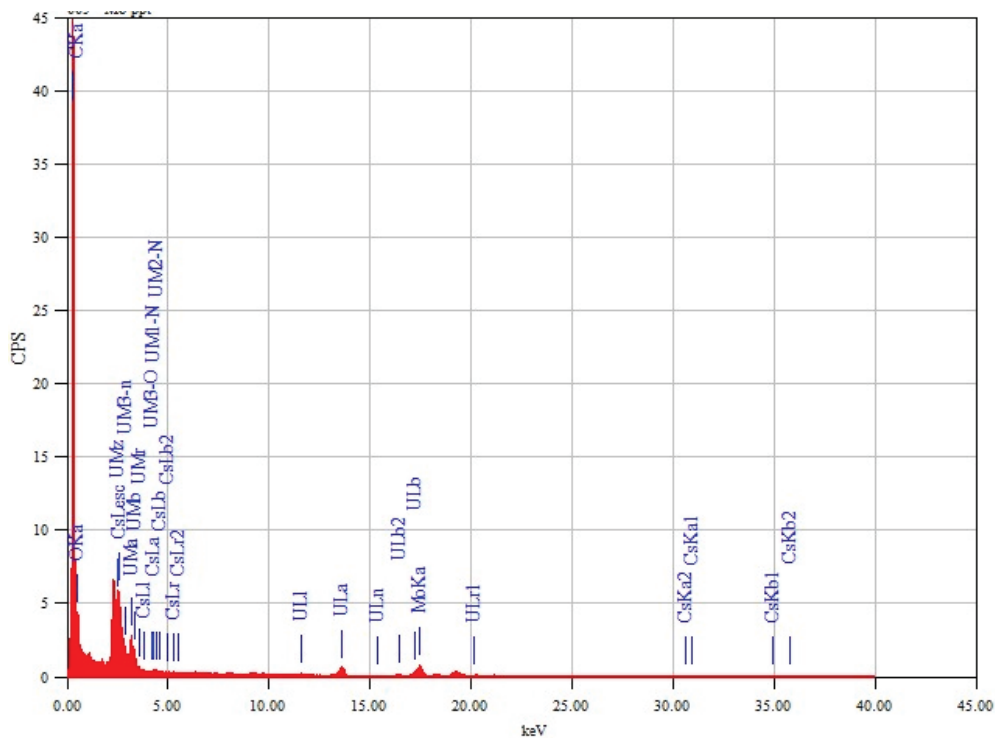


Figure 9.5: (a) TEM image of a large fission gas bubble (~45 nm) touching a precipitate, which consists of metallic fission products. (b) An EDX spectrum recorded from the precipitate region. The characteristic Mo peak can be observed in the spectrum.

9.2 Lattice imaging and SAEDP analyses

It was of interest to also investigate the atomic scale structure of UO_2 crystals in spent fuel by TEM, and to determine the lattice parameter via lattice-plane counting from experimental TEM images. Figure 9.6(a) shows a high-resolution TEM image of the PSF-R specimen, which has a local burnup of 65 MWd/kgU.

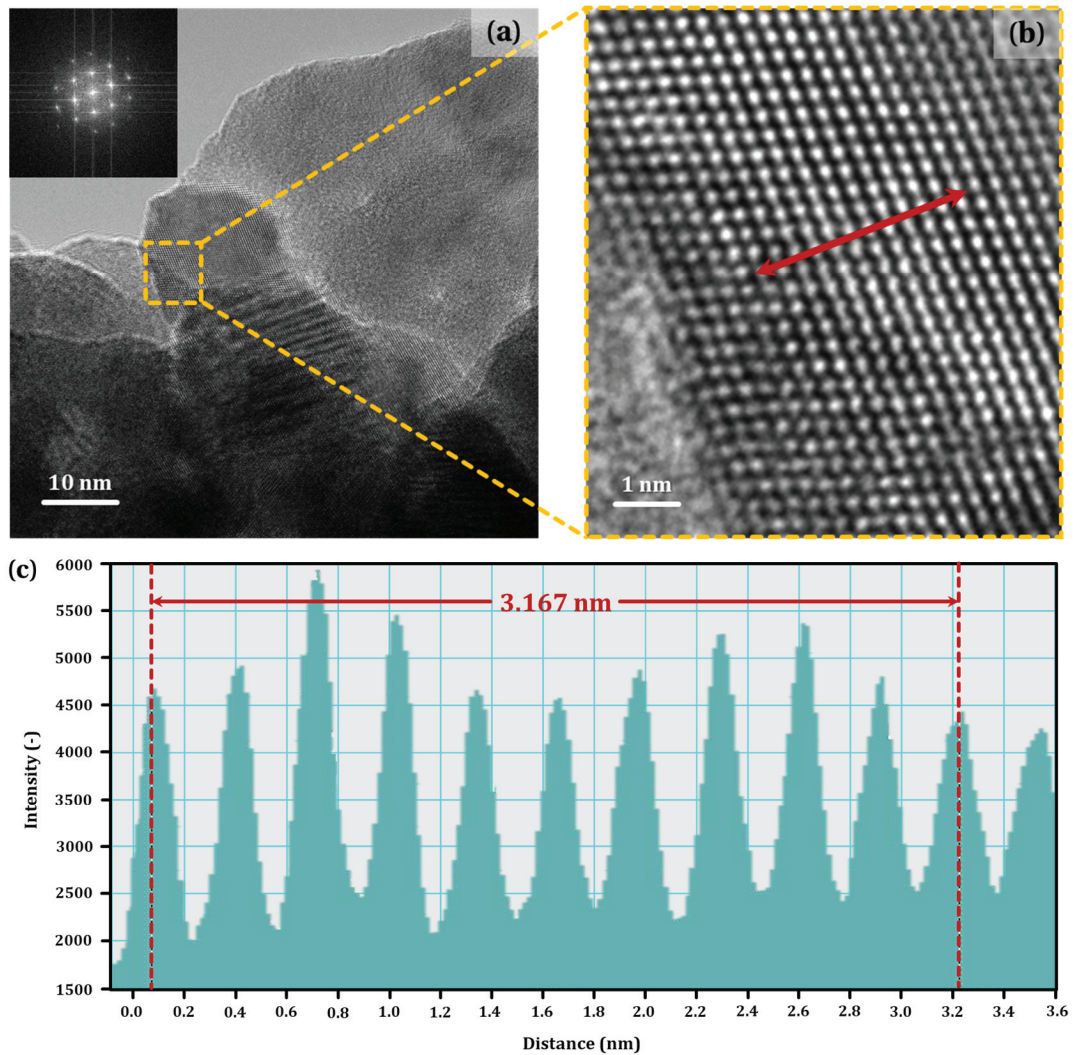


Figure 9.6: (a) Bright-field TEM image of a selected area of the PSF-R specimen showing UO_2 sub-grains that originate from polygonization of the original ‘mother’ grains. The image was taken from the [011] crystal orientation. **Inset:** Fast Fourier transform of lattice image from the area outlined by a yellow dotted box. (b) High-resolution TEM lattice fringe image of the region highlighted by the yellow square in (a). (c) Quantitative analysis of inter-planar lattice spacing. Profile in a rectangular frame showing eleven successive lattice strips along the {111} planes. See text for details.

The image corresponds to the [011] zone-axis of the fluorite-type structure. Compacted UO_2 grains with a nanoscale grain size distribution can be observed from the TEM image. Similar grain-refined regions are also found in other parts of the same TEM specimen. The lattice fringe micrograph of a small region, indicated by a yellow bounding box in Fig. 9.6(a), is presented Fig. 9.6(b). The observed strips in the image correspond to the {111} crystals planes in UO_2 . Using standard image processing software and applying lattice fringe analysis algorithm, quantitative analyses of lattice fringe spacing have been carried out on recorded high-resolution TEM micrographs. In Fig. 9.6(c), intensity profile of the selected lattice strips for the {111} planes of the UO_2 crystal, taken from the region highlighted by the red arrow in Fig. 9.6(b), is presented. The distance between the strips provides information about the interplanar distance in the {111} planes. The d -spacing of {111} planes, calculated averagely from ten successive lattice stripes (see Fig. 9.6(c)), is found to be 0.3167 nm. The lattice spacing, d_{111} , is related to the lattice constant, a , of UO_2 (see Chapter 4, Eq. 4.2). From TEM analyses, the lattice parameter for the PSF-R sample is found to be 5.485 Å, which is determined with an accuracy of 1%. The lattice parameter measured from TEM for the high burnup of 65 MWd/kgU fuel is in good agreement with the result evaluated from μXRD experiment discussed in Chapter 4. The value of the UO_2 lattice constant for PSF-C sample (local burnup about 40 MWd/kgU) obtained by lattice fringe analysis of TEM images (not shown) also agrees with the result of XRD analysis of this sample.

9.3 Summary

The object of the study was to characterize fission gas bubbles in spent UO_2 fuels. Detailed TEM investigations have been performed on the changes in the number density as well as size distribution of rare gas bubbles with burnup by analyzing two probe samples, PSF-C (burnup 40 MWd/kgU) and PSF-R (burnup 65 MWd/kgU), with an emphasis on the bubble evolution in the uranium dioxide microstructure. Additional results presented are the crystallographic lattice constant data of UO_2 , measured from experimental TEM images. A heterogeneous population of gas bubbles with a broad bubble size distribution has been observed in the analyzed specimens. In the PSF-C specimen, small isolated bubbles in nano-scale (in the range of 2-4 nm) as well as bubbles of larger size ranging from 30-100 nm were visible under the TEM observations. Large bubbles are often found in contact with large precipitates of the metallic fission products. The high burnup of 65 MWd/kgU fuel is characterized by ultra-fine grained UO_2 microstructures, and a high density population of nano-size bubbles in the grain interior as well as gas bubbles lying along grain boundaries were observed in the TEM specimen. Utilizing the limited amount of TEM data obtained in this study, an attempt was made to quantify average bubble size and number density of intragranular fission gas bubbles observed in the PSF-R sample. The lattice parameters of irradiated UO_2 for PSF-C and PSF-R samples obtained from TEM measurements complement micro-beam XRD results. It is noteworthy to mention that the scope of work in this thesis to

investigate fission gas bubble size distributions in spent fuels has been limited, and thus, the TEM results presented here are preliminary. Additional work using TEM needs to be done in this area to obtain a better counting statistics of bubble populations and an accurate representation of the gas content in high burnup nuclear fuels.

10 Summary and Conclusions

The safety and in-reactor performance of UO_2 fuel are closely related to its microstructural characteristics. To predict in-pile fuel behaviors on a macroscopic scale and aid the fuel performance simulation efforts that seek to model distinct activities, experimental studies revealing an atomic-scale microstructure evolution and fission products behavior in irradiated fuels are of crucial importance. In the irradiated state, the modified UO_2 microstructure is apparently the combined result of irradiation defects, incorporated fission products, formation of fission gas bubbles, reorganization of extended defects such as dislocations, grains subdivision also called *fuel polygonization*, and finally, grain recrystallization. Needless to mention that the standard form of UO_2 , having an average grain size $\sim 10\text{ }\mu\text{m}$ (as fabricated), is the most common nuclear fuel material. Besides standard grain size UO_2 , advanced nuclear fuel, such as chromia-doped UO_2 (as-fabricated average grain size $\geq 50\text{ }\mu\text{m}$) gained importance during the last two decades, and already commercialized in the nuclear industry. The larger grains microstructures in DF can promote reduced fuel swelling during irradiation and facilitate the retention of fission gases within the irradiated fuel pellets. In addition, the DF has been proposed over recent years as candidate accident-tolerant fuel, in combination with suitable cladding that meets the accident tolerance criteria, for LWR fuel applications. According to the reviewed literature, experimental studies and routine PIE work had been performed investigating various aspects of microstructure evolution in standard UO_2 spent fuels. However, there are no published studies providing important microstructural insights of structural evolution in irradiated DFs, especially for high burnup fuels.

This doctoral thesis reports experimental investigations on irradiation induced microstructure evolution in high burnup DFs considering the role of dopant Cr and chemical effect of fission product elements by X-ray analyses, and a comparison of the results of DFs with those observed for the standard UO_2 materials. To clarify the crystallographic aspect of irradiation induced microstructure development in high burnup fuels and associated HBS initiation, additional spectroscopic experiments have been performed for an evaluation of atomic-scale uranium and plutonium environment in intermediated burnup UO_2 . Within the scope of this thesis work, a preliminary spectroscopic study has been conducted to investigate the Cr oxidation state in high burnup DF. The ultimate aim of these studies is to gain an in-depth understanding of irradiation induced structural development in the spent fuels, and determination of the relative prosperity of doped and standard UO_2 at a given burnup when irradiated under

the identical in-reactor operating conditions. All fuel materials, analyzed in this study, were procured from commercial nuclear reactors in Switzerland and samples were examined using synchrotron-based X-ray microprobe techniques. The main experimental findings and results interpretation are discussed in the preceding chapters. The conclusions from individual chapter results are summarized here, along with a set of recommendations for future research.

10.1 Conclusions

A summary of the main results and their interpretation is as follows:

- Synchrotron XRD reveals strong evidence that the UO_2 lattice is disturbed after irradiation, and micro-scanning XRD provides a clear picture of the evolution of lattice distortions in the spent nuclear fuels. The lattice dilation of irradiated uranium dioxide crystals has been observed for both undoped and doped materials. The change in lattice parameter increases with increasing burnup up to a local burnup threshold, after which the lattice constant decreases slightly with the burnup increment. And more important, the lattice constant dependency on burnup for undoped and doped UO_2 follow a similar trend. Supported by both qualitative and quantitative analyses considering various factors that influence the unit cell dimension of irradiated UO_2 crystals, the findings of this study suggest that accumulated lattice defects prevail and cause the observed expansion of the crystalline UO_2 lattice in spent fuels.
- High spatial resolution micro-beam XRD mapping measurements have been performed to quantitatively evaluate the microscale lattice strain distribution within UO_2 crystallites in spent fuel samples. The lattice deformation in the irradiated UO_2 polycrystals is tensile in nature. The experiments reveal that the UO_2 lattice strain is locally heterogeneous at the microscale, though the distribution of strain in the chosen mapping region is nearly similar for Cr-free standard UO_2 and Cr-doped UO_2 spent fuels. For fuels with comparable burnup levels, the lattice strain accumulated on the selected (311) crystal planes of the UO_2 fluorite lattice are comparable for non-doped and doped UO_2 . In relation to the microscopic strain development in irradiated UO_2 , it is an important performance parameter for its influence on the overall macroscopic stability and in-pile creep behavior of UO_2 pellets in the fuel rods during reactor operations. Quantitative investigation of lattice strains in high burnup UO_2 fuel is not straightforward, and this is made possible in the present study.
- The unique advantage of micro-beam Laue diffraction has been utilized to quantitatively characterize the dislocation evolution with burnup for standard UO_2 and chromia-doped UO_2 fuels. For the first time, the assessment of GND density in spent nuclear fuel has been made using non-destructive μXRD

measurements of the UO_2 lattice curvature for the most active $\frac{1}{2}\langle 110 \rangle\{110\}$ slip systems relating to the slip directions during deformation via dislocation gliding. As a comparative result, it is found that the variation of GND density with burnup in UO_2 follows a similar trend for non-doped and doped fuels when irradiated under comparable conditions. Given the several assumptions that were required for the analysis, the obtained results provide a quantitative trend on dislocation densities in spent UO_2 fuels of different burnups. This study provides experimental results for the validation of dislocation-based simulation codes to better understand the irradiation-induced defect structures of UO_2 at high burnup with defect dependent properties.

- The valence state of the dopant chromium in fresh and irradiated DF has been measured by micro-beam XANES spectroscopy. Solute Cr atoms, located in the UO_2 grains of the fresh fuel specimen, are found to be in the trivalent state. Traces of undissolved chromia particles in the fresh fuel were also seen in other areas of the specimen, which was mapped with EPMA and micro-beam XRF spectroscopy. EPMA has revealed that the distribution of Cr in the irradiated DF matrix is heterogeneous, and chromium precipitation at the grain boundaries is observed. Another relevant EPMA observation is the apparent correlation of the dopant Cr with metallic FPs, such as Mo, Ru, Tc, *etc.*, wherein the Cr appears to be surrounding the metallic FPs. Preliminary XANES experiments, performed at a selected region on the irradiated specimen, indicate that the oxidation state of Cr is reduced from Cr(III) (*i.e.*, in fresh fuel) to lower and mixed valence states. The spectral shape of the Cr K-edge XANES reflects the presence of different Cr-bearing species, and provides an indication that a fraction of chromium is reduced to the metallic state. An important finding of this study is that there is no hexavalent Cr(VI) (the most toxic form of chromium bearing compounds) detected in any of the fuel samples.
- EXAFS spectroscopy has been used to evaluate the chemical state and local atomic structure of uranium and plutonium. The formal oxidation state of uranium is found to be 4+ for both non-irradiated and irradiated fuels implying that uranium mainly exists in the tetravalent state in both fuels, and irradiation does not alter the uranium valence state. The actinide element plutonium forms fluorite solid solutions with UO_2 inside the irradiated pellet, and the Pu L_3 -edge XANES clearly shows that Pu is tetravalent. A highly successful micro-beam XAS measurement has made it possible to determine quantitative structural parameters on atomic scale for the first-nearest neighbor of U–O and Pu–O interactions in high burnup spent fuel.
- Preliminary TEM analyses have been carried out for quantitative determinations of fission gas bubble densities and size distributions in a selection of spent fuels. A heterogeneous population of intragranular gas bubbles with a broad bubble

size distribution has been observed in the analyzed specimens. The observed size and number density of gas bubbles at several different regions of the examined TEM foils are dependent on the local fuel burnup as well as the temperature experienced by the fuel. The coexistence of gas bubbles with metallic fission product precipitates, growth of fission gas bubbles at the grain boundaries and the refined grain-area in high burnup fuel are also observed in the TEM specimens. The lattice parameters of irradiated UO_2 have been measured from high resolution TEM images, and the results are in good agreement with those obtained from XRD measurements.

As known, standard UO_2 is conventional LWR fuel, chromia-doped UO_2 has also been used in commercial reactors over the past years. In addition, Cr-doped UO_2 is one of the potential candidates to fulfill the accident tolerant fuel applications in combination with suitable cladding materials that meet all requirements under accident conditions. The work presented in this thesis points out a number of important findings from synchrotron-based X-ray experiments and provides a comprehensive and comparative overview of the structural changes in high burnup UO_2 crystallites. New findings clearly show that irradiation has almost the same effect for standard and doped UO_2 fuels: A valuable information that allows further burnup extension of the DF as the accident tolerant fuel option for this material. The revealed structural changes on the atomic-scale and the interpretation of experimental results in this thesis work can be directly transferred to theory formulation applicable to model LWR fuel performance connecting computational approaches at each length scale from the atomic scale up to the macroscopic scale.

10.2 Outlook

This thesis contains new and potentially promising results corresponding to the irradiation-induced atomic scale modifications of doped and undoped nuclear fuels. While it is successful in clarifying many points, there is a scope to address many open questions. The recommendations and suggestions for possible future experimental work are listed as follows:

- In relation to the results presented in Chapter 4, the lattice parameter evolution and the effect of the dissolved FPs were investigated for both the fuel types. However, due to experimental limitations, it was not possible to measure the concentration of all FPs by EPMA analysis. To improve the obtained results, more thorough EPMA analyses on the same samples could be undertaken.
- In Chapter 6, the results of dislocation content in high burnup irradiated fuels are presented. In this regard, a comprehensive TEM work would be beneficial to

study the dislocation networks, specifically in the high burnup range since experimental literature data is missing at burnup values > 70 MWd/kgU.

- The chemical state of the dopant Cr in doped fuels is reported in Chapter 7. However, due to experimental constraints and limited synchrotron beamtime opportunities, it has not been possible to carry out the chemical speciation of Cr by EXAFS in spent doped fuels covering a wide burnup range. This is an important research topic that can be undertaken in the future.
- With regard to the Pu speciation results given in Chapter 8, an important future experiment would be to use an energy dispersive multi-elements XRF detector and/or a wavelength dispersive spectrometer in the experimental setup for Pu L₃-edge XAS measurements in order to obtain more reliable quantitative analysis of the local structure around the plutonium in spent fuels.
- Chapter 10 presents preliminary results obtained from fission gas bubble analysis using TEM. Though preparing ultra-thin TEM lamellae from irradiated fuel samples pose a challenge, it was a starting step to address an important research topic of fission gas distribution and its dependence on burnup. Not much information could be uncovered during the timeframe of this thesis work. Hence, further TEM investigations are recommended and put in relation with synchrotron results to understand the mechanism of fission gas distribution at the grain boundaries, the number and size density evolution as well as the pressures of the gas bubbles as a function of burnup, *etc.*

A Appendix

Batch Processing using XRDUA

XRDUA software is used to process and analyze the XRD data. To begin with, the first step of the analysis consists of loading a diffraction pattern (.tiff file) recorded from a CCD camera.

A.1 General calibration routine for μ XRD experiment with XRDUA

The experimental setup was first calibrated with a known standard specimen to obtain specific detector geometry as well as orientation, standard error relating to the experimental setup, and other global parameters for accurate determination of all XRD peak positions of UO_2 fuel samples. This analysis was accomplished in the XRDUA program, using the “Options → Experimental geometry” tab. In this case, initial guess values for the required parameters were used as inputs. Finally, the sample to detector distance, the rotation and tilt angles and the beam position were the parameters refined, because the wavelength (or the energy of incident X-rays), as well as the X (horizontal pixel size of the CCD camera) and Y (vertical pixel size of the CCD camera) parameters were known. The calibration analysis was performed using the XRD data measured from a reference Al_2O_3 powder sample.

A CCD image of the Al_2O_3 sample was uploaded through “File → Read 2D pattern”. A dark image for background subtraction was uploaded through the lateral tab “Background → Load Dark Image”, then by clicking on “Subtract background”, the final CCD image of the Al_2O_3 sample was prepared for further analysis (as shown in Fig. A.1). In the “Experimental geometry” window, the wavelength, energy and pixel sizes were held fixed. Then, initial guess values for the sample to detector distance, d , and the beam center position were inserted. Using the lateral “Beam position” tab, different methods were exploited to fit the beam center position on the CCD image.

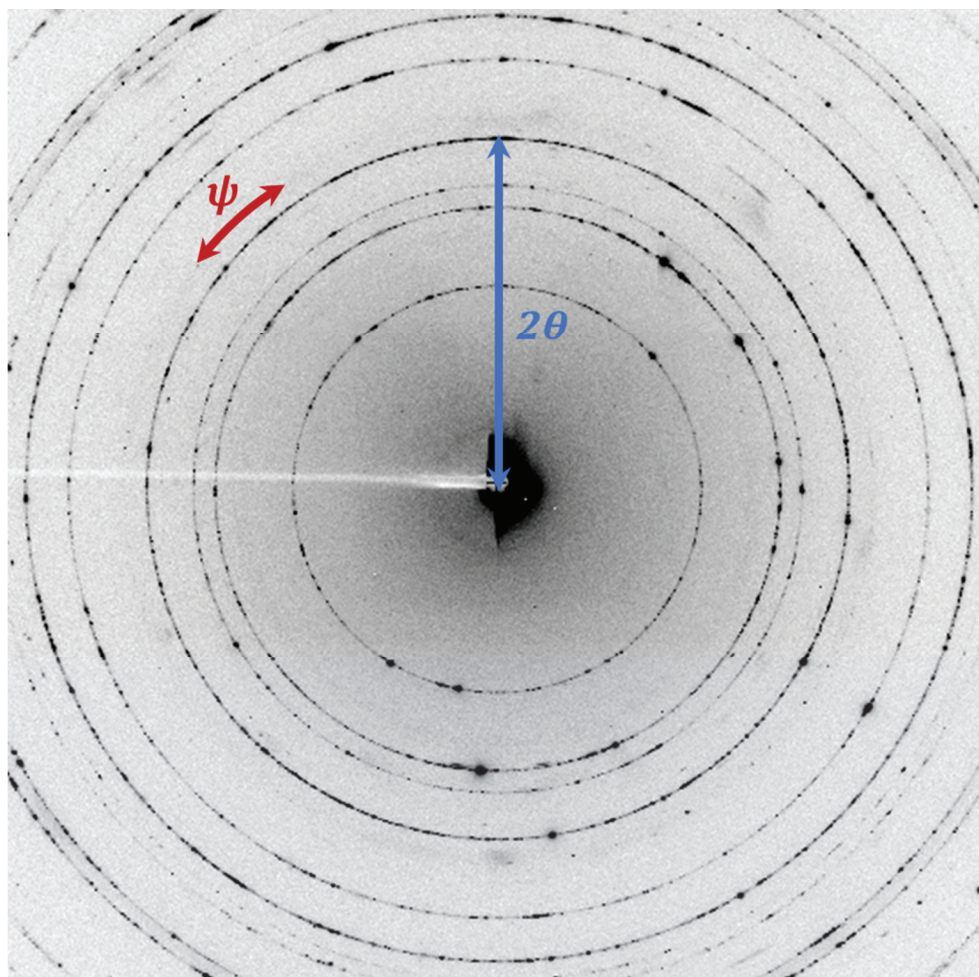


Figure A.1: An example of 2D XRD pattern acquired from Al_2O_3 powder sample. The radial and azimuthal directions are depicted.

The next step consists of loading a data file (.ciffile) containing structural information of the Al_2O_3 crystal. The required file has been downloaded from online XRD databases, followed by uploading in the XRDUA software through “File → Load → Load PDF”. Once the .ciffile is provided, the green circles representing the position of the Debye rings as extracted from the .ciffile, appear on the image and they are superimposed to the actual Debye rings of the 2D pattern. This result is shown in Fig. A.2. If this is not the case, it is then possible to modify the guessed experimental geometry parameters in order to obtain a good superimposition before starting the calibration process. Now, in the lateral tab “Calibration → Auto Set with PDF”, the software automatically sets the integration mask, also defined as ROI (region of interest), on the XRD pattern around the visible rings. Once all the preliminary steps have been completed, in the lateral tab “Calibration → Calibrate”, final calibration process has been performed following a stepwise procedure. In the “Calibration options” window, it is feasible to select suitable Debye rings and the number of standard deviations for appropriate outliers’ rejection. Since the parameter λ has to be considered as a fixed parameter, the “Refine Wavelength” option in the “Advanced” tab has been disabled. Once the calibration process has finished, the

software displays the outliers, fit plots, residuals and estimated experimental error for each data point of the d -spacing distribution created from XRD data of reference Al_2O_3 sample.

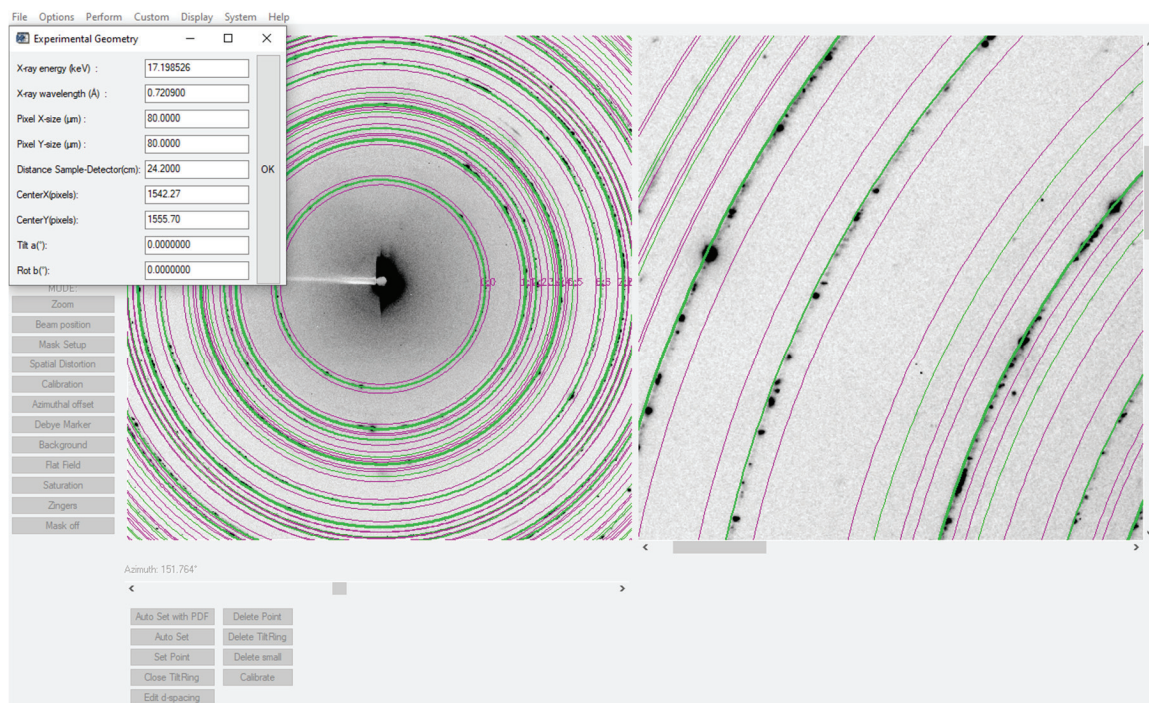


Figure A.2: Calibration of experimental setup using the 2D XRD pattern of Al_2O_3 ; rings from data file (.cifgreen) and auto set ROI (purple).

During the first calibration trial, all the Debye rings were selected and the value in the standard deviations tab was set to default. Then, by looking at the fit and residual plots, only the Debye rings providing best results were selected for the second trial in the calibration process. In order to reject outliers from the Debye rings, the outlier criterion was adapted, where the number of standard deviation taken for a data point to be rejected was set to 2 in the final step. The outcome of a fit plot is reported in Fig. A.3, as an example, in which the red line represents the software fit after calibration. It should be noted that, in this case, the Debye ring did not appear as a true circle but slightly distorted circle because of some imperfectness in focusing the incident X-ray beam at the CCD-detector plane. The graphical representation in Fig. A.3 shows the radial versus azimuthal integration plot of XRD intensities in the CCD pixels, as obtained in the calibration process.

After completing the calibration process, all the output information has been saved in a mask file (.msk file) through “File → Save → Save Mask”. This is an important requirement for further application of this file, *i.e.*, the refined parameters can be uploaded any time later for XRD data analysis.

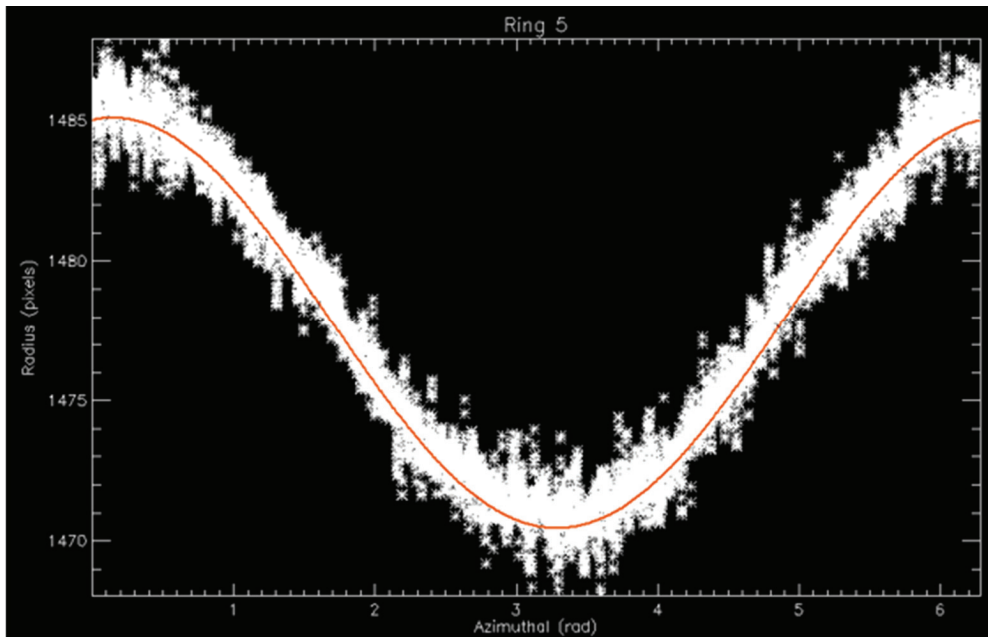


Figure A.3: Radial versus azimuthal integration plot of a selective Debye ring [number 5 corresponding to the (024) reflection of Al_2O_3] showing the measured intensity distributions in the CCD pixels and the fitted curve to generate a calibration curve.

A.2 Spectral analysis of fresh and irradiated UO_2 samples using XRDUA

In the first step, CCD-recorded Laue patterns of the investigated UO_2 fuel specimens were uploaded, followed by a dark image for background subtraction. A set of images from the whole dataset was selected and a sum of XRD patterns was created (“*Perform* → *Summate Patterns*”). In the same way, a number of CCD-recorded dark images were summed to create a corresponding dark-image file, which was used as the model file for background subtraction.

Before performing the integration, it is necessary to load the corresponding calibration mask file through “*File* → *Load* → *Load Mask*”. After selecting an appropriate ROI in the lateral tab “*Mask Setup*”, it is possible to proceed with the integration through “*Perform* → *Azimuthal Integration*” and save the output spectrum as a *.chi* file. In the 1D editor (“*Perform* → *Edit 1D Profile*”), a strip background subtraction has been performed (“*Background* → *Strip tab* → *Strip* → *Subtract*”).

At this point, it is necessary to mention that a normalization procedure was necessary. The centroid positions of the (111) peaks in the XRD data measured from the fuel samples were slightly adjusted to a fixed 2θ value, and the relative differences in 2θ positions of all the other higher index $\{hkl\}$ peaks were evaluated. In order to adjust the

position of the (111) peak, the parameter representing sample–detector distance in the “*Experimental Geometry*” window was slightly altered.

In the 1D editor of XRDUA, it is also possible to perform peak fitting and determine the centroid position. By clicking on the lateral “*Model*” tab, the pattern-modeling window is displayed with various options for modeling studies of XRD patterns. The first step consists of selecting the modeling type for the background in the “*Model*” window through the “*Background type*” tab. Then a group must be added to the chosen model by right clicking the corresponding folder and selecting “*Add*”. In the “*Main*” tab of the group window, it is possible to select the peak profile to be used for the fitting under “*Peak profile type*”. Before starting the refinement, it is necessary to add the peaks of interest from the raw spectrum through the “*Perform*” tab with either “*Add Peaks Manually*” or “*Add Peaks Automatically*”. In the “*Initial*” tab, the selected peaks are displayed with the initial guess position set by the software. Thereafter, it is possible to perform the fitting by clicking on “*Start refinement*” in the “*Model*” window. The results will be displayed in the “*Refined*” tab of the group window for each peak, and the resulting data can be saved under “*Perform → Save Peak Param*”.

Depending on the asymmetry of the XRD peak under consideration, either a Pseudo-Voigt curve or a Split Pseudo-Voigt curve fitting for peak profile was chosen.

A.3 Batch processing using XRDUA

In XRDUA, it is possible to perform a batch processing through “*Perform → Batch Processing*”, as available in the main window of the software. The first step consists of integrating XRD patterns to obtain the 1D spectra in the “*Explorative mode*”. In the “*File*” window, the directory containing the patterns, the integration mask and the output directory for batch processing data files must be inserted using the respective tabs. The integration mask should then be saved from an appropriate XRD pattern, and it must contain a ROI for subsequent integration and the refined parameters obtained during the calibration process.

In the “*Scan Dimensions*” window, after selecting the “*Map*” option, the start and stop positions with the total number of steps for horizontal and vertical detector movement must be inserted. If the movement directions of the scan are different from default, they must be changed as well. If all the values are inserted correctly, a preview of the map will appear on the batch processing window and the process can be started by clicking on “*Go*”. Once the process is over, in the output directory, an image file (.tiff format) is generated.

Now in the “*Full processing mode*”, a batch processing for the fitting of 1D spectra can be performed. In the “*File*” window, the directory containing the .tiff file must be inserted and the same file name must be specified in the first tab. The mask for the fitting

can be saved from the 1D editor through “*File → Save → Save Mask*” after performing the fitting on a reference spectrum, either from one of the processed XRD patterns or from an average pattern. The output of the “*Full processing mode*” is an *.xdi* file containing all the information about the fitted spectra.

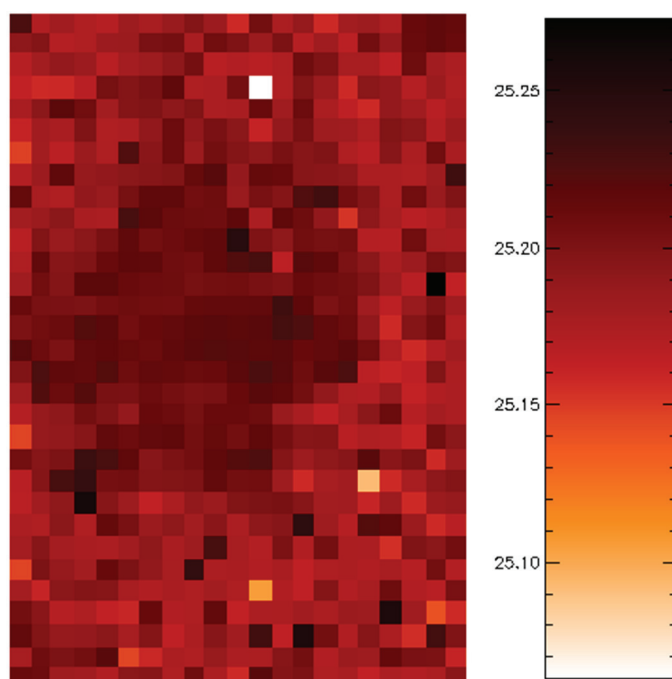


Figure A.4: An example of the 2θ distribution map of the (311) reflection, generated by analyzing the XRD data set in a batch mode, for the BDF-C particle.

In the XDI editor (“*Perform → Edit XDI files*”), the *.xdi* file can be loaded through “*File → Open XDI*” and the distribution maps are displayed while navigating in the “*Display Group*” tab. An example of distribution map retrieved by XRDUA batch processing is shown in A.4. In order to further elaborate the data contained in the distribution maps, the *.xdi* file can be converted into a data table, to be exported through “*File → Convert → XDI to PyMCA DAT*”.

Bibliography

- [1] *PRIS - Trend reports - Electricity Supplied* [Online].
Available: <https://pris.iaea.org/PRIS/WorldStatistics/WorldTrendinElectricalProduction.aspx>
- [2] *Energy – Facts and Figures* [Online].
Available: <https://www.eda.admin.ch/aboutswitzerland/en/home/wirtschaft/energie/energie---fakten-und-zahlen.html>
- [3] A. Kenich. *Atomistic simulation of fission products in zirconia polymorphs*. Ph.D. thesis, Imperial College London, 2019. doi: 10.25560/79395
- [4] *Nuclear Fuel Facts: Uranium* [Online].
Available: <https://www.energy.gov/ne/nuclear-fuel-facts-uranium>
- [5] K. Lassmann, C.T. Walker, J. van de Laar, and F. Lindström. *Modelling the high burnup UO₂ structure in LWR fuel*. J. Nucl. Mater. 226 (1995) 1-8.
doi: 10.1016/0022-3115(95)00116-6
- [6] J. Noirot, L. Desgranges, and J. Lamontagne. *Detailed characterisations of high burn-up structures in oxide fuels*. J. Nucl. Mater. 372 (2008) 318-339.
doi: 10.1016/j.jnucmat.2007.04.037
- [7] H. Xiao, C. Long, and H. Chen. *The formation mechanisms of high burnup structure in UO₂ fuel*. J. Nucl. Mater. 556 (2021) 153151.
doi: 10.1016/j.jnucmat.2021.153151
- [8] T. Sonoda, M. Kinoshita, I.L.F. Ray, T. Wiss, H. Thiele, D. Pellottiero, V.V. Rondinella, and H. Matzke. *Transmission electron microscopy observation on irradiation-induced microstructural evolution in high burn-up UO₂ disk fuel*. Nucl. Instrum. Methods Phys. Res. Sect. B Beam Interact. Mater. At. 191 (2002) 622-628. doi: 10.1016/S0168-583X(02)00622-5
- [9] V.V. Rondinella and T. Wiss. *The high burn-up structure in nuclear fuel*. Mater. Today 13 (2010) 24-32. doi: 10.1016/S1369-7021(10)70221-2
- [10] R. Manzel and C.T. Walker. *EPMA and SEM of fuel samples from PWR rods with an average burn-up of around 100 MWd/kgHM*. J. Nucl. Mater. 301 (2002) 170-182.
doi: 10.1016/S0022-3115(01)00753-X

- [11] J.P. Moore and D.L. Mcelroy. *Thermal Conductivity of Nearly Stoichiometric Single-Crystal and Polycrystalline UO₂*. J. Am. Ceram. Soc. 54 (1971) 40-46.
doi: 10.1111/j.1151-2916.1971.tb12164.x
- [12] B.J. Lewis, F.C. Iglesias, R.S. Dickson, and A. Williams. *Overview of high-temperature fuel behaviour with relevance to CANDU fuel*. J. Nucl. Mater. 394 (2009) 67-86. doi: 10.1016/j.jnucmat.2009.08.011
- [13] T. Wiss, V.V. Rondinella, R.J.M. Konings, D. Staicu, D. Papaioannou, S. Bremier, P. Pöml, O. Benes, J.-Y. Colle, P. Van Uffelen, A. Schubert, F. Cappia, M. Marchetti, D. Pizzocri, F. Jatuff, W. Goll, T. Sonoda, A. Sasahara, S. Kitajima, and M. Kinoshita. *Properties of the high burnup structure in nuclear light water reactor fuel*. Radiochim. Acta 105 (2017) 893-906. doi: 10.1515/ract-2017-2831
- [14] M. Lemes, A. Soba, and A. Denis. *An empirical formulation to describe the evolution of the high burnup structure*. J. Nucl. Mater. 456 (2015) 174-181.
doi: 10.1016/j.jnucmat.2014.09.048
- [15] T. Barani, D. Pizzocri, F. Cappia, L. Luzzi, G. Pastore, and P. Van Uffelen. *Modeling high burnup structure in oxide fuels for application to fuel performance codes. Part I: High burnup structure formation*. J. Nucl. Mater. 539 (2020) 152296.
doi: 10.1016/j.jnucmat.2020.152296
- [16] H.J. Matzke and M. Kinoshita. *Polygonization and high burnup structure in nuclear fuels*. J. Nucl. Mater. 247 (1997) 108-115.
doi: 10.1016/S0022-3115(97)00081-0
- [17] D. Pizzocri, F. Cappia, L. Luzzi, G. Pastore, V.V. Rondinella, and P. Van Uffelen. *A semi-empirical model for the formation and depletion of the high burnup structure in UO₂*. J. Nucl. Mater. 487 (2017) 23-29.
doi: 10.1016/j.jnucmat.2017.01.053
- [18] C.B. Lee and Y.H. Jung. *An attempt to explain the high burnup structure formation mechanism in UO₂ fuel*. J. Nucl. Mater. 279 (2000) 207-215.
doi: 10.1016/S0022-3115(00)00021-0
- [19] J. Arborelius, K. Backman, L. Hallstadius, M. Limbäck, J. Nilsson, B. Rebensdorff, G. Zhou, K. Kitano, R. Löfström, and G. Rönnerberg. *Advanced Doped UO₂ Pellets in LWR Applications*. J. Nucl. Sci. Technol. 43 (2006) 967-976.
doi: 10.1080/18811248.2006.9711184
- [20] L. Bourgeois, Ph. Dehaudt, C. Lemaignan, and A. Hammou. *Factors governing microstructure development of Cr₂O₃-doped UO₂ during sintering*. J. Nucl. Mater. 297 (2001) 313-326. doi: 10.1016/S0022-3115(01)00626-2
- [21] Ch. Riglet-Martial, Ph. Martin, D. Testemale, C. Sabathier-Devals, G. Carlot, P. Matheron, X. Iltis, U. Pasquet, C. Valot, C. Delafoy, and R. Largeton.

- Thermodynamics of chromium in UO₂ fuel: A solubility model.* J. Nucl. Mater. 447 (2014) 63-72. doi: 10.1016/j.jnucmat.2013.12.021
- [22] M.W. Owen, M.W.D. Cooper, M.J.D. Rushton, A. Claisse, W.E. Lee, and S.C. Middleburgh. *Diffusion in undoped and Cr-doped amorphous UO₂.* J. Nucl. Mater. 576 (2023) 154270. doi: 10.1016/j.jnucmat.2023.154270
- [23] M.W.D. Cooper, C.R. Stanek, and D.A. Andersson. *The role of dopant charge state on defect chemistry and grain growth of doped UO₂.* Acta Mater. 150 (2018) 403-413. doi: 10.1016/j.actamat.2018.02.020
- [24] M. Hong, B.P. Uberuaga, D.A. Andersson, C.R. Stanek, S.R. Phillpot, and S.B. Sinnott. *Role of electronic effects on the incorporation of Cr at a $\Sigma 5$ grain boundary in UO₂.* Comput. Mater. Sci. 78 (2013) 29-33. doi: 10.1016/j.commatsci.2013.05.008
- [25] S. Kashibe and K. Une. *Effect of additives (Cr₂O₃, Al₂O₃, SiO₂, MgO) on diffusional release of ¹³³Xe from UO₂ fuels.* J. Nucl. Mater. 254 (1998) 234-242. doi: 10.1016/S0022-3115(97)00356-5
- [26] Z. Guo, R. Ngayam-Happy, M. Krack, and A. Pautz. *Atomic-scale effects of chromium-doping on defect behaviour in uranium dioxide fuel.* J. Nucl. Mater. 488 (2017) 160-172. doi: 10.1016/j.jnucmat.2017.02.043
- [27] P. Van Uffelen, J. Hales, W. Li, G. Rossiter, and R. Williamson. *A review of fuel performance modelling.* J. Nucl. Mater. 516 (2019) 373-412. doi: 10.1016/j.jnucmat.2018.12.037
- [28] M.W.D. Cooper. *Ceramic nuclear fuel performance and the role of atomic scale simulations.* J. Nucl. Mater. 561 (2022) 153531. doi: 10.1016/j.jnucmat.2022.153531
- [29] B. Michel, M. Welland, N. Ofori-Opoku, L. Vanbrutzel, K. Kulacsy, M.R. Tonks, P.-G. Vincent, F. Ribeiro, A. Jelea, G. Pastore, D.A. Anderson, J.-m. Gatt, R. Madec, and J.-P. Crocombette. *State of the art of fuel micro-mechanical modelling: From atomic scale to engineering laws in fuel performance codes.* J. Nucl. Mater. 572 (2022) 154034. doi: 10.1016/j.jnucmat.2022.154034
- [30] C. Wen, D. Yun, X. He, Y. Xin, W. Li, and Z. Sun. *Applying multi-scale simulations to materials research of nuclear fuels: A review.* Materials Reports: Energy 1 (2021) 100048. doi: 10.1016/j.matre.2021.100048
- [31] L. Vimercati1, M.F. Gatti1, T. Gagliardi, F. Cuccaro, L. De Maria, A. Caputi, M. Quarato, and A. Baldassarre. *Environmental exposure to arsenic and chromium in an industrial area.* Environ. Sci. Pollut. Res. 24 (2017) 11528-11535. doi: 10.1007/s11356-017-8827-6
- [32] O. Roth and M. Jonsson. *Oxidation of UO₂(s) in aqueous solution.* Cent. Eur. J. Chem. 6 (2008) 1-14. doi: 10.2478/s11532-007-0067-z

- [33] D.R. Olander and D. Wongsawaeng. *Re-solution of fission gas – A review: Part I. Intragranular bubbles*. J. Nucl. Mater. 354 (2006) 94-109. doi: 10.1016/j.jnucmat.2006.03.010
- [34] F. Charollais, S. Fonquernie, C. Perrais, M. Perez, O. Dugne, F. Cellier, G. Harbonnier, and M.-P. Vitali. *CEA and AREVA R&D on HTR fuel fabrication and presentation of the CAPRI experimental manufacturing line*. Nucl. Eng. Des. 236 (2006) 534-542. doi: 10.1016/j.nucengdes.2005.11.022
- [35] D.N. Sah, U.K. Viswanathan, E. Ramadasan, K. Unnikrishnan, and S. Anantharaman. *Post irradiation examination of thermal reactor fuels*. J. Nucl. Mater. 383 (2008) 45-53. doi: 10.1016/j.jnucmat.2008.08.022
- [36] K. Suyama, H. Mochizuki, and T. Kiyosumi. *Revised Burnup Code System SWAT: Description and Validation Using Postirradiation Examination Data*. Nucl. Technol. 138 (2002) 97-110. doi: 10.13182/NT02-A3282
- [37] T. Yamamoto and M. Yamamoto. *Nuclear Analysis of PIE Data of Irradiated BWR 8×8-2 and 8×8-4 UO₂ Fuel Assemblies*. J. Nucl. Sci. Technol. 45 (2008) 1193-1214. doi: 10.1080/18811248.2008.9711908
- [38] W. Goll, P.B. Hoffmann, C. Hellwig, W. Sauser, J. Spino, and C.T. Walker. *UO₂ fuel behaviour at rod burn-ups up to 105 MWd/kgHM: A review of 10 years of high burn-up examinations commissioned by AREVA NP*. Atw Int. Z. Fuer Kernenergie. 52 (2007) 95-102.
- [39] J.J. Carbajo, G.L. Yoder, S.G. Popov, and V.K. Ivanov. *A review of the thermophysical properties of MOX and UO₂ fuels*. J. Nucl. Mater. 299 (2001) 181-198. doi: 10.1016/S0022-3115(01)00692-4
- [40] J.K. Fink. *Thermophysical properties of uranium dioxide*. J. Nucl. Mater. 279 (2000) 1-18. doi: 10.1016/S0022-3115(99)00273-1
- [41] P. Hofmann. *Current knowledge on core degradation phenomena, a review*. J. Nucl. Mater. 270 (1999) 194-211. doi: 10.1016/S0022-3115(98)00899-X
- [42] B.J. Lewis, R. Dickson, F.C. Iglesias, G. Ducros, and T. Kudo. *Overview of experimental programs on core melt progression and fission product release behaviour*. J. Nucl. Mater. 380 (2008) 126-143. doi: 10.1016/j.jnucmat.2008.07.005
- [43] D.R. Olander and P. Van Uffelen. *On the role of grain boundary diffusion in fission gas release*. J. Nucl. Mater. 288 (2001) 137-147. doi: 10.1016/S0022-3115(00)00725-X
- [44] H. Kleykamp. *The solubility of selected fission products in UO₂ and (U, Pu)O₂*. J. Nucl. Mater. 206 (1993) 82-86. doi: 10.1016/0022-3115(93)90236-R
- [45] R.W. Grimes and C.R.A. Catlow. *The stability of fission products in uranium dioxide*. Philos. Trans. R. Soc. Lond. Ser. Phys. Eng. Sci. 335 (1991) 609-634. doi: 10.1098/rsta.1991.0062

- [46] L.W. Hobbs. *Topology and geometry in the irradiation-induced amorphization of insulators*. Nucl. Instrum. Methods Phys. Res. Sect. B Beam Interact. Mater. At. 91 (1994) 30-42. doi: 10.1016/0168-583X(94)96187-5
- [47] K.E. Sickafus, L. Minervini, R.W. Grimes, J.A. Valdez, M. Ishimaru, F. Li, K.J. McClellan, and T. Hartmann. *Radiation Tolerance of Complex Oxides*. Science 289 (2000) 748-751. doi: 10.1126/science.289.5480.748
- [48] L.F. He, B. Valderrama, A.-R. Hassan, J. Yu, M. Gupta, J. Pakarinen, H.B. Henderson, J. Gan, M.A. Kirk, A.T. Nelson, M.V. Manuel, A. El-Azab, and T.R. Allen. *Bubble formation and Kr distribution in Kr-irradiated UO₂*. J. Nucl. Mater. 456 (2015) 125-132. doi: 10.1016/j.jnucmat.2014.09.026
- [49] P.M. Martin, E. Vathonne, G. Carlot, R. Delorme, C. Sabathier, M. Freyss, P. Garcia, M. Bertolus, P. Glatzel, and O. Proux. *Behavior of fission gases in nuclear fuel: XAS characterization of Kr in UO₂*. J. Nucl. Mater. 466 (2015) 379-392. doi: 10.1016/j.jnucmat.2015.08.019
- [50] F. Garrido, L. Vincent, L. Nowicki, G. Sattonnay, and L. Thom  . *Radiation stability of fluorite-type nuclear oxides*. Nucl. Instrum. Methods Phys. Res. Sect. B Beam Interact. Mater. At. 266 (2008) 2842-2847. doi: 10.1016/j.nimb.2008.03.128
- [51] H. Labrim, M.-F. Barthe, P. Desgardin, T. Sauvage, G. Blondiaux, C. Corbel, and J.P. Piron. *Vacancy defects induced in sintered polished UO₂ disks by helium implantation*. Appl. Surf. Sci. 252 (2006) 3256-3261. doi: 10.1016/j.apsusc.2005.08.045
- [52] W.H. Hocking, R.A. Verrall, and I.J. Muir. *Migration behaviour of iodine in nuclear fuel*. J. Nucl. Mater. 294 (2001) 45-52. doi: 10.1016/S0022-3115(01)00447-0
- [53] HJ. Matzke, P.G. Lucuta, and T. Wiss. *Swift heavy ion and fission damage effects in UO₂*. Nucl. Instrum. Methods Phys. Res. Sect. B Beam Interact. Mater. At. 166-167 (2000) 920-926. doi: 10.1016/S0168-583X(99)00801-0
- [54] HJ. Matzke and A. Turos. *Ion implantation studies of UO₂ and UN*. J. Nucl. Mater. 188 (1992) 285-292. doi: 10.1016/0022-3115(92)90486-5
- [55] M. Kato, A. Komeno, H. Uno, H. Sugata, N. Nakae, K. Konashi, and M. Kashimura. *Self-radiation damage in plutonium and uranium mixed dioxide*. J. Nucl. Mater. 393 (2009) 134-140. doi: 10.1016/j.jnucmat.2009.05.020
- [56] L. Van Brutzel and M. Rarivomanantsoa. *Molecular dynamics simulation study of primary damage in UO₂ produced by cascade overlaps*. J. Nucl. Mater. 358 (2006) 209-216. doi: 10.1016/j.jnucmat.2006.07.009
- [57] M. Abramowski. *Atomistic simulations of the uranium/oxygen system [Nuclear fuels]*. Ph.D. thesis, University of London (United Kingdom), 2001.

- [58] A. Romano, C.A. Shuffler, H.D. Garkisch, D.R. Olander, and N.E. Todreas. *Fuel performance analysis for PWR cores*. Nucl. Eng. Des. 239 (2009) 1481-1488. doi: 10.1016/j.nucengdes.2008.11.022
- [59] M. Stan. *Multi-scale models and simulations of nuclear fuels*. Nucl. Eng. Technol. 41 (2009) 39-52. doi: 10.5516/NET.2009.41.1.039
- [60] J.D. Hales, S.R. Novascone, B.W. Spencer, R.L. Williamson, G. Pastore, and D.M. Perez. *Verification of the BISON fuel performance code*. Ann. Nucl. Energy 71 (2014) 81-90. doi: 10.1016/j.anucene.2014.03.027
- [61] H.S. Aybar and P. Ortego. *A review of nuclear fuel performance codes*. Prog. Nucl. Energy 46 (2005) 127-141. doi: 10.1016/j.pnucene.2005.01.004
- [62] B.-H. Lee, Y.-H. Koo, J.-Y. Oh, J.-S. Cheon, Y.-W. Tahk, and D.-S. Sohn. *Fuel performance code COSMOS for analysis of LWR UO₂ and MOX fuel*. Nucl. Eng. Technol. 43 (2011) 499-508. doi: 10.5516/NET.2011.43.6.499
- [63] D. Bathellier, M. Lainet, M. Freyss, P. Olsson, and E. Bourasseau. *A new heat capacity law for UO₂, PuO₂ and (U,Pu)O₂ derived from molecular dynamics simulations and useable in fuel performance codes*. J. Nucl. Mater. 549 (2021) 152877. doi: 10.1016/j.jnucmat.2021.152877
- [64] M.W.D. Cooper, G. Pastore, Y. Che, C. Matthews, A. Forslund, C.R. Stanek, K. Shirvan, T. Tverberg, K.A. Gamble, B. Mays, D.A. Andersson. *Fission gas diffusion and release for Cr₂O₃-doped UO₂: From the atomic to the engineering scale*. J. Nucl. Mater. 545 (2021) 152590. doi: 10.1016/j.jnucmat.2020.152590 ; and references therein.
- [65] Y. Harada and S. Doi. *Irradiation behavior of large grain UO₂ fuel rod by active powder*. J. Nucl. Sci. Technol. 35 (1998) 411-418. doi: 10.1080/18811248.1998.9733883
- [66] H. Assmann, W. Dörr, G. Gradel, G. Maier, and M. Peehs. *Doping UO₂ with niobia – Beneficial or not?*. J. Nucl. Mater. 98 (1981) 216-220. doi: 10.1016/0022-3115(81)90401-3
- [67] K.-W. Song, Y.H. Jeong, K.S. Kim, J.G. Bang, T.H. Chun, H.K. Kim, and K.N. Song. *High burnup fuel technology in Korea*. Nucl. Eng. Technol. 40 (2008) 21-36. doi: 10.5516/NET.2008.40.1.021
- [68] A. Leenaers, L.de Tollenaere, C. Delafoy, and S. Van den Berghe. *On the solubility of chromium sesquioxide in uranium dioxide fuel*. J. Nucl. Mater. 317 (2003) 62-68. doi: 10.1016/S0022-3115(02)01693-8
- [69] C. Delafoy, P. Dewes, and T. Miles. *Areva NP Cr₂O₃-doped fuel development for BWRs*. Proceedings of LWR Fuel Performance/TopFuel San Francisco, CA, USA (2007).

- [70] J.H. Yang, K.S. Kim, I.H. Nam, J.S. Oh, D.-J. Kim, Y.W. Rhee, and J.H. Kim. *Effect of step wise variation of oxygen potential during the isothermal sintering on the grain growth behavior in Cr₂O₃ doped UO₂ pellets*. J. Nucl. Mater. 429 (2012) 25-33. doi: 10.1016/j.jnucmat.2012.05.034
- [71] M. Sun, J. Stackhouse, and P.M. Kowalski. *The +2 oxidation state of Cr incorporated into the crystal lattice of UO₂*. Commun. Mater. 1:13 (2020) 1-8. doi: 10.1038/s43246-020-0014-5
- [72] P. Kegler, M. Klinkenberg, A. Bukaemskiy, G.L. Murphy, G. Deissmann, F. Brandt, and D. Bosbach. *Chromium doped UO₂-based ceramics: Synthesis and characterization of model materials for modern nuclear fuels*. Materials 14 (2021) 6160. doi: 10.3390/ma14206160
- [73] A.R. Massih and L.O. Jernkvist. *Effects of additives on UO₂ fuel behavior: Expanded edition*. Report number: 2021:20. Available: <https://www.ssm.se>
- [74] A. Milena-Pérez, L.J. Bonales, N. Rodríguez-Villagra, S. Fernández, V.G. Baonza, and J. Cobos. *Raman spectroscopy coupled to principal component analysis for studying UO₂ nuclear fuels with different grain sizes due to the chromia addition*. J. Nucl. Mater. 543 (2021) 152581. doi: 10.1016/j.jnucmat.2020.152581
- [75] H. Smith, L.T. Townsend, R. Mohun, T. Cordara, M.C. Stennett, J.F.W. Mosselmans, K. Kvashnina, and C.L. Corkhill. *Cr²⁺ solid solution in UO₂ evidenced by advanced spectroscopy*. Commun. Chem. 5:163 (2022) 1-8. doi: 10.1038/s42004-022-00784-3
- [76] G.L. Murphy, R. Gericke, S. Gilson, E.F. Bazarkina, A. Rossberg, P. Kaden, R. Thümmeler, M. Klinkenberg, M. Henkes, P. Kegler, V. Svitlyk, J. Marquardt, T. Lender, C. Hennig, K.O. Kvashnina, and N. Huittinen. *Deconvoluting Cr states in Cr-doped UO₂ nuclear fuels via bulk and single crystal spectroscopic studies*. Nat. Commun. 14:2455 (2023) 1-11. doi: 10.1038/s41467-023-38109-0
- [77] H. Smith, T. Cordara, C. Gausse, S.E. Pepper, and C.L. Corkhill. *Oxidative dissolution of Cr-doped UO₂ nuclear fuel*. npj Mater. Degrad. 7:25 (2023) 1-11. doi: 10.1038/s41529-023-00347-4
- [78] C. Delafoy, P. Blanpain, C. Maury, P. Dehaut, C. Nonon, and S. Valin. *Advanced UO₂ fuel with improved PCI resistance and fission gas retention capability*. Proceedings of TopFuel 2003, Würzburg, Germany (2003).
- [79] S. Valin *et al.* *Synthesis of the advanced UO₂ microstructures program in the TANOX device*. Proceedings of International Atomic Energy Agency (IAEA) Technical Committee Meeting, Brussels, Belgium (2003) 1011-4289.

- [80] A.P. Hammersley, S.O. Svensson, and A. Thompson. *Calibration and correction of spatial distortions in 2D detector systems*. Nucl. Instrum. Methods Phys. Res. Sect. Accel. Spectrometers Detect. Assoc. Equip. 346 (1994) 312-321.
doi: 10.1016/0168-9002(94)90720-X
- [81] W.De Nolf and K. Janssens. *Micro X-ray diffraction and fluorescence tomography for the study of multilayered automotive paints*. Surf. Interface Anal. 42 (2010) 411-418. doi: 10.1002/sia.3125
- [82] *Match! – Phase Analysis using Powder Diffraction* [Online].
Available: <http://www.crystalimpact.com/match/>
- [83] C. Mieszczyński, G. Kuri, C. Degueldre, M. Martin, J. Bertsch, C.N. Borca, D. Grolimund, C. Delafoy, and E. Simoni. *Irradiation effects and micro-structural changes in large grain uranium dioxide fuel investigated by micro-beam X-ray diffraction*. J. Nucl. Mater. 444 (2014) 274-282.
doi: 10.1016/j.jnucmat.2013.09.054
- [84] C. Mieszczyński, C. Degueldre, G. Kuri, J. Bertsch, and C.N. Borca. *Investigation of irradiated uranium-plutonium mixed oxide fuel by synchrotron based micro X-ray diffraction*. Prog. Nucl. Energy 57 (2012) 130-137.
doi: 10.1016/j.pnucene.2011.11.012
- [85] G. Kuri, M. Martin, and J. Bertsch. *Microbeam X-ray diffraction to study radiation damage in irradiated uranium dioxide nuclear fuel*. Proceedings of 2014 water reactor fuel performance meeting, top fuel, LWR fuel performance meeting (WRFPM 2014), Sendai, Japan (2014) 100043.
- [86] B. Ravel and M. Newville. *ATHENA, ARTEMIS, HEPHAESTUS: Data analysis for X-ray absorption spectroscopy using IFEFFIT*. J. Synchrotron Rad. 12 (2005) 537-541.
doi: 10.1107/S0909049505012719
- [87] E.A. Stern, B.A. Bunker, and S.M. Heald. *Many-body effects on extended x-ray absorption fine structure amplitudes*. Phys. Rev. B 21 (1980) 5521-5539.
doi: 10.1103/PhysRevB.21.5521
- [88] M. Newville. *IFEFFIT: interactive XAFS analysis and FEFF fitting*. J. Synchrotron Rad. 8 (2001) 322-324. doi: 10.1107/S0909049500016964
- [89] W. Friedrich, P. Knipping, and M. von Laue. *Interferenz-Erscheinungen bei Röntgenstrahlen*. Proceedings of Verlag der Königlich Bayerischen Akademie der Wissenschaften, München, Germany (1912) 303-322.
- [90] L. de Broglie. *Recherches sur la théorie des quanta*. Ph.D. thesis, Université de Paris, 1924. doi: 10.1051/anphys/192510030022
- [91] M. Newville. *Fundamentals of XAFS*. Rev. Mineral. Geochem. 78 (2014) 33-74.
doi: 10.2138/rmg.2014.78.2

- [92] S.D. Conradson and J.A. Schecker. *XAFS- A Technique to Probe Local Structure*. Los Alamos Science 26 (2000) 422-435.
- [93] D.E. Sayers, E.A. Stern, and F.W. Lytle. *New technique for investigating noncrystalline structures: Fourier analysis of the Extended X-Ray Absorption Fine Structure*. Phys. Rev. Lett. 27 (1971) 1204-1207. doi: 10.1103/PhysRevLett.27.1204
- [94] D.C. Koningsberger, B.L. Mojet, G.E. van Dorssen, and D.E. Ramaker. *XAFS spectroscopy: fundamental principles and data analysis*. Top. Catal. 10 (2000) 143-155. doi: 10.1023/A:1019105310221
- [95] E.A. Stern, M. Newville, B. Ravel, Y. Yacoby, and D. Haskel. *The UWXAFS analysis package: philosophy and details*. Phys. B Condens. Matter 208-209 (1995) 117-120. doi: 10.1016/0921-4526(94)00826-H
- [96] T. Ikonen and V. Tulkki. *The importance of input interactions in the uncertainty and sensitivity analysis of nuclear fuel behavior*. Nucl. Eng. Des. 275 (2014) 229-241. doi: 10.1016/j.nucengdes.2014.05.015
- [97] J.S. Kim, Y.S. Jeon, S.D. Park, S.H. Han, and J.G. Kim. *Burnup determination of high burnup and dry processed fuels based on isotope dilution mass spectrometric measurements*. J. Nucl. Sci. Technol. 44 (2007) 1015-1023. doi: 10.1080/18811248.2007.9711341
- [98] J.S. Kim, Y.S. Jeon, S.D. Park, Y.-K. Ha, and K. Song. *Analysis of high burnup pressurized water reactor fuel using uranium, plutonium, neodymium, and cesium isotope correlations with burnup*. Nucl. Eng. Technol. 47 (2015) 924-933. doi: 10.1016/j.net.2015.08.002
- [99] K. Nogita and K. Une. *Thermal recovery of radiation defects and microstructural change in irradiated UO₂ fuels*. J. Nucl. Sci. Technol. 30 (1993) 900-910. doi: 10.1080/18811248.1993.9734564
- [100] V. Brankov, G. Khvostov, K. Mikityuk, A. Pautz, R. Restani, S. Abolhassani, G. Ledergerber, and W. Wiesenack. *Analysis of effects of pellet-cladding bonding on trapping of the released fission gases in high burnup KKL BWR fuels*. Nucl. Eng. Des. 305 (2016) 559-568. doi: 10.1016/j.nucengdes.2016.06.021
- [101] G. Kuri, H. Ramanantoanina, S. Bhattacharya, J. Bertsch, and M. Martin. *Insights into the interfacial speciation of Ni in the corrosion layer of high burnup Zircaloy-2 cladding: A combined XRD, XAS, and LFDFE study*. Corros. Sci. 215 (2023) 111024. doi: 10.1016/j.corsci.2023.111024
- [102] C. Mieszczyński, G. Kuri, J. Bertsch, M. Martin, C.N. Borca, C. Delafoy, and E. Simoni. *Microbeam x-ray absorption spectroscopy study of chromium in large-grain uranium dioxide fuel*. J. Phys. Condens. Matter 26 (2014) 355009. doi: 10.1088/0953-8984/26/35/355009

- [103] T. Cardinaels, K. Govers, B. Vos, S. Van den Berghe, M. Verwerft, L. de Tollenaere, G. Maier, and C. Delafoy. *Chromia doped UO₂ fuel: Investigation of the lattice parameter*. J. Nucl. Mater. 424 (2012) 252-260. doi: 10.1016/j.jnucmat.2012.02.025
- [104] M. Szuta. *Total surface area change of Uranium dioxide fuel in function of burn-up and its impact on fission gas release during neutron irradiation for small, intermediate and high burn-up*. Proceedings of Ninth International Conference on WWER Fuel Performance, Modelling and Experimental Support, Bulgaria (2011).
- [105] J. Spino and D. Papaioannou. *Lattice parameter changes associated with the rim-structure formation in high burn-up UO₂ fuels by micro X-ray diffraction*. J. Nucl. Mater. 281 (2000) 146-162. doi: 10.1016/S0022-3115(00)00236-1
- [106] M. Amaya, J. Nakamura, and T. Fuketa. *The effects of irradiation condition and microstructural change on lattice parameter, crystal lattice strain and crystallite size in high burnup UO₂ pellet*. J. Nucl. Mater. 392 (2009) 439-446. doi: 10.1016/j.jnucmat.2009.04.005
- [107] M. Amaya, J. Nakamura, T. Fuketa, and Y. Kosaka. *Relationship between changes in the crystal lattice strain and thermal conductivity of high burnup UO₂ pellets*. J. Nucl. Mater. 396 (2010) 32-42. doi: 10.1016/j.jnucmat.2009.10.049
- [108] L. Lynds, W.A. Young, J.S. Mohl, and G.G. Libowitz. *X-Ray and density study of nonstoichiometry in uranium oxides*. Advances in Chemistry 39 (1963) 58-65. doi: 10.1021/ba-1964-0039.ch005
- [109] J.M. Elorrieta, L.J. Bonales, N. Rodríguez-Villagra, V.G. Baonza, and J. Cobos. *A detailed Raman and X-ray study of UO_{2+x} oxides and related structure transitions*. Phys. Chem. Chem. Phys. 18 (2016) 28209-28216. doi: 10.1039/C6CP03800J
- [110] F. Bruneval, M. Freyss, and J.-P. Crocombette. *Lattice constant in nonstoichiometric uranium dioxide from first principles*. Phys. Rev. Mater. 2 (2018) 023801. doi: 10.1103/PhysRevMaterials.2.023801
- [111] H.J. Matzke. *Oxygen potential measurements in high burnup LWR UO₂ fuel*. J. Nucl. Mater. 223 (1995) 1-5. doi: 10.1016/0022-3115(95)00004-6
- [112] W.J. Weber. *Ingrowth of lattice defects in alpha irradiated UO₂ single crystals*. J. Nucl. Mater. 98 (1981) 206-215. doi: 10.1016/0022-3115(81)90400-1
- [113] W.J. Weber. *Alpha-irradiation damage in CeO₂, UO₂ and PuO₂*. Radiat. Eff. 83 (1984) 145-156. doi: 10.1080/00337578408215798
- [114] Z. Talip, T. Wiss, V. Di Marcello, A. Janssen, J.-Y. Colle, P. Van Uffelen, P. Raison, and R.J.M. Konings. *Thermal diffusion of helium in ²³⁸Pu-doped UO₂*. J. Nucl. Mater. 445 (2014) 117-127. doi: 10.1016/j.jnucmat.2013.10.066

- [115] K. Une, K. Nogita, S. Kashibe, and M. Imamura. *Microstructural change and its influence on fission gas release in high burnup UO_2 fuel*. J. Nucl. Mater. 188 (1992) 65-72. doi: 10.1016/0022-3115(92)90455-T
- [116] S.L. Hayes, J.K. Thomas, and K.L. Peddicord. *Material property correlations for uranium mononitride: I. Physical properties*. J. Nucl. Mater. 171 (1990) 262-270. doi: 10.1016/0022-3115(90)90374-V
- [117] K. Barla, R. Herino, G. Bomchil, J.C. Pfister, and A. Freund. *Determination of lattice parameter and elastic properties of porous silicon by X-ray diffraction*. J. Cryst. Growth 68 (1984) 727-732. doi: 10.1016/0022-0248(84)90111-8
- [118] G. Leinders, T. Cardinaels, K. Binnemans, and M. Verwerft. *Accurate lattice parameter measurements of stoichiometric uranium dioxide*. J. Nucl. Mater. 459 (2015) 135-142. doi: 10.1016/j.jnucmat.2015.01.029
- [119] H. Kleykamp. *The chemical state of the fission products in oxide fuels*. J. Nucl. Mater. 131 (1985) 221-246. doi: 10.1016/0022-3115(85)90460-X
- [120] H. Kleykamp. *The chemical state of fission products in oxide fuels at different stages of the nuclear fuel cycle*. Nucl. Technol. 80 (1988) 412-422. doi: 10.13182/NT88-A34065
- [121] K. Masumichi, S. Masakazu, and N. Kenji. *Phase study on solid fission products, Ba, Sr and Zr in oxide fuel*. J. Nucl. Mater. 51 (1974) 90-94. doi: 10.1016/0022-3115(74)90118-4
- [122] P.V. Nerikar, X.-Y. Liu, B.P. Uberuaga, C.R. Stanek, S.R. Phillpot, and S.B. Sinnott. *Thermodynamics of fission products in UO_{2+x}* . J. Phys. Condens. Matter 21 (2009) 435602. doi: 10.1088/0953-8984/21/43/435602
- [123] C. Degueldre, M. Martin, G. Kuri, D. Grolimund, and C.N. Borca. *Plutonium-uranium mixed oxide characterization by coupling micro-X-ray diffraction and absorption investigations*. J. Nucl. Mater. 416 (2011) 142-150. doi: 10.1016/j.jnucmat.2010.11.096
- [124] C.T. Walker, C. Bagger, and M. Mogensen. *Observations on the release of cesium from UO_2 fuel*. J. Nucl. Mater. 240 (1996) 32-42. doi: 10.1016/S0022-3115(96)00477-1
- [125] S. Ishimoto, M. Hirai, K. Ito, and Y. Korei. *Effects of soluble fission products on thermal conductivities of nuclear fuel pellets*. J. Nucl. Sci. Technol. 31 (1994) 796-802. doi: 10.1080/18811248.1994.9735225
- [126] C. Sari, C.T. Walker, and G. Schumacher. *Solubility and migration of fission product barium in oxide fuel*. J. Nucl. Mater. 79:1 (1979) 255-259. doi: 10.1016/0022-3115(79)90455-0
- [127] S.C. Middleburgh, R.W. Grimes, K.H. Desai, P.R. Blair, L. Hallstadius, K. Backman, and P. Van Uffelen. *Swelling due to fission products and additives*

- dissolved within the uranium dioxide lattice.* J. Nucl. Mater. 427 (2012) 359-363. doi: 10.1016/j.jnucmat.2012.03.037
- [128] E. Remy, S. Picart, T. Delahaye, I. Jobelin, O. Dugne, I. Bisel, P. Blanchart, and A. Ayral. *Fabrication of uranium dioxide ceramic pellets with controlled porosity from oxide microspheres.* J. Nucl. Mater. 448 (2014) 80-86. doi: 10.1016/j.jnucmat.2014.01.017
- [129] R.D. Shannon. *Revised effective ionic radii and systematic studies of interatomic distances in halides and chalcogenides.* Acta Crystallogr. A 32 (1976) 751-767. doi: 10.1107/S0567739476001551
- [130] D.-J. Kim. *Lattice parameters, ionic conductivities, and solubility limits in fluorite-structure MO₂ oxide [M = Hf⁴⁺, Zr⁴⁺, Ce⁴⁺, Th⁴⁺, U⁴⁺] solid solutions.* J. Am. Ceram. Soc. 72 (1989) 1415-1421. doi: 10.1111/j.1151-2916.1989.tb07663.x
- [131] S. Imoto. *Chemical state of fission products in irradiated UO₂.* J. Nucl. Mater. 140 (1986) 19-27. doi: 10.1016/0022-3115(86)90192-3
- [132] G. Brillant and A. Pasturel. *Study of Ba and Zr stability in UO_{2±x} by density functional calculations.* Phys. Rev. B 77 (2008) 184110. doi: 10.1103/PhysRevB.77.184110
- [133] A.N. Goland and D.T. Keating. *Lattice parameter, volume, and length changes in crystals containing dislocation loops.* J. Appl. Phys. 41 (1970) 814-815. doi: 10.1063/1.1658759
- [134] M.A. Krivoglaz. *X-ray and neutron diffraction in nonideal crystals.* Springer Science & Business Media, 2012.
- [135] T.-H. Nguyen, A. Debelle, A. Boulle, F. Garrido, L. Thomé, and V. Demange. *Mechanical response of UO₂ single crystals submitted to low-energy ion irradiation.* J. Nucl. Mater. 467 (2015) 505-511. doi: 10.1016/j.jnucmat.2015.10.046
- [136] H. Palancher, R. Kachnaoui, G. Martin, A. Richard, J.-C. Richaud, C. Onofri, R. Belin, A. Boulle, H. Rouquette, C. Sabathier, G. Carlot, P. Desgardin, T. Sauvage, F. Rieutord, J. Raynal, Ph. Goudeau, and A. Ambard. *Strain relaxation in He implanted UO₂ polycrystals under thermal treatment: An in situ XRD study.* J. Nucl. Mater. 476 (2016) 63-76. doi: 10.1016/j.jnucmat.2016.04.023
- [137] G. Gutierrez, D. Gosset, M. Bricout, C. Onofri, and A. Debelle. *Effect of coupled electronic and nuclear energy deposition on strain and stress levels in UO₂.* J. Nucl. Mater. 519 (2019) 52-56. doi: 10.1016/j.jnucmat.2019.03.034
- [138] M. Bricout, C. Onofri, A. Debelle, Y. Pipon, R.C. Belin, F. Garrido, F. Leprêtre, and G. Gutierrez. *Radiation damage in uranium dioxide: Coupled effect between electronic and nuclear energy losses.* J. Nucl. Mater. 531 (2020) 151967. doi: 10.1016/j.jnucmat.2019.151967

- [139] A. Boulle, A. Chartier, A. Debelle, X. Jin, and J.-P. Crocombette. *Computational diffraction reveals long-range strains, distortions and disorder in molecular dynamics simulations of irradiated single crystals*. J. Appl. Crystallogr. 55 (2022) 296-309. doi: 10.1107/S1600576722001406
- [140] M. Amaya, J. Nakamura, and T. Fuketa. *Measurements of crystal lattice strain and crystallite size in irradiated UO₂ pellet by X-ray Diffractometry*. J. Nucl. Sci. Technol. 45 (2008) 244-250. doi: 10.1080/18811248.2008.9711433
- [141] K. Nogita and K. Une. *Radiation-induced microstructural change in high burnup UO₂ fuel pellets*. Nucl. Instrum. Methods Phys. Res. Sect. B Beam Interact. Mater. At. 91 (1994) 301-306. doi: 10.1016/0168-583X(94)96235-9
- [142] K. Nogita and K. Une. *Irradiation-induced recrystallization in high burnup UO₂ fuel*. J. Nucl. Mater. 226 (1995) 302-310. doi: 10.1016/0022-3115(95)00123-9
- [143] Yu.K. Bibilashvili, A.V. Medvedev, G.A. Khvostov, S.M. Bogatyr, and L.V. Korystine. *Development of the fission gas behaviour model in the start-3 code and its experimental support*. Proceedings of Seminar on Fission Gas Behaviour In Water Reactor Fuels, Cadarache, France (2000) 407-425.
- [144] K. Nogita, K. Une, M. Hirai, K. Ito, K. Ito, and Y. Shirai. *Effect of grain size on recrystallization in high burnup fuel pellets*. J. Nucl. Mater. 248 (1997) 196-203. doi: 10.1016/S0022-3115(97)00156-6
- [145] M.G. Abdoelatef, F. Badry, D. Schwen, C. Permann, Y. Zhang, and K. Ahmed. *Mesoscale modeling of high burn-up structure formation and evolution in UO₂*. JOM 71 (2019) 4817-4828. doi: 10.1007/s11837-019-03830-z
- [146] I.L.F. Ray, H.J. Matzke, H.A. Thiele, and M. Kinoshita. *An electron microscopy study of the RIM structure of a UO₂ fuel with a high burnup of 7.9% FIMA*. J. Nucl. Mater. 245 (1997) 115-123. doi: 10.1016/S0022-3115(97)00015-9
- [147] R.I. Barabash, G.E. Ice, B.C. Larson, G.M. Pharr, K.-S. Chung, and W. Yang. *White microbeam diffraction from distorted crystals*. Appl. Phys. Lett. 79 (2001) 749-751. doi: 10.1063/1.1389321
- [148] R.I. Barabash, G.E. Ice, and F.J. Walker. *Quantitative microdiffraction from deformed crystals with unpaired dislocations and dislocation walls*. J. Appl. Phys. 93 (2003) 1457-1464. doi: 10.1063/1.1534378
- [149] A.S. Budiman, W.D. Nix, N. Tamura, B.C. Valek, K. Gadre, J. Maiz, R. Spolenak, and J.R. Patel. *Crystal plasticity in Cu damascene interconnect lines undergoing electromigration as revealed by synchrotron x-ray microdiffraction*. Appl. Phys. Lett. 88 (2006) 233515. doi: 10.1063/1.2210451
- [150] G.E. Ice and J.W.L. Pang. *Tutorial on x-ray microLaue diffraction*. Mater. Charact. 60 (2009) 1191-1201. doi: 10.1016/j.matchar.2009.07.006

- [151] D.C. Pagan and M.P. Miller. *Connecting heterogeneous single slip to diffraction peak evolution in high-energy monochromatic X-ray experiments*. J. Appl. Crystallogr. 47 (2014) 887-898. doi: 10.1107/S1600576714005779
- [152] A.S. Budiman, S.-M. Hanb, N. Li, Q.-M. Wei, P. Dickerson, N. Tamura, M. Kunz, and A. Misra. *Plasticity in the nanoscale Cu/Nb single-crystal multilayers as revealed by synchrotron Laue x-ray microdiffraction*. J. Mater. Res. 27 (2012) 599-611. doi: 10.1557/jmr.2011.421
- [153] J. Yan, W. Dong, P. Shi, T. Li, W. Liu, Y.-D. Wang, X.-L. Wang, Y. Zhu, and Y. Ren. *Synchrotron x-ray study of heterostructured materials: A review*. JOM 75 (2023) 1423-1434. doi: 10.1007/s11837-023-05711-y
- [154] K.R. Magid, J.N. Florando, D.H. Lassila, M.M. LeBlanc, N. Tamura, and J.W. Morris. *Mapping mesoscale heterogeneity in the plastic deformation of a copper single crystal*. Philos. Mag. 89 (2009) 77-107. doi: 10.1080/14786430802558577
- [155] J.F. Nye. *Some geometrical relations in dislocated crystals*. Acta Metall. 1 (1953) 153-162. doi: 10.1016/0001-6160(53)90054-6
- [156] S. Das, F. Hofmann, and E. Tarleton. *Consistent determination of geometrically necessary dislocation density from simulations and experiments*. Int. J. Plast. 109 (2018) 18-42. doi: 10.1016/j.ijplas.2018.05.001
- [157] M.F. Ashby. *The deformation of plastically non-homogeneous materials*. Philos. Mag. J. Theor. Exp. Appl. Phys. 21 (1970) 399-424. doi: 10.1080/14786437008238426
- [158] A. Arsenlis, D.M. Parks, R. Becker, and V.V. Bulatov. *On the evolution of crystallographic dislocation density in non-homogeneously deforming crystals*. J. Mech. Phys. Solids 52 (2004) 1213-1246. doi: 10.1016/j.jmps.2003.12.007
- [159] A. Arsenlis and D.M. Parks. *Crystallographic aspects of geometrically-necessary and statistically-stored dislocation density*. Acta Mater. 47 (1999) 1597-1611. doi: 10.1016/S1359-6454(99)00020-8
- [160] J. Hua and A. Hartmaier. *Determining Burgers vectors and geometrically necessary dislocation densities from atomistic data*. Model. Simul. Mater. Sci. Eng. 18 (2010) 045007. doi: 10.1088/0965-0393/18/4/045007
- [161] H. Gao, Y. Huang, W.D. Nix, and J.W. Hutchinson. *Mechanism-based strain gradient plasticity– I. Theory*. J. Mech. Phys. Solids 47 (1999) 1239-1263. doi: 10.1016/S0022-5096(98)00103-3
- [162] S.T. Murphy, M.J.D. Rushton, and R.W. Grimes. *A comparison of empirical potential models for the simulation of dislocations in uranium dioxide*. Prog. Nucl. Energy 72 (2014) 27-32. doi: 10.1016/j.pnucene.2013.09.010

-
- [163] B. Deng, A. Chernatynskiy, P. Shukla, S.B. Sinnott, and S.R. Phillpot. *Effects of edge dislocations on thermal transport in UO₂*. J. Nucl. Mater. 434 (2013) 203-209. doi: 10.1016/j.jnucmat.2012.11.043
 - [164] L. Portelette, J. Amodeo, B. Michel, and R. Madec. *Athermal dislocation strengthening in UO₂*. J. Nucl. Mater. 538 (2020) 152157. doi: 10.1016/j.jnucmat.2020.152157
 - [165] X.-Y. Liu, E. Martinez, and B.P. Uberuaga. *Dissociated vacancies and screw dislocations in MgO and UO₂: Atomistic modeling and linear elasticity analysis*. Sci. Rep. 9 (2019) 6499. doi: 10.1038/s41598-019-42926-z
 - [166] A.V. Lunev, S.V. Starikov, T.N. Aliev, and V.I. Tseplyaev. *Understanding thermally-activated glide of $1/2\langle 110 \rangle\{110\}$ screw dislocations in UO₂ – A molecular dynamics analysis*. Int. J. Plast. 110 (2018) 294-305. doi: 10.1016/j.ijplas.2018.07.003
 - [167] A. Alamo, J.M. Lefebvre, and J. Soullard. *Deformation plastique du bioxyde d'uranium: Observation des sous-structures de dislocations*. J. Nucl. Mater. 75 (1978) 145-153. doi: 10.1016/0022-3115(78)90038-7
 - [168] J. Rest. *Derivation of analytical expressions for the network dislocation density, change in lattice parameter, and for the recrystallized grain size in nuclear fuels*. J. Nucl. Mater. 349 (2006) 150-159. doi: 10.1016/j.jnucmat.2005.10.007
 - [169] H. Xiao, C. Long, and H. Chen. *Model for evolution of grain size in the rim region of high burnup UO₂ fuel*. J. Nucl. Mater. 471 (2016) 74-79. doi: 10.1016/j.jnucmat.2016.01.006
 - [170] M.S. Veshchunov and V.E. Shestak. *Model for evolution of crystal defects in UO₂ under irradiation up to high burn-ups*. J. Nucl. Mater. 384 (2009) 12-18. doi: 10.1016/j.jnucmat.2008.09.024
 - [171] T. Vazhappilly and A.K. Pathak. *Theoretical study on the mechanical and thermal properties of uranium dioxide doped with lanthanide fission products*. J. Nucl. Mater. 519 (2019) 128-136. doi: 10.1016/j.jnucmat.2019.03.032
 - [172] M.T. Aybers, A.A. Akşit, S. Akbal, Ş. Ekinci, A. Yaylı, L. Çolak, A. Van, B. Kopuz, and N. Ateş. *Grain growth in corundum oxides-doped uranium dioxide and effects of grain growth to the mechanical properties of uranium dioxide such as elasticity determined by ultrasonic methods*. Key Eng. Mater. 264-268 (2004) 985-988. doi: 10.4028/www.scientific.net/KEM.264-268.985
 - [173] R. Henry, I. Zacharie-Aubrun, T. Blay, N. Tarisien, S. Chalal, X. Iltis, J.-M. Gatt, C. Langlois, and S. Meille. *Irradiation effects on the fracture properties of UO₂ fuels studied by micro-mechanical testing*. J. Nucl. Mater. 536 (2020) 152179. doi: 10.1016/j.jnucmat.2020.152179

- [174] G. Kuri, C. Mieszczyński, M. Martin, J. Bertsch, C.N. Borca, and C. Delafoy. *Local atomic structure of chromium bearing precipitates in chromia doped uranium dioxide investigated by combined micro-beam X-ray diffraction and absorption spectroscopy*. J. Nucl. Mater. 449 (2014) 158-167.
doi: 10.1016/j.jnucmat.2014.03.017
- [175] J.J. Rehr, J. Mustre De Leon, S.I. Zabinsky, and R.C. Albers. *Theoretical x-ray absorption fine structure standards*. J. Am. Chem. Soc. 113 (1991) 5135-5140.
doi: 10.1021/ja00014a001
- [176] S. Bhattacharya, G. Kuri, M. Martin, J. Bertsch, and M.A. Pouchon. *Atomic-scale insights into structural distortions in irradiated UO₂ at an intermediate burnup around 50 MWd/kgU*. Proceedings of International LWR Fuel Performance Meeting (TopFuel), Raleigh, NC, USA (2022) 278-285.
doi: 10.13182/TopFuel22-38929
- [177] P. Martin, M. Ripert, T. Petit, T. Reich, C. Hennig, F. D'Acapito, J.L. Hazemann, and O. Proux. *A XAS study of the local environments of cations in (U, Ce)O₂*. J. Nucl. Mater. 312 (2003) 103-110. doi: 10.1016/S0022-3115(02)01590-8
- [178] J.G. Tobin, S.-W. Yu, C.H. Booth, T. Tylliszczak, D.K. Shuh, G. van der Laan, D. Sokaras, D. Nordlund, T.-C. Weng, and P.S. Bagus. *Oxidation and crystal field effects in uranium*. Phys. Rev. B 92 (2015) 035111.
doi: 10.1103/PhysRevB.92.035111
- [179] D. Prieur, U. Carvajal-Nunez, T. Vitova, and J. Somers. *Local and Electronic Structure of Americium-Bearing PuO₂*. Eur. J. Inorg. Chem. 2013 (2013) 1518-1524.
doi: 10.1002/ejic.201201294
- [180] J.A. Turnbull. *The distribution of intragranular fission gas bubbles in UO₂ during irradiation*. J. Nucl. Mater. 38 (1971) 203-212. doi: 10.1016/0022-3115(71)90044-4
- [181] M.V. Speight. *A calculation on the migration of fission gas in material exhibiting precipitation and re-solution of gas atoms under irradiation*. Nucl. Sci. Eng. 37 (1969) 180-185. doi: 10.13182/NSE69-A20676
- [182] I.L.F. Ray, H. Thiele, and H.J. Matzke. *Transmission electron microscopy study of fission product behaviour in high burnup UO₂*. J. Nucl. Mater. 188 (1992) 90-95.
doi: 10.1016/0022-3115(92)90458-W
- [183] S. Kashibe, K. Une, and K. Nogita. *Formation and growth of intragranular fission gas bubbles in UO₂ fuels with burnup of 6–83 GWd/t*. J. Nucl. Mater. 206 (1993) 22-34. doi: 10.1016/0022-3115(93)90229-R
- [184] R.M. Cornell. *An electron microscope examination of matrix fission-gas bubbles in irradiated uranium dioxide*. J. Nucl. Mater. 38 (1971) 319-328.
doi: 10.1016/0022-3115(71)90061-4

Curriculum vitae

Personal details

Name	Shaileyee Bhattacharya
Date of birth	June 16, 1996
Nationality	Indian
Address	Weiermattring 12, 5200 Brugg AG, Switzerland
E-mail address	shaileyee.bhattacharya@psi.ch shaileyeebhattacharya@gmail.com

Education

	Ph.D.: Material Science and Engineering
01/2020 – 03/2024	<i>École Polytechnique Fédérale de Lausanne (EPFL)</i> Lausanne, Switzerland
	Master of Science: Chemistry
07/2017 – 05/2019	<i>Indian Institute of Technology Roorkee (IIT-R)</i> Roorkee, Uttarakhand, India
	Bachelor of Science: Chemistry (Hons.)
07/2014 – 06/2017	<i>Miranda House, University of Delhi</i> New Delhi, India

Work and Research Experience

	Doctoral Student <i>Paul Scherrer Institut, Villigen, Switzerland</i> <i>Title: Atomic level insights into irradiation effects in nuclear fuel materials</i>
01/2020 – Present	<ul style="list-style-type: none">• Determination of atomic scale structural and chemical modifications of irradiated UO₂ materials, used for energy production in nuclear power plants• Analysis of UO₂ oxidation characteristics as a result of irradiation effects for long term, safe and economic in reactor use of fuels• Extensive hands on experience in a HotLab• EPMA analysis for elemental distribution of fission products in irradiated fuel matrix

- Synchrotron based X-ray diffraction and X-ray absorption spectroscopy studies of UO₂ particles
- Computational evaluation of atomic and electronic structures of UO₂ to explain experimentally observed phenomena
- Electron microscopy (TEM) analysis of irradiated fuels

Internship Student – Masters' Thesis Project

Max Planck Institute for Chemical Physics of Solids, Dresden, Germany

Title: Single crystal growth and electrical transport properties of some magnetic and non-magnetic topological phosphides

12/2018 – 04/2019

- Synthesis of high quality single crystals of magnetic (ZrMnP and HfMnP) and non-magnetic (WP and WP₂) topological phosphides
- Study of electrical transport and magnetic properties of synthesized single crystals

Internship Student

Max Planck Institute for Chemical Physics of Solids, Dresden, Germany

Title: Synthesis and characterization of single crystals of topological materials

05/2018 – 07/2018

- Single crystal growth of topological materials by metal flux method, Bridgman method, and chemical vapor transport method
- Characterization of crystals using Laue X-ray Diffraction, Energy Dispersive X-Ray Analysis (EDXA), *etc.*

Internship Student

S. N. Bose National Centre for Basic Sciences, Kolkata, India

Title: MD simulations for three dimensional gaseous molecules

12/2017 – 01/2018

- Molecular dynamics simulations using Leap Frog algorithm for energy minimization calculations of gaseous molecules in 3D

Publications

- **S. Bhattacharya**, G. Kuri, M. Martin, J. Bertsch, M.A. Pouchon. *Assessment of unit cell parameter, lattice strain and geometrically necessary dislocation density level in high burnup spent fuels: A synchrotron based scanning x-ray micro-diffraction study*. Manuscript ready for submission in a peer reviewed journal
- G. Kuri, H. Ramanantoanina, **S. Bhattacharya**, J. Bertsch, M. Martin. *Insights into the interfacial speciation of Ni in the corrosion layer of high burnup Zircaloy-2 cladding: A combined XRD, XAS, and LFDFT study*. Corrosion Science 215 (2023) 111024. (doi: 10.1016/j.corsci.2023.111024)
- **S. Bhattacharya**, G. Kuri, M. Martin, J. Bertsch, M.A. Pouchon. *Atomic-scale insights into structural distortions in irradiated UO₂ at an intermediate burnup around 50 MWd/kgU*. Proceedings of International LWR Fuel Performance Meeting (TopFuel), Raleigh, NC, USA (2022) 278-285. (doi: 10.13182/TopFuel22 38929)
- S. Singh, J. Nokty, **S. Bhattacharya**, P. Vir, Y. Sun, N. Kumar, C. Felser, C. Shekhar. *Anisotropic nodal line derived large anomalous Hall conductivity in ZrMnP and HfMnP*. Advanced Materials 33 (2021) Issue 48 2104126. (doi: 10.1002/adma.202104126)

Conference Presentations

- **S. Bhattacharya**, G. Kuri, J. Bertsch, M.A. Pouchon. *Atomic level insights into nuclear fuels irradiated in light water reactor: Synchrotron light investigations*. E-MRS 2023 Fall Meeting (18-21 September, 2023 / Warsaw, Poland) – Oral presentation.
- **S. Bhattacharya**, G. Kuri, M. Martin, J. Bertsch, M.A. Pouchon. *Atomic-scale insights into structural distortions in irradiated UO₂ at an intermediate burnup around 50 MWd/kgU*. TopFuel 2022 Conference (9-13 October, 2022 / Raleigh, NC, USA) – Oral presentation.
- **S. Bhattacharya**, G. Kuri, J. Bertsch. *Dislocation nucleation in UO₂ spent fuels evaluated by synchrotron based Laue diffraction method*. CIMTEC 2022 Conference (25-29 June, 2022 / Perugia, Italy) – Oral presentation.
- **S. Bhattacharya**, G. Kuri, M. Martin, J. Bertsch, M.A. Pouchon. *Grains subdivision and accumulation of geometrically necessary dislocations in irradiated UO₂ studied by micro beam Laue diffraction*. NuMat 2020 Conference (26-30 October, 2020 / Ghent, Belgium)– Virtual oral presentation.